Dynamics of Granular Crystals with Elastic-Plastic Contacts

Thesis by
Hayden Andrew Burgoyne

In Partial Fulfillment of the Requirements for the
degree of
Doctor of Philosophy in Space Engineering

CALIFORNIA INSTITUTE OF TECHNOLOGY
Pasadena, California

2016
Defended April 15, 2016

Hayden Andrew Burgoyne
ORCID: orcid.org/0000-0003-0891-6411

ACKNOWLEDGEMENTS

First, I would like to thank my advisor, Chiara Daraio, for all her guidance, support, and contributions. She was wonderfully helpful as a professor and very kind as a mentor. I wish I could have spent more time in her lab at ETH Zurich as well, but I greatly appreciate how accommodating she was. I'd also like to thank Guruswami Ravichandran, who acted as a co-advisor and provided essential support through the NASA Space Technology Fellowship, the Air Force Center of Excellence and particularly with his wonderful research group at Caltech. I'd also like to thank John "Andy" Newman from NASA Langley, who became my collaborator through the NASA Space Technology Fellowship program. My time at NASA Langley was extremely crucial to everything I accomplished during my studies, and without Andy none of it would be possible. Andy was extremely generous with his time and resources in helping to enable much of the experimental work. I'd also like to thank the other members of my thesis committee: Jose Andrade, who taught an extremely useful plasticity course and provided support and guidance through the Air Force Center of Excellence and, finally, committee chair Dennis Kochmann. I'd also like to thank Professor Kochmann for including me in his Keck Institute for Space Studies workshop which was a fantastic learning experience and professional opportunity.

I'd like to thank the NASA Space Technology Fellowship program for their generous support, for introducing me to essential collaborators, and for providing amazing experiences at NASA Langley. This work and my graduate studies were supported by NSTRF grant number NNX13AL66H.

Additionally, I'd like to acknowledge funding from the Air Force Office of Scientific Research (AFOSR) and Air Force Research Labs (AFRL). This work was support by AFOSR grant number FA9550-12-1-0091 through the University Center of Excellence in High-Rate Deformation Physics of Heterogeneous Materials.

I'd like to thank everyone in GALCIT for being the best department at Caltech. In particular, Cheryl Gause was always so patient whenever I found a new way to make her job difficult. Dimity Nelson was the real hero during my time organizing the Caltech Space Challenge. Thank you so much Dimity! No piece of experimental equipment in GALCIT would function without Petros Arakelian, who always had innovative and practical solutions in the lab. Thank you to all the other GALCIT

professors who taught great courses to prepare me for my research and for my professional career.

And of course, my friends and family. I have to start with the most important person in my life, Kristina Hogstrom. I never could have wished for a better partner through this entire experience than you. Being able to share both the burdens and the successes together has added so much more meaning to my time at Caltech and made it so much more rewarding. You're my best friend and my best collaborator. From the first-year problem sets, to experiments at NASA in Virginia, to conferences in Jerusalem, working together at Caltech was just the start of our lives together.

Thank you so much to all of my friends from GALCIT for making the years at Caltech so much more enjoyable and fun. In particular, I have to thank Bruno Savard for being a great roommate all those years, Niko Cymbalist for being an awesome co-organizer for the Caltech Space Challenge, Jordan Croom for helping Kristina and I crush so many problem sets, and Christian Kettenbeil for being so helpful in the lab. Too many other Caltech friends also deserve so much appreciation; thank you all so much! I'd also like to thank all of my other friends in Los Angeles, particularly my high school friends, for always taking an interest in how things are going.

Finally, I'd like to thank my entire family. It was such an advantage to be so close to such a wonderful support group. Each and every one of you contributed greatly to all the success I've had. My grandparents, Rod, Toni, Joan, and Arnie, have always been critical in teaching me the value of education. My step-parents, aunts and uncles, and cousins have all been so supportive and encouraging throughout my education. My siblings Marnie, Andrew, Stephanie, Avi, and Jon are the best brothers and sisters in the world! My parents, Rodney and Anita, have always treated me with such kindness and respect. I love them so much and I owe them everything.

ABSTRACT

We study the behavior of granular crystals subjected to impact loading that creates plastic deformation at the contacts between constituent particles. Granular crystals are highly periodic arrangements of spherical particles, arranged into densely packed structures resembling crystals. This special class of granular materials has been shown to have unique dynamics with suggested applications in impact protection. However, previous work has focused on very low amplitude impacts where every contact point can be described using the Hertzian contact law, valid only for purely elastic deformation. In this thesis, we extend previous investigation of the dynamics of granular crystals to significantly higher impact energies more suitable for the majority of applications. Additionally, we demonstrate new properties specific to elastic-plastic granular crystals and discuss their potential applications as well. We first develop a new contact law to describe the interaction between particles for large amplitude compression of elastic-plastic spherical particles including a formulation for strain-rate dependent plasticity. We numerically and experimentally demonstrate the applicability of this contact law to a variety of materials typically used in granular crystals. We then extend our investigation to one-dimensional chains of elastic-plastic particles, including chains of alternating dissimilar materials. We show that, using the new elastic-plastic contact law, we can predict the speed at which impact waves with plastic dissipation propagate based on the material properties of the constituent particles. Finally, we experimentally and numerically investigate the dynamics of two-dimensional and three-dimensional granular crystals with elastic-plastic contacts. We first show that the predicted wave speeds for 1D granular crystals can be extended to 2D and 3D materials. We then investigate the behavior of waves propagating across oblique interfaces of dissimilar particles. We show that the character of the refracted wave can be predicted using an analog to Snell's law for elastic-plastic granular crystals and ultimately show how it can be used to design impact guiding "lenses" for mitigation applications.

PUBLISHED CONTENT AND CONTRIBUTIONS

[1] Hayden A. Burgoyne and Chiara Daraio. “Strain-rate-dependent model for the dynamic compression of elastoplastic spheres.” In: *Physical review. E, Statistical, nonlinear, and soft matter physics* 89.3 (Mar. 2014), p. 032203. ISSN: 1550-2376. DOI: 10.1103/PhysRevE.89.032203. URL: http://journals.aps.org/pre/abstract/10.1103/PhysRevE.89.032203.
H.A.B contributed to the conception of this work, formulation of the model, numerical analyses, experimental validation, writing of the manuscript, and preparation of figures.

[2] Hayden A. Burgoyne and Chiara Daraio. “Elastic–Plastic Wave Propagation in Uniform and Periodic Granular Chains”. In: *Journal of Applied Mechanics* 82.8 (June 2015), p. 081002. DOI: 10.1115/1.4030458. URL: http://appliedmechanics.asmedigitalcollection.asme.org/article.aspx?articleid=2288770%7B%5C&%7DresultClick=3.
H.A.B contributed to the conception of this work, development of simulations, numerical analyses, experimental validation, writing of the manuscript, and preparation of figures.

[3] Hayden A. Burgoyne et al. “Guided Impact Mitigation in 2D and 3D Granular Crystals”. In: *Procedia Engineering* 103 (2015), pp. 52–59. ISSN: 18777058. DOI: 10.1016/j.proeng.2015.04.008. URL: http://www.sciencedirect.com/science/article/pii/S1877705815006827.
H.A.B contributed to the conception of this work, development of simulations, numerical analyses, experimental validation, writing of the manuscript, and preparation of figures.

TABLE OF CONTENTS

LIST OF ILLUSTRATIONS

LIST OF TABLES

Chapter 1

INTRODUCTION

This thesis is an investigation of the dynamics of high energy impacts on densely-packed arrangements of spherical metallic particles that cause plastic deformation at the contact points between granules. We call these arrangements of particles "granular crystals" because of the discrete nature of the grains that compose them and because their highly-organized periodic arrangements mimic the structures of crystals. Over the course of this work, we systematically progress from creating a description of the interaction between individual grains, through to the design of heterogeneous 2D and 3D granular crystals with specific applications in impact protection and mitigation. First, this introduction illustrates some of the motivation for investigating these material systems, describes the foundation laid by previous work upon which we build, and then lays out the goals and organization of this thesis as a whole.

1.1 Background and Previous Work

Because of their subtle complexity, the details of the dynamics of granular materials have long been an active field of research in mechanics. Granular materials like sand, soils, or even grains of rice often behave differently than most solids and can sometimes act more like liquids or gases with surprising results [1, 2]. Because granular materials are so ubiquitous but also so intricately complex, there are many ways to approach the problem of better understanding their dynamic properties and many ways in which new understandings could be beneficial to society. As an example, there are many industries in which the manipulation of granular materials is the key to efficiency, such as farming, mining, pharmaceuticals, and construction. Additionally, planetary science relies heavily on knowledge of the behaviors of granular materials, particularly in simulations of collisions of smaller planetary bodies such as asteroids or in the large collision between the early Earth and an unknown body that formed the Moon. Finally, we often rely on granular materials to provide protection from high velocity impacts. Sand bags are most often used to protect against bullets and other ballistics. Granular materials are typically effective at absorbing the energy of impact through the crushing of individual grains and rearranging of the grains within the bulk material.

1.1.1 Contact Behavior

The key feature that imbues granular materials with their unique properties as well as their complexity is the interactions between the grains. Their interactions are typically highly non-linear, leading to dynamics that are both dissimilar to typical linear continuum mechanics and often dissimilar among different classes of granular materials. One non-linearity stems from the fact that many granular materials cannot support tension. Grains are typically free to separate from their neighbors without any adhesion, so bulk materials behave differently in tension than in compression. However, the arguably more consequential non-linearity is in the force-displacement relationship; forces between grains often do not increase linearly with increased overlap between them. The contact behavior in the simplest possible granular material—spherical particles with a linear elastic material model—was first postulated by Hertz in 1881 [3]. He showed analytically and experimentally that the force between spherical elastic particles increased as the displacement between the particles to the 3/2 power. Beginning from a point contact, the contact area between the particles expands into a circle and grows as they are compressed together, continually increasing the amount of force required to incrementally increase the particles' overlap. He also determined that the radial distribution of forces within the contact area was parabolic with a maximum at the center of the contact, going to zero around the edges. The behavior of particles and the character of the non-linear interaction can be significantly altered by changing the shape or the material properties of the constituent grains. With each increase in complexity, their dynamics can be wholly different in order to be more suitable for a specific type of application or material system.

While the contact interaction for elastic bodies was analytically solved and experimentally verified by Hertz [3], the elastic-plastic contact deformation of spheres is still not well characterized. A fully analytical solution for stresses during the compression of two spheres has not been obtained even for bi-linear, elastic-perfectly plastic materials, disregarding any strain-hardening or more complicated material model. Therefore, many models have been made for the dynamic compression of elastic-plastic spheres that incorporate a mix of analytical, numerical, and experimental methods.

Thornton's initial model applied a Von Mises criterion to the stresses between two elastic spheres, capping the parabolic pressure distribution in the contact area [4]. Using this pressure distribution, Thornton was able to model the coefficient of

restitution for elastic-plastic collisions between particles; however the predictions did not suitably match experimental results in many cases. From this pioneering work, there were many subsequent extensions in order to create a model that was applicable for various geometries, materials, or loading cases as needed [5–9]. Many finite element method (FEM) studies modeled the loading of elastic-plastic hemispheres on a rigid wall or conversely a rigid hemisphere compressed into an elastic-plastic half-space [10–13]. However, these models were not general enough to be suitable for design of granular systems with a wide variety of constituent materials or for a suitable variety of loading amplitudes and rates.

Because this work is motivated by understanding impact protection for high velocity impacts, the strain rate dependent plasticity behavior of many of the materials typically used in granular crystals is of great importance. Strain rate dependence has been previously noted in the experimental observation of collisions between spheres, as well as in Hopkinson bar experiments involving hemispherical contacts [14–16]. The Hopkinson bar experiments, performed by Wang et al. to experimentally measure the dynamic force-displacement response of the contact between two metallic hemispheres, showed that strain rate dependence was particularly important for steels [17]. It was demonstrated that existing models do not correctly predict the strain rate dependent behavior without additional empirical constraints. However, attempts to do so were performed by tuning existing models for the specific loading rates needed to satisfy experimental conditions instead of attempting to incorporate existing models for strain rate dependent plastic behavior, such as the relatively simplistic Johnson-Cook model [18].

1.1.2 Dynamics of 1D Granular Crystals

In recent years, there has been extensive investigation into the behavior of 1D chains of particles with non-linear contact interactions, beginning with Nesterenko demonstrating the formation of solitary waves in Hertzian granular chains [19, 20]. Solitary waves, or "solitons," are steady non-linear waves that do not exhibit dispersion, i.e. the pulse shape does not change as the wave propagates through the granular material. In an uncompressed chain of elastic particles, there is initially no stiffness because each contact is a point and therefore the sonic wave speed is zero. After an impact, a soliton, or train of solitons, will form and travel at a speed that is frequency independent, but amplitude dependent. This wave speed can be written as [21]:

$$V_{\mathrm{H,1D}} = 0.68 \left(\frac{E^*}{r^* \rho^{3/2}} \right)^{1/3} F_M^{1/6}, \tag{1.1}$$

where E^* and r^* are functions of the particles' elastic properties and radius respectively, ρ is the density of the constituent material and F_M is the maximum force experienced at the contacts. Because no energy is dissipated at the elastic Hertzian contacts, F_m (and therefore $V_{\mathrm{H,1D}}$) remains constant.

Many subsequent studies demonstrated dynamic properties of elastic 1D materials which seemed useful for impact protection applications. These studies typically use a combination of experimental investigations with numerical simulations using discrete element method (DEM) simulations [22]. Using precompression the wave speed can be tuned [23]. Branching and recombining of 1D chains allowed for further manipulation of how energy propagates, selectively directing energy by choosing materials in each branch and branch angles [24, 25]. Additionally, the dynamics of heterogeneous chains of particles, particularly alternating chains of two materials often called "dimer chains," have been shown to enhance the impact protection applications. At the interfaces between chains of different constituent particle materials within a 1D chain, reflected waves can appear in order to trap energy and dissipate shock-type waves [22, 26–29]. In dimer chains, local resonances of the different phases have been shown to further slow the transmission of energy [30–34]. For acoustic and harmonic excitations, dimer chains have been used to create materials with tunable band gaps with proposed applications in vibration isolation and acoustic filters [35–41]. However, these effects, for uniform and dimer chains, were all demonstrated at significantly lower forces than useful for most impact applications because they relied on the materials remaining elastic throughout the impacts [42].

Because of the enticing properties of 1D granular crystals for impact mitigation, attempts to extend these investigations to include the inevitable plasticity at the contacts have more recently been attempted. The dynamics of chains of elastic-plastic particles has been investigated with numerical and experimental approaches [29-34]. The Hopkinson bar experiments used to obtain force-displacement data from single contacts were extended to experiments of longer 1D chains [43, 44]. However, because a significant portion of the impact energy is dissipated through plastic deformation at the contacts, the experiments were very limited in length of the 1D chain in order to obtain meaningful measurements from the transmitted wave through the chain. Numerical studies were also performed using DEM incorporating

various simplified models for the elastic-plastic contact behavior [45–48]. These studies began to describe the types of waves that form after impacts in elastic-plastic granular materials and their characteristic properties such as energy dissipation and wave speed. In these studies, simulations showed that the leading plastic wave propagating through elastic-plastic granular chains traveled slower than subsequent unloading and reloading waves due to residual plastic deformations changing the geometry of the contacts [45, 47]. In these events, the unloading and reloading waves following the first compressive wave operate in the elastic regime and exhibit the same properties as waves in elastic Hertzian granular chains. However, the initial plastic wave exhibits a different dynamic response governed by its unique contact law. Work by Pal el al. described the energy dissipation of a short impulse inducing plasticity in the initial particles of a long chain and the dependence of the wave speed on the excitation amplitude [45], but the dependence of the wave speed on the particles' material properties was not investigated.

1.1.3 2D and 3D Granular Crystals

As in the one-dimensional case, work in 2D and 3D granular crystals has mostly focused on experimental and numerical investigation without plasticity at the contacts. Recent work has extended many of the findings in 1D towards understanding non-linear wave propagation in elastic 2D and 3D granular crystals with Hertzian contacts. Much of the research has focused on the differences in how waves propagate through 2D and 3D materials due to the geometry of their crystal structure. In 2D, Leonard el al. investigated the nature of waves in square packings versus in hexagonal packings [49–51], as well as square packings with intruder particles embedded [52–54]. Anisotropic control over how waves propagated radially out from an elastic impact was demonstrated by choosing the materials used in 2D geometries [55]. Incorporating randomness and disorder into 2D granular crystals has also been shown to significantly influence the propagation of waves [25, 56]. The focus on crystal structure has been particularly dominant in 3D because there is a much greater variety of crystals than in 2D [57–59]. The dynamic responses of hexagonal close packed (HCP), face centered cubic (FCC) or body centered cubic (BCC) are distinguished by the number of neighboring contact particles, the angles between each contact, and the bulk density of the particle packing.

A recent development in the investigation of 2D and 3D granular crystals showed that with some scaling, the results for 1D chains of elastic particles could be applied to higher dimensional systems. Manjunath et al. showed that the predicted solitary

wave speed given in Equations 1.1 could be directly related to planar wave speed propagation through 2D and 3D lattices [60]. By using a scaling that took into account both the effects of stiffness changes due to contact geometry and density changes due to packing density, it was shown that:

$$\begin{aligned} V_{\mathrm{H,2D}} &= \frac{3}{2\sqrt{2}} V_{\mathrm{H,1D}} \\ V_{\mathrm{H,3D}} &= \frac{2}{\sqrt{3}} V_{\mathrm{H,1D}}, \end{aligned} \tag{1.2}$$

where $V_{\mathrm{H,1D}}$ was the solitary wave speed through 1D Hertzian granular chains from Equations 1.1. For this scaling, the 2D granular crystals were hexagonally packed and the 3D crystal structure was HCP. In all cases investigated, the plane waves were excited only along the close packed direction.

Tichler et al. recently showed that for 2D elastic granular crystals, an analog to Snell's law for optics can be written to describe the behavior of solitary plane waves impinging on oblique interfaces between two materials [61]. Snell's law can be derived for any type of wave from the geometry of the interface and knowledge of the speed at which waves travel on either side of the interface. In its simplest form, Snell's law allows us to find the angle of refraction, the angle at which transmitted waves are bent with respect to the interface between materials, to be:

$$\frac{\sin \Theta_{\mathrm{inc}}}{\sin \Theta_{\mathrm{ref}}} = \frac{V_1}{V_2}, \tag{1.3}$$

where V_1 and V_2 are the wave speeds in each of the materials and Θ_{inc} and Θ_{ref} are the incident and refracted wave angles with respect to the angle of the interface. Their finding that Snell's law can be applied to elastic granular crystals reveals two important things: first, it could only be valid if the solitary wave speed was independent of the angle the plane wave was propagating in with respect to the close packed direction. Second, many of the lessons and practices from optics, lens design, and optical metamaterials could possibly be applied to rationally designing heterogeneous granular crystals. If so, these materials be used for controlling the propagation of impact energy in the same fashion as light is manipulated in optics. However, as with most of the previous research, these findings were only demonstrated for elastic granular crystals with no plasticity at the contacts, and therefore the findings were not previously assumed to be applicable for impact protection applications.

Experimental investigations of high speed impacts on 2D and 3D granular materials have taken a variety of approaches. Initially work focused on using photoelas-

ticity to observe how polarized light is affected by stresses in soft transparent circular grains in 2D arrays of disk [62–64]. The experiments provided initial validation of the DEM approach to simulations of impact on granular materials. For elastic impacts on 2D granular crystals, embedded piezo-electric sensors within the particles were used to measure compressive forces along with embedded accelerometers [49, 50, 53, 54]. For much higher velocity impacts, others used impacts on beds of granular materials to observe the ejecta and the craters left behind [65–67]. Using high speed photography to track particles or even to do digital image correlation in order to observe strain fields within the particles has also been used on drop weight tower experiments or similar experiments using a small explosion to create an impulse [68].

1.1.4 Granular Metamaterials

While the complexities of the non-linear particle interactions and complicated geometries of the crystal structures are typically considered problems to be overcome through research, they can alternatively be thought of as parameters with which to rationally modify the dynamic behavior of these materials. With a deeper understanding of the contact law's effect on the dynamics, one can imagine designing a material to have a specific response to an excitation. Engineered materials are often described as "metamaterials" and are most frequently discussed when referring to optical metamaterials. Optical metamaterials have been used to demonstrate "negative refraction" of electromagnetic waves, controlling light in ways not possible with natural materials by introducing microstructure which manipulates the waves on the length-scale of its wavelength [69]. Metamaterials have now been investigated heavily for acoustic waves as well as other linear elastic waves [70–72]. This preliminary work led to more recent analytical, experimental, and numerical findings showing that layered composites comprised of thin plates can be used to effectively bend linear-elastic plane waves around a spherical obstacle [73–75]. In non-linear wave dynamics, materials with "tunable" properties are often discussed with an emphasis on controlling the nature of waves as they propagate through granular materials [23, 35]. In nearly all such metamaterials, the material is precisely designed for a known input and is often dependent on the frequency content or amplitude of the excitation. This makes many metamaterial designs less useful for real-world applications where the exact nature of the excitation isn't always known, especially for cloaking and protection applications.

As mentioned, granular materials inherently exhibit many properties that are

useful for impact protection and therefore disorganized random granular materials like sand and soil are the current standard in many applications. Because of their unique dynamics and opportunities for tunable properties, granular materials are also of great interest to the engineered materials community. However, there are still many unknowns as to the dynamic behavior of these materials in the higher-energy regimes applicable to impact protection applications. Furthermore, any designed material must have demonstrated use in "real-world" scenarios with realistic uncertainties, rather than be exclusively applicable to a specific case for which it is designed. With a greater fundamental understanding of the dynamics of these materials, perhaps it would be possible to replace a conventional sandbag with a system whereby the material properties and arrangement of each grain within the material is specifically chosen. Perhaps then the flow of energy within the material after an impact could be engineered and designed to achieve a specific goal. Impact energy could be directed away from sensitive regions of the material that we'd like to protect, towards less critical regions where damage could be localized.

1.2 Goals and Conceptual Organization

The goal of this research is to investigate the behavior of granular crystals after impacts at high pressures and strain-rates, in particular, for impacts that create plastic deformation at the contacts. Higher energy impacts represent a regime that has previously been avoided by a significant portion of granular crystal research because of the dramatically different dynamics that occur upon the initiation of plasticity. While previous work has discussed the applicability of designing granular crystals for use in impact protection, it has yet to be investigated whether the useful properties exhibited in the elastic-only cases remain in the elastic-plastic regime as well. Given that plasticity occurs at very low forces when dealing with the stress concentration between two spherical particles, it is nearly impossible to avoid plasticity when dealing with the types of impact problems for which protection is required. In this work, we present a systematic investigation of the dynamics of granular crystals composed of elastic-plastic particles.

This thesis has been organized to systematically build up the complexity of the dynamics being investigated in the same fashion as the logical progression occurred during the research. As discussed in the motivation, the key to understanding granular materials is characterizing the contact behavior. Therefore, we begin with a new description of the contact between elastic-plastic spherical particles. From there, we move to the simplest geometry of granular crystals, one-dimensional (1D)

chains of particles. After presenting some design considerations for 1D materials, we increase the complexity further and discuss the dynamics of impact wave propagation in two-dimensional (2D) and three-dimensional (3D) granular crystals.

Chapter 2 describes all the numerical and experimental tools that were used throughout this thesis. Numerical simulations were used as the main method of investigation of the dynamics of granular materials. Experiments were performed to validate the simplest cases of each type of material system (1D, 2D, homogeneous, heterogeneous, etc.). After validation, simulations allowed us to open up the design space and predict the behavior of materials which would have been prohibitively expensive, time consuming, or complicated to test experimentally.

In Chapter 3, we delve into a detailed description of individual contacts between elastic-plastic spherical particles used in this work. We present a new model for the force-displacement relationship and show that it is valid for a wide range of metallic spheres including materials with strain-rate dependent plasticity. The wide applicability of the model is necessary for facilitating the design of materials using elastic-plastic particles as building blocks as it allows us to choose from many useful materials. We experimentally validate this model using Hopkinson bar experiments at a variety of strain-rates and forces.

In Chapter 4, we increase complexity from single contacts to one-dimensional (1D) chains of particles. We investigate the properties of waves through elastic-plastic particles for both uniform chains of a single materials and dimer chains of two alternating materials. We experimentally validate our simulations again using the Hopkinson bar, but with the addition of a laser vibrometer to measure small oscillations of the particles towards the end of the long chains of particles. A key result from this chapter is a model for the speed at which waves travel through 1D chains of elastic-plastic particles and its sole dependence on the material properties of the constituent particles.

In Chapter 5, we discuss higher dimensions and investigate impacts on larger arrays of elastic-plastic particles. We present experiments to validate 2D and 3D simulations of impacts on uniform and heterogeneous arrays of elastic-plastic particles. Using the experimentally validated simulations, we extend the results obtained for 1D materials into higher dimensions. We also present models for how waves behave in heterogeneous granular crystals, particularly across angled interfaces between two materials. Finally, we show that these results allow us to apply knowledge from optics to create impact guiding lenses with applications in impact protection,

mitigation, and control of the flow of impact energy within a granular material.

In the final chapter, we summarize the findings presented in this thesis. We also provide a perspective on how this work could be extended and open questions that could be pursued in future work.

Chapter 2

METHODS

In this chapter we discuss the various numerical and experimental tools developed to support the findings of this thesis. Simulations allows us to quickly and efficiently explore the details of the dynamics of elastic-plastic granular materials, particularly for complex geometries and exotic materials. However, without experimental validation of the numerical tools, simulations cannot be assumed to be reliable proxies for the realities of the physics involved. Therefore, in this work, we use numerical simulations as our main method of investigation into the dynamics of waves in elastic-plastic behavior, but continually provide experiments to verify that the physics are being sufficiently captured and that all assumptions are valid.

2.1 Numerical Methods

2.1.1 Finite Elements Modeling of Elastic-Plastic Contact Behavior

In the simplest case, conventional tools used in continuum mechanics are helpful in initially understanding the behavior of single contacts between individual grains. Because the stresses in elastic-plastic spheres are not fully analytically solved, we must use finite element methods to simulate their response and extract the forces and displacements from the simulations.

In order to investigate the dependence of the force-displacement response on the material properties and sphere radius, we used a finite element model developed in ABAQUS. This allowed us to easily vary parameters over ranges that could not always be explored experimentally. We used an elastic-perfectly plastic constitutive model for the spheres materials and included a Johnson-Cook model for the strain-rate dependence. For quasistatic and constant strain-rate simulations we used ABAQUS/Standard, a non-linear implicit integrator, while for impact simulations we used ABAQUS/Explicit, a time-stepping non-linear explicit integrator. In quasistatic simulations, truncated spheres (Figure 2.1) were placed in hard contact between two rigid analytic surfaces without friction. Displacements of the rigid surfaces were prescribed such that the spheres would achieve about twice the displacement needed to reach the fully plastic region, but before finite deformations would induce any building up or sinking in of material around the contact surface. The total duration of the displacement of the rigid surface was varied in constant

strain-rate simulations in order to achieve the desired deformation rate. In dynamic simulations, an initial velocity was provided to the entire first sphere with the second sphere free. 1000 time steps were used in all simulations.

Taking advantage of radial symmetry, 6.35 mm diameter hemispheres were modeled as quarter circles comprised of around 2500 axisymmetric quad elements with nodes at the contact areas spaced 0.025 mm. This mesh was found to be of suitable accuracy through mesh convergence studies. With the very closely spaced nodes in the initial contact region, we were able to very accurately recover the Hertzian force-displacement predictions before plasticity initiated and resolve the initiation of plasticity below the contact surface as shown in Figure 2.1. With a coarser mesh away from the initial contact area, the force-displacement relation became scalloped because of the curved geometry; as each subsequent node came down to meet the contact surface, the force would appear to reach a minimum before ballooning up again after the node was in contact with the other surface. Significant increases in the mesh density all along the surface of the sphere successfully reduced the magnitude of these numerical oscillations. However, the force-displacement FEM results in the plastic region converged to a line which could also be obtained through a linear regression of the results with the oscillations. Because the mesh refinement required a significant increase in simulation time and the coarse results yielded the same fitted results, the mesh used was most suitable.

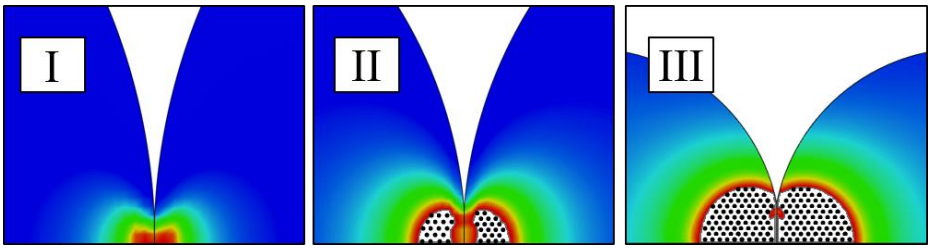

Figure 2.1: Schematics from ABAQUS showing the setup of the quasistatic compression experiments of the elastic-perfectly plastic hemispheres with colors representing the Von Mises stresses within the material. Three images showing the various regions involved in the development of plasticity I) before plasticity initiates, II) at the onset of plasticity while the plastic region is contained within elastic regions, and III) fully plastic regime where the contact area is fully plastic.

2.1.2 Discrete Element Method Modeling

Due to the curved geometry and varying contact area inherent in this problem, a fine mesh and small time steps are required for accurate FEM results. Therefore, FEM quickly becomes very computationally expensive even for just two particles. To extend simulations to allow for more complicated systems, particularly simulations of many spheres, we used a discrete element model (DEM), which is a technique that is often used in investigations of granular mechanics. DEM was first described by Cundall and Strack in 1979 and has been extensively used in the granular material since [19, 22, 34, 76]. DEM assumes particles to be rigid bodies which interact via nonlinear springs governed by a contact interaction model. Writing Newton's Second Law for each of the particles and contacts determines a system of coupled differential equations that can be solved with conventional numerical methods like Runge-Kutta integration. DEM sacrifices knowledge regarding local deformations, strains, and stresses within the particles in order to achieve its speed. However, it relies on the contact model to capture the intricacies of the interaction and is only as accurate as the contact law it incorporates. Each particle in the simulation is given three positional degrees of freedom and no angular rotations are allowed or considered. In many DEM codes, including the one developed here, there are no tangential forces (friction) applied between particles; only normal forces are applied.

The DEM approach developed in this work can be used for any suitable contact law to describe the interaction between particles. In this section, we'll describe how the DEM simulations were performed and how the code was organized. The details and formulation of the elastic-plastic contact model used for many of the simulations discussed in this chapter will be described in Chapter 3.

Description of General Discrete Element Method Implementation

Our implementation of the discrete element method was written in MATLAB. It consisted of three basic pieces: 1) initialization, 2) time integration of Newton's 2nd Law, and 3) post-processing. The key aspect of this code which necessitated creating a custom tool instead of using existing software such as LAAMPS was the incorporation of plastic deformation. In order to model plasticity, at each time step we were required to know whether this contact had been plasticity deformed previously in the simulation. In order to allow for loading, unloading, and reloading of elastic-plastic particles, the history of plastic deformation must be recorded for each contact pair after each time step. In our code, the history of plasticity, including

the maximum deformations and forces experienced by each particle previously in the simulation, is stored as global variables and continuously updated. Access to global variables is not readily available in any other code and so a new tool had to be developed.

At each time step in the simulations, the forces on every particle are summed and Newton's 2nd Law is numerically integrated to estimate the positions and velocities of each particle in the next time step. For the 1D case for a single particle, Newton's 2nd law represents a 2nd order ODE that can be written as two coupled first order ODEs as follows:

$$\ddot{x}_i = \frac{F_{\text{total},i}}{m_i} \quad \Rightarrow \quad \begin{cases} \dot{x}_i = v_i \\ \dot{v}_i = F_{\text{total},i}/m_i, \end{cases} \tag{2.1}$$

where x_i is the positions of the i-th particle, v_i is its velocity, dots represent time derivatives, $F_{\text{total},i}$ is the sum of all forces on that particle, and m_i is its mass. $F_{\text{total},i}$ can include prescribed forces over time as well as all interparticle forces. The specific model of the interparticle forces developed for the elastic-plastic case will be discussed in Chapter 3; however, it is a function of the displacements and velocities of the i-th particle and its contacts' displacement and velocity, and also a function of the time history of plasticity at the contacts between the particles. The MATLAB function used to calculate the interparticle forces is given in Appendix A.2.1 for the specific elastic-plastic contact law discussed in Chapter 3. For the 3D case, we must write Equation 2.1 for each of the three directional degrees of freedom giving us six ODEs total for each particle in the simulation. The ODEs for each particle given in Equation 2.1 for each directional degree of freedom can be combined into a single $6N$-element (where N is the number of particles) vector representing the time derivative of the state of the system of particles:

$$\frac{d\mathbf{X}}{dt} = \begin{bmatrix} \dot{x}_{1,x} \\ \dot{x}_{1,y} \\ \dot{x}_{1,z} \\ \dot{x}_{2,x} \\ \vdots \\ \dot{v}_{1,x} \\ \dot{v}_{1,y} \\ \dot{v}_{1,z} \\ \dot{v}_{2,x} \\ \vdots \end{bmatrix} = \begin{bmatrix} v_{1,x} \\ v_{1,y} \\ v_{1,z} \\ v_{2,x} \\ \vdots \\ F_{\text{total},1,x}/m_1 \\ F_{\text{total},1,y}/m_1 \\ F_{\text{total},1,z}/m_1 \\ F_{\text{total},2,x}/m_2 \\ \vdots \end{bmatrix} \tag{2.2}$$

The MATLAB script used to calculate the above derivative of the state vector in Equation 2.2 is given in Appendix A.2.2 for the 3D case.

By discretizing the time step, numerical integration can be used to calculate the state of the simulation at time t, for a given set of initial conditions for which each particles position and velocity at the initial time are specified in the vector $\mathbf{X}_0$. The integration was performed using MATLAB's *ode4* function, a 4th order Runge-Kutta (RK4) method with a fixed time step. The MATLAB script for the RK4 method used is given in Appendix A.2.3. A fixed time step was necessary versus a more efficient adaptive time step method like *ode45* in order to allow for saving the plastic deformation histories into global variables correctly after each time step.

The real materials used throughout this thesis and their material properties used in simulations are given in Table 2.1. Material properties were chosen from within the range given by the manufacture's specifications in order to most closely match preliminary experimentally measured values. The DEM implementation allows for a real material to be specified for each individual particle or a custom model material to be applied to groups of particles upon initialization.

Material	Density (kg/m^3)	Young's Modulus (GPa)	Yield Strength (MPa)
Stainless steel 440c	7650	200	1900
Stainless steel 302/304	7860	200	600
Aluminum 2017	2700	75	400
Brass 260	8530	110	670

Table 2.1: Material properties of the constituent materials used in DEM simulations.

Discrete Element Method Modeling for Single Elastic-Plastic Contacts

The first DEM simulations performed were used to test the model for the compression of elastic-plastic spherical particles and compare the simulations results to Hopkinson bar experiments. Samples comprised of two hemispherical particles (one contact point) were dynamically compressed at various strain-rates using Hopkinson bar experiments described further in Subsection 2.2.1. By varying the materials and the forces, the DEM simulations incorporating the model of the compression of

elastic-plastic spheres were experimentally validated over the range of cases needed for design of new granular crystals. From the experiments, the velocity profile over time measured from the end of the Hopkinson bar was applied as the velocity profile of the first particle in the simulation. The second particle was assumed to be in perfect contact with a 1D linear medium having the same properties as the transmission bar used in experiments (i.e., wave speed, density, area). This numerical setup allowed the experimental strain-rate to be replicated in simulations to validate the strain-rate dependence of the elastic-plastic contact model. The details of the contact law and the results of the experimental and numerical comparisons will be discussed in Chapter 3.

For simulations of contact behavior, particles were only moving in one-dimension along the axis of the excitation. Therefore, it was assumed that the particles do not rotate or translate off-axis, reducing the dynamics to fully 1D interactions. The additional degrees of freedom were removed from simulations in order to dramatically decrease computational time. Time step convergence studies were performed and a time step of 5×10^{-8} seconds was used for all one-dimensional simulations. When the time steps were halved again, numerical values changed by no more than 0.1%. In DEM studies of elastic particles, time steps are typically determined by checking that energy is conserved; if the numerical errors are too large then there will be artificial loss of energy. For the elastic-plastic particles simulated in this work, we are intentionally dissipating energy, and therefore we cannot use energy conservation as a means of determining a suitably small time step and we must use a convergence study instead.

Discrete Element Method Modeling for One-Dimensional Granular Chains

DEM simulations were also used to simulate long chains of spherical particles in one-dimension. The results of all simulations and experiments of 1D chain will be discussed in Chapter 4. In DEM simulations of 1D chains of spheres, the initial conditions selected specified either the velocity or the force profile of the first sphere in the chain. When simulating Hopkinson bar experimental tests, we again used the velocity profiles measured experimentally at the end of the incident bar as initial conditions for the first particle in the chain. Additional simulations were performed to investigate the general properties of waves in elastic-plastic granular crystals. For these simulations, it was desirable to use a more regular square velocity or force pulse applied to the first sphere. By applying a known force for a specified duration,

we could more easily compare the dynamics of wave propagation between granular chains with particles comprised of different constituent materials. After the initial pulse was applied, the particle could move freely like the other particles in the simulations. The final sphere was again assumed to be in contact with a 1D linear medium having the same properties as the transmission bar used in experiments. When processing the numerical results, we calculated the local wave speeds by taking the difference in the arrival times of the stress wave at each subsequent particle and dividing it by the distance between those particles. The arrival time for each particle was defined as the time for which the particle reached 1% of the initial velocity of the first particle, or 1% of the maximum velocity of the first particle.

For simulations of 1D chains of particles, it was again assumed that the particles do not rotate or translate off-axis, allowing the extra degrees of freedom to be removed from simulations to improve simulation speed. The same time step of 5×10^{-8} seconds was used for all one-dimensional simulations as was used in the single contact simulations. The same convergence test was used to find a suitable time step as for the single contact simulations. This time step was found to be appropriate to minimize the numerical error for all materials and particle sizes simulated in this work and was therefore used for all further simulations.

Discrete Element Method Modeling for Higher Dimensional Granular Crystals

While it is trivial to extend the 1D DEM approach to two and three dimensions, some of the assumptions required do not necessarily hold in higher dimension. For example, in our formulation there is no consideration of friction between the particles. In 1D, the particles cannot slide past one another, whereas oblique impacts will often occur in 2D and 3D. We also assumed that particles would not turn and that they would always contact each other at the same point, which might not remain valid with more degrees of freedom. In order to ensure that the neglected effect were indeed negligible in the dynamics of these materials, we performed multiple types of experimental validation on a variety of types of granular crystals. All experimental validation and additional simulations of 2D and 3D granular crystals will be discussed in Chapter 5.

The first 2D simulations required replicating an experiment involved a sliding impacting rig for 2D arrays of elastic-plastic particles which will be described in Subsection 2.2.3. These experiments involved hexagonally packed particles with

material properties of the types of materials used in experiments. The boundary conditions of the experiment are applied to the simulations by placing rigid walls on 3 sides of the simulated particles. Due to symmetry, compressing a particle against the rigid wall requires the same force as compressing two identical particles by twice the displacement between the particle and the wall. The impactor bar is treated as a rigid flat particle whose force-displacement relationship is the same as the rigid walls, but whose mass, positions and velocity are tracked in the same fashion as the other particles. Because no particles can rotate in the simulations, the impactor bar is also assumed to always remain horizontal relative to the sample's front face. The impactor bar is given the measured mass and initial velocity extracted from each experiment.

Additional experiments were performed for validation of 3D DEM as well using a drop weight tower experiment which will be described in Subsection 2.2.4. For these simulations, two layers of 3D hexagonally close packed (HCP) spheres of the materials used in experiments were simulated during an impact of a rigid polygonal surface with the mass of the weight used in experiment. Interactions between particles and rigid boundaries have the same force-displacement relation as a particle interacting with an identical particle due to symmetry. Rigid flats were incorporated into the numerical system by defining a polygonal boundary, a mass, and an initial velocity. The base was given no initial velocity and an infinite mass, forcing it to remain stationary throughout simulations, while the impacting tip was given the same mass and velocity as the experimental impactor. No boundary conditions were applied to any of the individual particles and they were free to escape after impact of the rigid surface in any direction as in the experimental setup.

For general investigations of wave propagation properties in uniform 1D, 2D, and 3D systems, the impacts on semi-infinite half spaces of model materials were simulated using periodic boundary conditions. In the 1D, 2D, and 3D systems, 50 layers of close-packed particles were arranged in the z-direction. A schematic of the arrangements for 1D, 2D, and 3D simulations is shown in Figure 2.2. For 1D, a single chain of 50 particles was used. In the 2D and 3D systems, periodic boundary conditions were implemented into the numerical scheme by assigning particles on the boundary a periodic complement on the opposite boundary with which inter-particle forces were shared. The 2D simulations consisted of 50 hexagonally packed layers in the z-direction with five particles across the width in the direction of periodicity. The 3D simulations consisted of 50 layers of HCP spheres in the z-

direction with hexagons of three particles per side in the plane of periodicity. No boundary conditions were applied to the bottom layer.

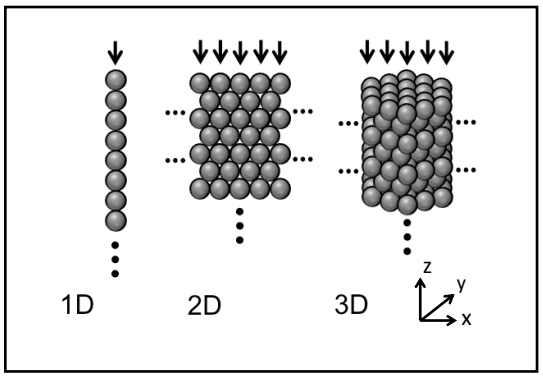

Figure 2.2: Schematics of numerical setup of particles for investigation of wave properties in 1D, 2D, and 3D materials composed of elastic-plastic particles. For all simulations, waves propagated in the z direction. In 2D simulations, hexagonal packing was used and periodic boundary conditions were applied in the x direction. In 3D simluations, hexagonally closed packed (HCP) crystal structure was used and periodic boundary conditions were applied in the x and y directions.

For these simulations, force pulses of a material dependent amplitude were applied to each particle in the top layer: a single particle for 1D, 5 particles for 2D, and 17 particles for 3D. Local wave speeds after impacts were calculated by taking the arrival time of the wave to each layer divided by z-distance between subsequent layers. Arrival times at a given particle were taken to be when the particle's velocity reached 1% of its maximum velocity during the initial impact.

2.2 Experimental Methods

2.2.1 Hopkinson Bar Experiments for Single Contacts

In order to experimentally validate the model at intermediate strain-rates, we used a split Hopkinson compression bar [16, 17, 77]. A schematic diagram of the experimental setup is presented in Fig. 2.3. Maraging steel bars of 19.05 mm diameter were used for the incident, transmission, and striker bars. Copper pulse shapers were sometimes used in order to vary the strain rate and a clay momentum trap was used to prevent reflections of the stress waves after completion of the experiment. Two identical partial spheres (either hemispheres and 3/4 spheres) of diameter 6.35 mm were placed in contact between the incident and transmission

bars. In experiments to determine the behavior of individual contacts between particles, partial spheres of stainless steel 440c, stainless steel 302, and aluminum 2017 were tested under various loadings with the amplitude of the incident stress wave controlled by varying the pressure driving the striker bar. Using a 10 cm striker bar, pressures varied from 50 kPa to 125 kPa, inducing striker bar velocities of around 10 to 25 m/s before impact.

Figure 2.3: A schematic of the Hopkinson bar setup used to experimentally obtain the force-displacement relation at the contact between two hemispherical particles.

The velocity profile at the end of the Hopkinson bar is given as a function of the strains measured by the incident strain gauge during the incident and reflected pulses:

$$v_{\text{bar}}(t) = c_i\big(-\varepsilon_i(t) + \varepsilon_r(t)\big), \tag{2.3}$$

where c_i is the elastic wave speed in the Hopkinson bar and ε_i and ε_r are the strains during the incident and reflected pulses. The incident strain is translated forward in time by c_1 times the distance from the gauge to the end of the bar, while the reflected strain is translated backwards in time by the same amount such that they are summed when both are at the end of the bar. A dispersion correction was applied to the incident and reflected waves as in [77] in order to account for dispersion in the 1D bar, yielding smoother applied velocity profiles. This velocity profile versus time is then applied to the first particle in simulations of the contact behavior of two particles. The materials properties of the transmission bar are used to define the infinite 1D material which is assumed to be in contact with the 2nd particle in simulations.

2.2.2 Hopkinson Bar and Laser Vibrometer Experiments for 1D Elastic-Plastic Chains

The Hopkinson pressure bar was also used to impact chains of metallic spheres. A schematic of the experimental setup is shown in Figure 2.4. Strain gauges on the incident and transmission bars measured the incident, reflected, and transmitted stress waves. The spheres were held between the bars and confined to move only along the axis of the chain by a 3D printed plastic tube. A truncated (3/4) sphere was used as the first particle in flat contact with the end of the incident bar. This ensured that the first particle had the same velocity profile as the end of the incident bar, as measured by the strain gauges, and that all energy was dissipated in the contacts between spheres. The flat side of the first particle remained in contact with the incident bar through the duration of the data acquisition. A copper pulse shaper was used between the striker and incident bar to ensure repeatable impacts for all experiments.

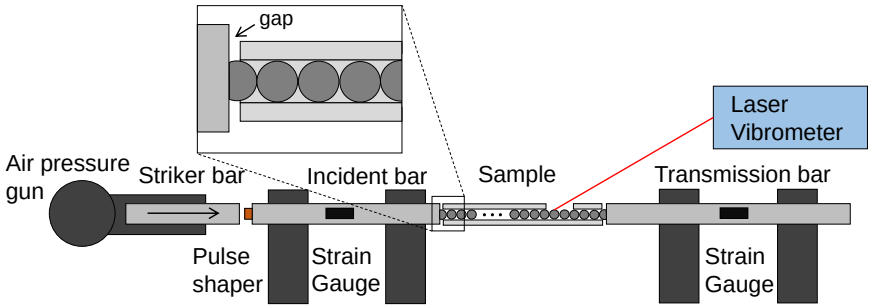

Figure 2.4: A schematic of the Hopkinson bar setup used to investigate the behavior of 1D chains of elastic-plastic particles. A laser vibrometer was used to measure the particle velocity of a particle towards the end of the chain. Most of the impact is dissipated within the chain and so very little is observed in the strain gauge on the transmission bar, requiring the laser vibrometer to extract information about the character of the wave within the material.

The spherical particles used in experiments had a diameter of 6.35 mm and were made of stainless steel 440c, stainless steel 302, aluminum 2017 and brass 260, purchased from McMaster-Carr. Truncated (3/4) spheres of the same materials were purchased from BalTec. Sample holders were 3D printed with an Objet500 Connex printer using a rigid plastic, VeroBlack, and were designed to have an inner diameter the same as the spheres. The tubes ensured that the chains of spheres remained aligned along the axis of the Hopkinson bar without rattling, but did not

create appreciable friction. The 3D printed inner surface was thoroughly cleaned after printing and spheres could slide freely within the tube without the need for lubrication. To avoid the transmission of stress waves through the holder, the length of the tube was made slightly shorter than the chain of spheres, forming a small gap between the holder and the bars (see inset of Figure 2.4). Because the stress waves were not transmitted through the plastic holder, the holder was not included in the simulations. Vaseline was used to adhere the truncated spheres to the incident and transmission bars to ensure they were centered and aligned. The tube containing the remaining spheres was then placed between the two aligned truncated spheres. The rigid plastic tube was stiff enough but light enough that it could support its own weight without sagging while held firmly between the incident and transmission bars, ensuring no gaps between spheres. During the experiments, it was observed that the initial axial pressure wave was fully transmitted through the 1D chain before any off-axis motion occured due to buckling of the sample. It required multiple reflections of the wave for the equilibrium forces from the Hopkinson bar to reach the force required to buckle the sample, at which time, data was no longer being collected.

We used strain gauges on the incident and transmission bars to detect the incoming, reflected and transmitted waves after interaction with the granular chains. In addition, a Polytech laser vibrometer was used to measure the velocity profile of one of the spheres in the chain. This direct measurement of the dynamics of particles inside the sample allowed testing longer chains and enabled a more direct comparison of the experimental results with numerical simulations. The laser vibrometer data and strain gauge data were both supplied to a data acquisition computer such that they were triggered together, ensuring that the time recorded by all sensors was synchronized. We tested chains of fifty spheres and twenty five spheres, consisting of identical particles (i.e., uniform chains) and periodic arrangements of particles alternating between spheres of two different materials (i.e., dimer chains). In all configurations studied, the length of the chains was such that the forces transmitted through the chains were significantly reduced, and the signal measured by the strain gauges in the transmission bar could be indistinguishable from the experimental noise. Therefore, the laser vibrometer was used to measure the particle velocity of the 40th sphere throughout the impact for 50-particle chains and 15th sphere for 25-particle chains. The laser was focused through a narrow gap in the 3D printed tube holder onto a small piece of reflective tape adhered to the surface of the sphere. The laser was aligned along the axis of the chain such that it could measure the

velocity of the sphere as it displaced during the experiment. Any off-axis motion would have destroyed the signal to the laser, which verified that our experiment remained one-dimensional during the measurement period and any buckling of the sample occurred after the initial wave passed.

2.2.3 Sliding Rig for Impacts on 2D Arrays

A sliding impactor rig was designed in order to perform impact experiments on a 2D array of metallic spheres. The entire experiment lay flat on the surface of an optical table. The slider was guided by Teflon linear bearings along two aluminum t-slotted beams. It was propelled by four stiff elastic bands, two on each side of the linear bearings in order to apply forces symmetrically. The sample sat in a holder rigidly attached to the optical table between the two t-slotted beams. Attached below the slider, was a hardened stainless steel 440c impacting bar which was aligned with the front edge of the sample and would detach from the slider upon impacting the sample. By detaching from the slider, the impact energy could be characterized with just the mass of the impactor bar and its speed just before the impact.

Using a winch, the slider was retracted 1 m and secured using a Sea Catch toggle release [ref] mounted to the optical table. The elastic bands were each rated to 280 N/m and therefore the four bands provided 1120 N of force on the sliding rig at full extension. When the Sea Catch mechanism was released, the slider would accelerate to around 20 m/s before the impacting bar struck the sample with some variation due to friction in the Teflon linear bearings, initial alignment of the sliding rig, and differences in the stiffness of the four bands. In order to measure the exact velocity of the slider at the time of the impact, two pairs of infrared LEDs and detectors on a breadboard mounted to the optical table were used as timing gates. The drop in voltage of each infrared detector as the sliding rig passed in front of the LED was amplified and measured on an oscilloscope giving the travel time between gates. The infrared gates were separated by 2.5 cm with the second gate aligned with the location of the impact. Therefore, the average speed of the impacting rig could be calculated over the 2.5 cm before impacting the sample and assumed to be the speed of the impacting bar at the time of impact. Figure 2.5a shows a schematic of the sliding 2D impactor rig along with a photograph in Figure 2.5b.

The samples consisted of 263 hexagonally-packed metallic spheres with diameter 6.35 mm. The spheres were arranged into 15 rows such that the final sample measured 11.4 cm across and 8.3 cm deep. Spheres of multiple materials were

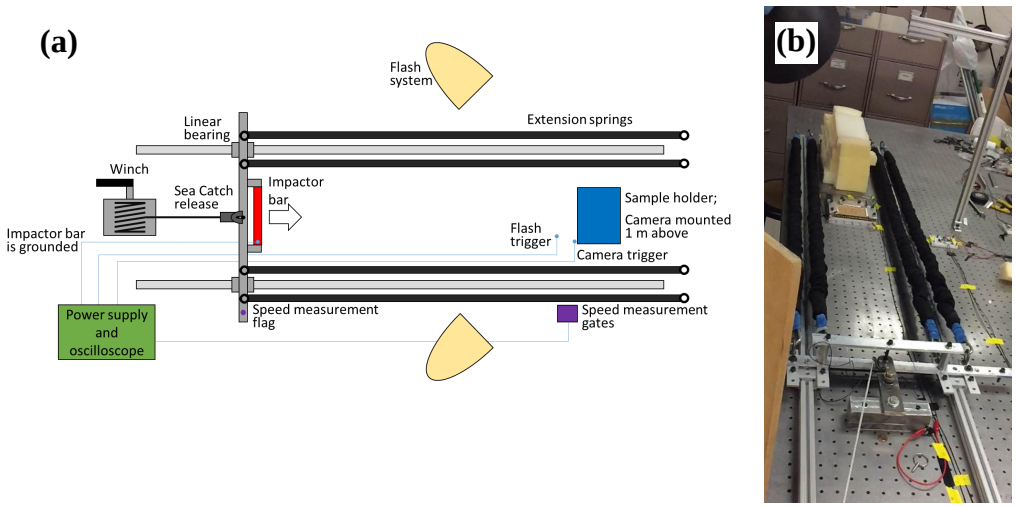

Figure 2.5: (a) Schematic of experimental setup. (b) Photograph showing the experimental setup with extension springs stretched.

tested including stainless steel 440c, stainless steel 304, and brass 260 purchased from McMaster-Carr. Experiments were performed on uniform arrays of a single material as well as arrays containing a wedge of spheres of another material in order to test the behavior of the impact wave impinge on an oblique interface between two materials. The spheres of the alternate material were placed in the bottom right corner of the sample array in an equilateral triangle with 10 spheres per side. The 2D array sat on an aluminum plate and was constrained on three sides by stainless steel 440c bars that could be individually aligned and tightened in order to ensure that the 2D array was fully close-packed. The sample was enclosed on top by a thin clear acrylic window. All sample supports were positioned such that the leading half first row of spheres was fully exposed to the oncoming impactor bar with supports just reaching the mid-section of the spheres. In order to ensure that the sample remained intact and fully close-packed before the impact a thin strip of electrical tape was placed along the front surface of the acrylic window and onto the tops of the first row of spheres, but without covering the contact point between the impactor bar and the particles. Figure 2.6a shows a schematic of the sample including the location of the oblique wedge of the alternate material and the supporting walls along with a photograph of a sample in Figure 2.6b.

A Shimadzu HPV-X camera was used to observe the positions of about half the spheres in the sample. The camera was mounted on an arm approximately 1 m directly above the sample with a 90 mm lens, such that the field of view was about

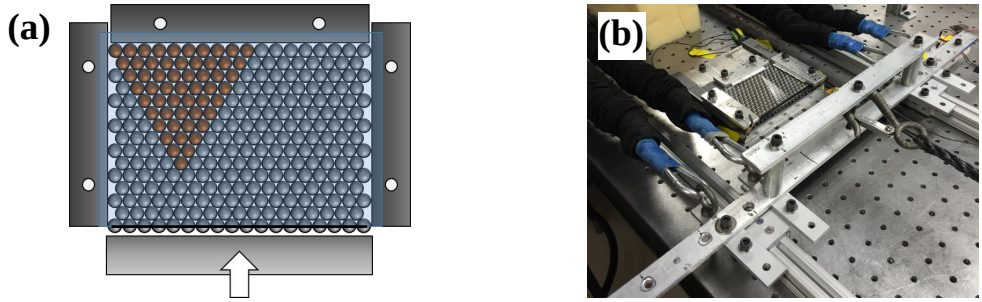

Figure 2.6: (a) Schematic showing details of sample container with spheres arranged in 60 degree wedge of brass spheres within an array of stainless steel 440c spheres. (b) A photograph showing the details of the sample and slider.

half the size of the sample. The high-speed camera was able to record 256 frames of 400 x 250 pixel images at a frame rate of 333,333 frames per second with each particle about 30 pixels across (225 μm/pixel). A representative frame taken by the high-speed camera just before an impact is shown in Figure 2.7a. Because the exposure time is so small, a short-duration, high-intensity flash lighting system was required. Triggering of the high-speed camera and flash system were performed by grounding the impactor bar and having the bar make contact with wires precisely placed in front of the sample. When the impactor bar made contact with each of these wires, the trigger signal was driven from +5V to ground at the correct time. The flash system required approximately 1 ms to reach full intensity and could stay illuminated for around 5 ms before beginning to dim. Therefore, the trigger wire for the flash was placed 4 cm in front of the sample such that 2 ms would pass between triggering the flash and the impact assuming the bar was traveling 20 m/s. The high-speed camera continuously records into a buffer, but only saves the 256 frames immediately following the trigger signal. The trigger wire for the camera was placed on the sample holder about 1 mm from the front of the sample. Therefore, about 50 μs was recorded before the impact allowing the speed of the impacting bar to be verified prior to impact. Depending on the constituent materials, the experiment duration could be up to 400 μs; the 768 μs total recording duration (256 frames at 333,333 frames per second) was therefore enough to capture the full experiment duration with enough margin to account for any error in the timing of the triggering.

Positional data from each particle in each frame is extracted by performing 2D image correlation using a 30x30 pixel kernel comprised of a representative particle

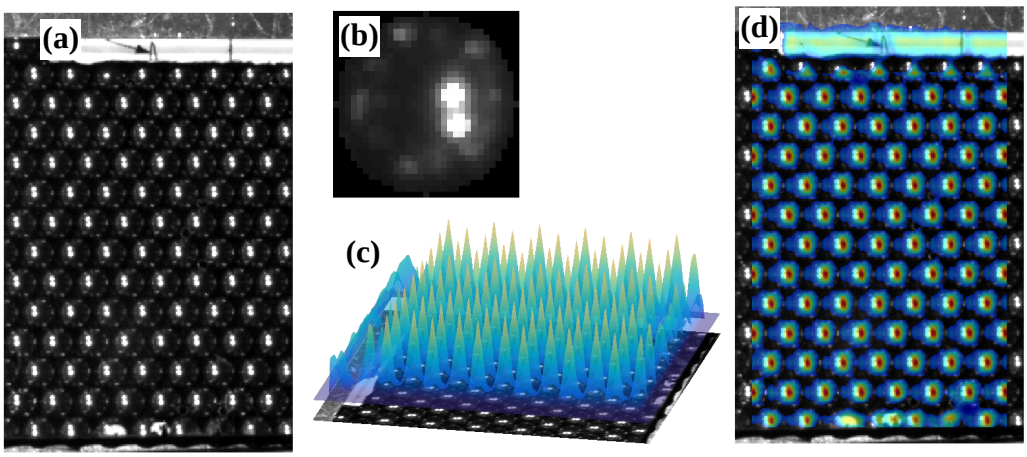

Figure 2.7: (a) A representative frame from the high-speed camera taken just before an impact. (b) The image of a particle used as the kernel for 2D correlation. (c),(d) Surface of the 2D correlation matrix overlaid onto the frame from which the correlation was calculated.

from the initial frame. An image of the kernel particle used for the analysis of one experiment is shown in Figure 2.7b. Using MATLAB's *corr2* function, the 2D correlation for every 30 x 30 subimage centered within the image is calculated to obtain a 2D correlation matrix. The 2D correlation matrix of the frame shown in Figure 2.7a is shown as a surface plotted above the frame in Figure 2.7c and 2.7d. The centroid of each peak within the correlation matrix was calculated to get the positions of each of the particles in the image. Each particle was then tracked through each of the 256 frames to get the time history of the positions of the particles.

2.2.4 Drop Weight Tower Experiments for 2-Layer 3D Granular Crystals

Increasing dimensionality from 1D to 2D introduced the possibility of tangential forces between particles requiring significant experimental validation. However, increasing the dimensionality again from 2D to 3D does not actually introduce new physics. It does, however, introduce many added complexities in the possible geometric crystal arrangements and significant added difficulty in instrumentation for experiments. It is very difficult to probe the interior of a three-dimensional material because it is surrounded by more material. Nevertheless, we performed preliminary experiments towards the investigation of 3D granular materials using a drop weight tower on two stacked layers of particles. Because there are multiple ways to densely pack spheres in 3D we performed experiments on two layers of both hexagonally close packed (HCP) and face centered cubic (FCC) crystal arrangements

of particles. A schematic of the HCP arrangement of particles is shown in Figure 2.8a. We also performed experiments on arrangements of particles with two types of materials. However, due to limitation of the experimental setup, only brass and softer stainless steel 304 could be used and their properties are relatively similar. A hexagonal impactor tip was used to impact the center of the 2-layer crystal with an area 5 particles wide. The layers were wide enough (21 particles across) such that the impact wave did not reach the sides of the particles during the experiments so boundary effects would not affect the behavior.

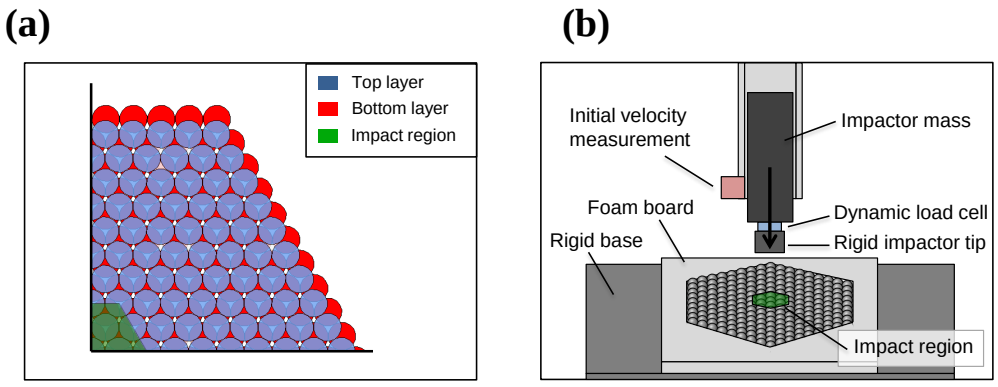

Figure 2.8: (a) A schematic showing one quarter of the arrangement of both layers of particles for the drop tower experiments as well as the location in which the impactor makes contact. (b) A schematic of the drop tower setup.

A drop weight tower at NASA Langley was used from heights of 0.46 m and 0.81 m to impact the granular crystals with impact velocities of 3 m/s and 4 m/s as measured directly above the sample with some variation due to friction losses during operation. A schematic of the experimental setup is shown in Figure 2.8b. The 2.3-kg impactor consisted of a cylindrical mass attached to an Instron Dynatup 90 kN load cell with flat tips made of hardened stainless steel 15-5. The weight of the impactor tips was minimized in order to reduce the internal vibrations measured by the load cell. The impactor tip section was hexagonal with side lengths of 12.7 mm in order to impact the selected area on the sample as shown in Figure 2.8a shaded in green color.

The materials used in experiments were 6.35 mm diameter spheres of Brass 260 and Stainless Steel 302 purchased from McMaster Carr. Foam board was used to contain the spheres such that all spheres would be in initial contact without providing

any significant structural stiffness during the impact. The spheres were arranged on a large stainless steel 15-5 base which was rigid compared to the softer spheres.

Chapter 3

CONTACT MODEL

Earlier work on elastic-plastic contact deformation focused on the contact of a sphere and a rigid half-space to analyze contact between identical spheres [10–13]. This approach is useful for many practical applications of spheres impacting flat surfaces and also, by symmetry, the collision of identical spheres. These works used various simplifying assumptions for the changes in the distribution of pressure over the contact surfaces to develop empirical force-displacement models. In these models, several empirical parameters are typically used to fit experimental curves and capture aspects of the deformation process that cannot be directly derived analytically. Such models have been used to inform experiments in a limited range of material properties, geometries, or loading cases [5–9], but their restrictive assumptions make them unsuitable for a general predictive analysis. Furthermore, a model that is dynamically valid for materials that exhibit strain rate dependence has been elusive.

In this chapter, we describe the elastic-plastic contact model we developed to describe the compression of elastic-plastic spherical particles, which incorporates material strain rate dependence. The model extracted the quasistatic contact response from finite element (FEM) analysis by inputting only the material properties and geometry of the spheres. The strain rate dependence was incorporated in the model by introducing a Johnson-Cook type strain-rate dependence into the elastic-perfectly plastic material model determined through FEM analysis. We validated this model with experiments where the contact between two spheres was excited dynamically in a Hopkinson bar. We tested the model for a range of materials and loading conditions, varying the spheres material properties and impact velocities.

The content of this chapter has been partially adapted from:
Hayden A. Burgoyne and Chiara Daraio. "Strain-rate dependent model for the dynamic compression of elastoplastic spheres." *Physical Review E* 2014, **89**(3). p. 032203.

3.1 Model Description

The quasistatic compression of an elastic-plastic spherical contact has three distinct regimes (Figure 3.1a): an elastic region (Region I), a region with a constrained plastic zone (Region II), and a region with unconstrained plasticity (Region III) [8]. In Region I, no part of the sphere has yielded and the force-displacement relationship is fully captured by the Hertzian description of the contact between two elastic spheres. Region II begins when yield first occurs in the sphere at a relative approach between the centers of the spheres δ_y. The plastic region develops initially below the surface and is fully contained within regions of deformation that are still elastic [78]. The force-displacement response in Region II can no longer be captured by the Hertzian description, but is not yet linear as initially assumed by early models [4]. Region III begins when the plastic region reaches the edge of contact surface and becomes unconstrained, at a displacement δ_p. When the contact region is fully plastic, the pressure is nearly constant and we therefore observe a linear force-displacement response [8, 78]. The plastic zone in each of the three regions is shown with representative FEM results in Figure 3.1b.

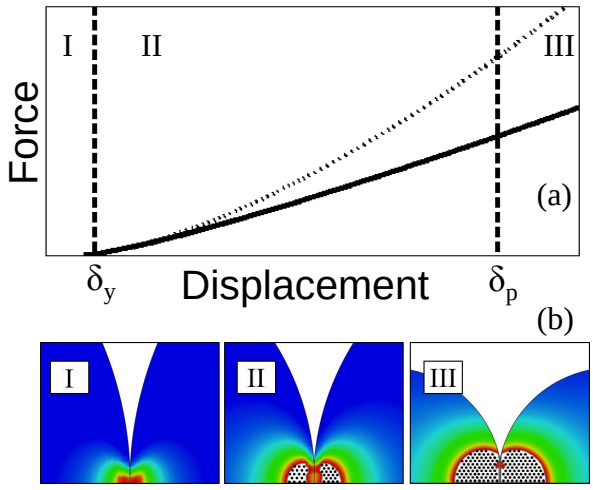

Figure 3.1: Plot of force versus displacement showing the three distinct regions during the deformation process. The dotted line is a plot of the Hertzian solution for elastic spheres. (b) Representative diagrams (obtained via finite element simulations) of the stress distributions in each of the three deformation regions. Gray represents the plastic zone.

In Region I, before the initiation of plasticity, the behavior is accurately described by the analytical solution found by Hertz [79]. The pressure over the contact area is proportional to $\sqrt{a^2 - r^2}$, where a is the contact radius and r is the polar coordinate.

Integrating the pressure field over the contact region shows that the applied normal force, F, is proportional to the distance between the centers of the spheres, δ, to the three-halves power. The force in Region I is given by [79]:

$$F = \frac{4}{3} E^* \sqrt{r^*} \delta^{3/2}, \tag{3.1}$$

with the effective Young's Modulus:

$$E^* = \left(\frac{1 - \nu_1^2}{E_1} + \frac{1 - \nu_2^2}{E_2} \right)^{-1},$$

where E_1, E_2, ν_1, ν_2 are the Young's Moduli and the Poisson's Ratio of the two materials and the effective radius as:

$$r^* = \left(\frac{1}{r_1} + \frac{1}{r_2} \right)^{-1},$$

where r_1, r_2 are the radii of the two spheres [79]. In this work, we've only considered the contact between spheres of identical radius, R, and therefore the effective radius always reduces to $r^* = R/2$. The Hertzian region ends when plasticity is first observed, which is determined using the Von Mises criterion to be at a displacement δ_y and force F_y given by [10]:

$$\begin{aligned} \delta_y &= \frac{1}{4} \frac{r^*}{E^{*2}} (1.6\pi\sigma_y)^2, \\ F_y &= \frac{1}{6} \left(\frac{r^*}{E^*} \right)^2 (1.6\pi\sigma_y)^3. \end{aligned} \tag{3.2}$$

Here, σ_y is the yield stress of the material and the constant 1.6 is determined by maximizing the J2 invariant of the axisymmetric stress distribution with respect to both angle and depth below the surface.

The onset of plasticity defines the beginning of Region II, where the contact area is still mixed elastic and plastic. The pressure field for this mixed region was proposed by Stronge [78] and can be integrated over the contact area to get a force-displacement relation of the form:

$$F = \delta(\alpha + \beta \log \delta). \tag{3.3}$$

Here, α and β are obtained imposing continuity of the force at the boundaries between Region I and III:

$$\alpha = \frac{\delta_p F_y \log \delta_p - \delta_y F_p \log \delta_y}{\delta_y \delta_p \left(\log \delta_p - \log \delta_y\right)},$$
$$\beta = \frac{\delta_y F_p - \delta_p F_y}{\delta_y \delta_p \left(\log \delta_p - \log \delta_y\right)}.$$

Since the pressure distribution in Region III is nearly constant, the force is equal to the pressure times the area of the contact:

$$F = p_0 \pi a^2, \tag{3.4}$$

where p_0 is the constant pressure and a is the contact radius. We model a^2 by taking its elastic definition and modifying it with an empirical parameter, c_2, that represents the effect of plasticity on the contact radius. Because yield causes the contact area to increase more slowly with increasing force than in the elastic case, we expect c_2 to be negative. It is given by the following relationship described by Brake [80]:

$$a^2 = 2r^* \delta + c_2.$$

In previous studies, p_0 was assumed to be $2.8\sigma_y$ [14, 80, 81]. FEM observations show that this is a reasonable assumption for many cases, but it is not valid for all materials. In this model, we take the ratio of p_0 to the yield stress to be the second empirical parameter,

$$p_0 = c_1 \sigma_y.$$

We take the displacement at which Region III begins, δ_p, to be the model's third empirical parameter. From δ_p, we can calculate the force at which Region III begins, F_p, to be:

$$F_p = p_0 \pi (2r^* \delta_p + c_2). \tag{3.5}$$

In order to determine the empirical parameters, material properties were varied within the FEM simulations over a range that includes most metals and common materials (Figure 3.2a). The quasistatic model presented here was then fit to the force-displacement results from the FEM simulations. To determine the empirical parameters, we chose an arbitrary δ_p and performed a linear regression on the FEM data for $\delta > \delta_p$ in order to determine the constants c_1 and c_2. We calculated the least-square error in the model versus the FEM results for all possible choices of

δ_p, and took the empirical constants for which this error was minimized (further described in Section 3.2).

The quasistatic model for compressive loading can be summarized in the following piecewise force-displacement relationship:

$$F(\delta) = \begin{cases} \frac{4}{3}E^*\sqrt{r^*}\delta^{3/2} & \text{for } 0 < \delta < \delta_y \\ \delta(\alpha + \beta \log \delta) & \text{for } \delta_y < \delta < \delta_p \\ p_0\pi(2r^*\delta + c_2) & \text{for } \delta > \delta_p. \end{cases} \tag{3.6}$$

Unloading was shown to be a purely elastic process in previous works [17, 81–83] and here we take the formulation where the unloading force is given as:

$$F_{un} = \frac{4}{3}E^*\sqrt{r_p}(\delta - \delta_r)^{3/2}.$$

r_p is the contact radius after plastic deformation, given by:

$$r_p = \frac{4E^*}{3F_{\max}}\left(\frac{2F_{\max} + F_y}{2\pi(1.6\sigma_y)}\right)^{3/2},$$

and δ_R is the residual permanent deformation, given by:

$$\delta_R = \delta_{\max} - \left(\frac{3F_{\max}}{4E^*\sqrt{r_p}}\right)^{2/3}.$$

$F_{\max}$ and $\delta_{\max}$ are the force and displacement at which unloading begins [17].

When considering strain-rate dependent materials, previous FEM analysis showed that Johnson-Cook strain-rate dependence captures the behavior of moderate-speed sphere impact experiments [14, 15]. The Johnson-Cook material model relates the yield stress to the strain-rate, with dependence given by:

$$\sigma_y^* = \sigma_y(1 - C \log(\dot{\varepsilon}/\dot{\varepsilon}_0)). \tag{3.7}$$

Here $\dot{\varepsilon}$ is the strain rate, $\dot{\varepsilon}_0$ is the quasistatic strain rate at which σ_y is measured, and C is an empirical parameter determined experimentally [18].

There were two considerations in order to incorporate strain-rate dependence into the quasistatic contact model presented above: first, we had to define strain-rate in the contact problem and, second, we also needed to determine the dependence

of the model's parameters on the yield stress of the material. No previous attempt had been made to incorporate rate dependence into an analytical model for the force-displacement relationship, since all knowledge of local strain-rates is lost in the analytical description. Here, we defined strain-rate by considering the relative velocity of approach between the two spheres at each time step, as:

$$\dot{\varepsilon} = \frac{v_2 - v_1}{r_1 + r_2}, \tag{3.8}$$

where v_2 and v_1 are the velocities of the centers of mass of the two spheres and r_1 and r_2 are the radii of the spheres. We then calculated a new σ_y^* at every time step that was modified by the rate at which the spheres were moving together. Once the dependence on the yield stress was determined, σ_y^* could be used to calculate new dynamic empirical parameters and update the contact model as the simulation progresses.

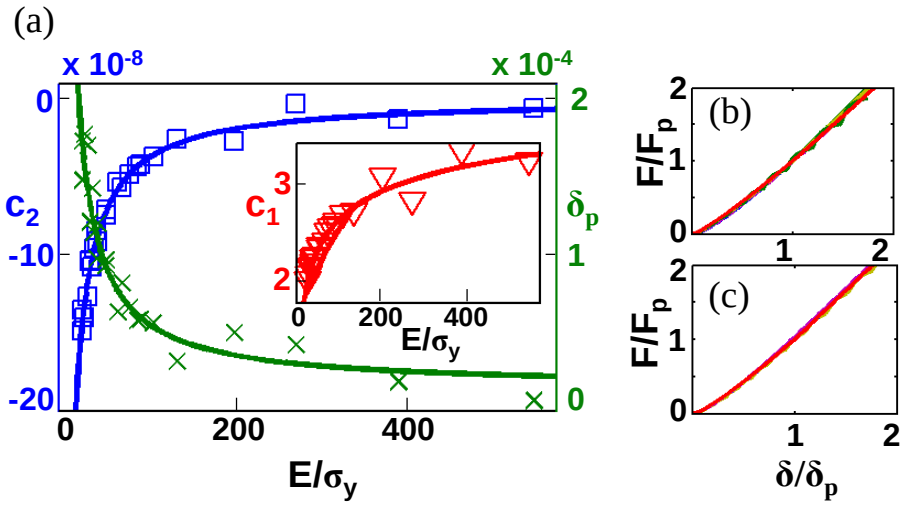

Figure 3.2: (a) Plot of the model's three empirical parameters versus the ratio E^*/σ_y with markers showing the results of FEM and the curve fittings used in the model. (b) Multiple plots of force versus displacement taken from FEM results and the results of the model for different 4 different values of the ratio E/σ_y, normalized by the force and displacement at which Region III begins. (c) Plots of force versus displacement taken from FEM results and results of the model for three different sphere diameters, 6.35 mm, 9.525 mm, and 12.7 mm, normalized by the force and displacement at which Region III begins.

3.2 Experimental Validation and Modeling Results

Using FEM, we performed quasistatic compression of 6.35 mm diameter hemispheres for a variety of material parameters. The simulations were performed for

the following cases: (i) spheres with identical Young's Modulus, yield stress and radius; (ii) spheres with different Young's modulus, but identical yield stress and radius; and (iii) spheres with different yield stress, but identical Young's modulus and radius. The force-displacement data obtained with FEM were then fitted to the model from Equation 3.6 to extract empirical parameters for each simulation. The process for fitting the model to the FEM data was as follows: first, each of the 1000 displacement steps taken by the FEM simulations was considered as a possible δ_p. Because the model is linear after δ_p, a linear regression was fit to all data for which $\delta > \delta_p$. This linear regression was used to calculate the c_1 and c_2 for that choice δ_p using Equation 3.6. Using these three possibilities for the empirical parameters, the least-square error of the model versus the FEM simulation data was calculated over the entire data from the simulation. Finally, the set of parameters with the smallest least-square error was taken as the appropriate empirical parameters for that set of material properties. The empirical constants for each set of material properties are represented by the markers in Figure 3.2a.

The results of these studies showed that the values of the empirical constants did not depend on the magnitude of material properties, but rather on the ratio of the effective Young's modulus to the yield stress. After fitting the model to a number of FEM simulations as previously described, we performed a regression analysis to find general empirical functions to describe the parameters' dependence on the ratio of Young's modulus to yield stress (see solid lines in Figure 3.2a). These empirical functions for the compression of 6.35 mm diameter hemispheres are given as:

$$\begin{aligned}
\delta_p &= \left(0.00428\left(\frac{E^*}{\sigma_y}\right)^{-1} + 1.47\times10^{-5}\right)\left(\frac{r^*}{0.00159}\right),\\
c_1 &= -6.76\left(\frac{E^*}{\sigma_y}\right)^{-0.137} + 6.30,\\
c_2 &= \left(-3.99\times10^{-6}\left(\frac{E^*}{\sigma_y}\right)^{-1} + 1.01\times10^{-9}\right)\left(\frac{r^*}{0.00159}\right)^2,
\end{aligned} \tag{3.9}$$

where E^*/σ_y is the non-dimensional ratio of effective Young's modulus to yield stress and r^* is the effective radius of the sphere (in meters) given earlier in the model description. The empirical parameters scale with the effective radius as predicted by dimensional analysis, allowing for the FEM results to be scaled to other sphere sizes.

Using this set of empirical functions, we modeled the quasi-static compression

of spheres with different material properties and sizes. Figure 3.2b shows the FEM results and the model for four different values of the ratio of effective Young's modulus to yield stress, normalized by the force and displacement at which Region III begins. In each case, the FEM results and the model are nearly indistinguishable. Figure 3.2c shows the normalized FEM and model results for three different sphere radii. In these cases the same empirical functions derived for the 6.35 mm spheres were used with the simple scaling given in Equation 3.9. Again the model results are nearly indistinguishable from the FEM simulations.

With the empirical functions in Equation 3.9 and the elastic-plastic contact model given in Equation 3.6, we had an explicit relation for the yield stress of the material on the force. Therefore, we could use Equation 3.7 and Equation 3.8 to modify the model based on velocity of approach of the two spheres. We performed FEM simulations for the compression of two hemispheres with Johnson-Cook strain-rate dependence at a constant relative velocity and compared it with model's predictions. Figure 3.3a shows the results of constant strain-rate FEM analysis versus the analytical model using the same velocity of approach and Johnson-Cook parameters. This figure shows the simulation of 6.35 mm Stainless Steel 440c hemispheres with material properties given in Table 1 and Johnson-Cook parameters: $C = 0.04$ and $\dot{\varepsilon}_0 = 0.001$. The inset in Figure 3.3a shows the same plots normalized by the force and displacement at which Region III begins (in this case all curves are overlapping). The model accurately captured the FEM behavior over an extreme range of effective strain-rates, from 0.001 (quasistatic) to 10,000 (Figure 3.3a). Despite losing the information about local deformations and local strain-rates, the global strain-rate defined above, captured the dynamics suitably.

Because this model remained valid over a range of strain rates, we could apply it to simulate dynamic events that typically have large variations in strain rates like impacts of two spheres and Split Hopkinson Bar experiments. Figure 3.3b shows the results of FEM analysis of two identical 6.35 mm Stainless Steel 440c spheres impacting with various initial velocities and compares the force-displacement relationship with a DEM simulation of the same event using the model including strain-rate dependence and the model without strain-rate dependence.

During a Hopkinson bar compression test, strain rate varies greatly. In order to simulate the event in DEM using the strain-rate dependent empirical model, force versus time measurements taken directly from the experiments were applied to the first particle. The second particle was assumed to be in perfect contact with a

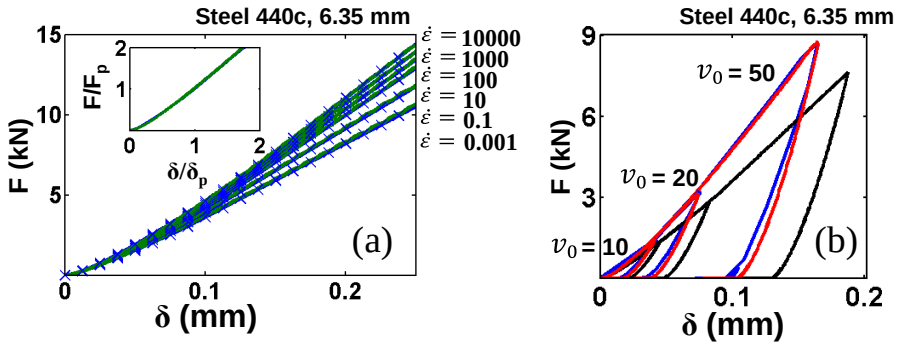

Figure 3.3: (a) Plot of force versus displacement for compression at various constant strain rates. Green lines represent the FEM results and blue lines and crosses represent the results from the model. The inset shows the same plots normalized by the force and displacement at which Region III begins. (b) Force versus displacement plots during the impact of two identical spheres with various initial velocities. Red lines represent the FEM data, blue is the DEM model with strain rate dependence, and black lines represent results from the DEM model without strain rate dependence assuming quasistatic loading.

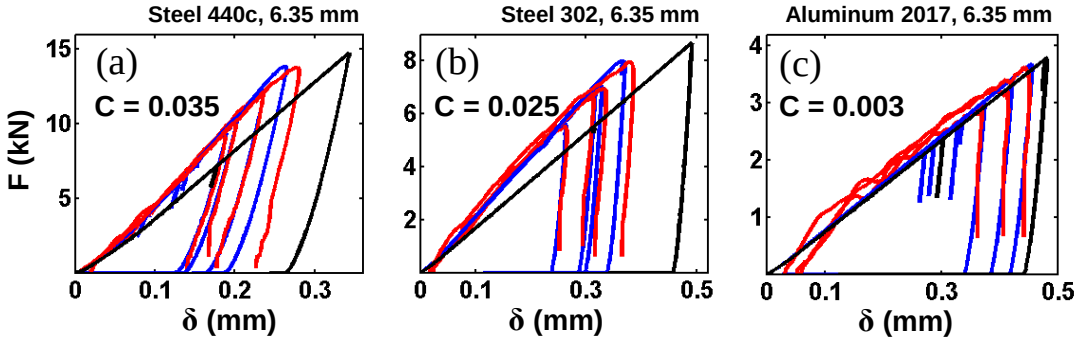

Figure 3.4: Plots of force versus displacement for experimental results (red), results using the strain rate dependent model for DEM (blue), and results using the model without strain rate dependence (black). Materials used are (a) Stainless Steel 440c, (b) Stainless Steel 302, and (c) Aluminum 2017.

one-dimensional linear media with the wave speed and density properties of the experimental transmission bar. The full experimental and numerical setup was discussed in Chapter 2.

We compared the DEM simulation's force-displacement results to the Hopkinson bar experimental results for a number of different strain rates and for a number of different materials. Figure 3.4 shows the results of the comparison. The two stainless steels tested (302 and 440c) exhibited relatively large strain-rate dependence while

aluminum (2017-T4) showed very little. The Johnson-Cook parameter was chosen in order to capture the rate dependence of the given material and was the same throughout the entire simulations. By including dependence on the relative velocity of the two particles, we see that we could effectively simulate the behavior of strain-rate dependent materials during dynamic events.

Figure 3.5 shows two stainless steel 440c hemispheres after a hopkinson bar experiment such as those shown in Figure 3.4a. The permanent damage is clearly visible on the top surface surface of each of the hemispheres demonstrating the extent to which plastic deformation occurs and energy is dissipated.

Figure 3.5: Photograph of two stainless steel 440c hemisphere after a hopkinson bar compression experiment. Permanent plastic deformation is visible on the top surfaces of the hemispheres.

3.3 Summary of Chapter

We have presented a new model for the compression of elastic-plastic spheres. Once the model's dependence on the yield stress was determined using FEM results, a Johnson-Cook strain rate dependence was used to modify the effective yield stress based on the relative velocity of the two spheres. This method was shown to agree with both dynamic FEM simulations and experimental results using a Hopkinson bar. Our model captures well the response of the compression of spheres for a number of materials, different radii spheres, and a range of loading conditions.

Chapter 4

DYNAMICS OF ONE-DIMENSIONAL ELASTIC-PLASTIC GRANULAR CHAINS

This work focuses on the properties of the leading wave, traveling through uniform and periodic granular chains consisting of alternating particle types, in response to a long duration impact. In such a loading scenario, plasticity continues to dissipate energy at each contact, significantly affecting the dynamics of wave propagation. We also investigate the effect of plasticity on wave propagation through dimer chains of alternating materials. Recent experiments have suggested that dimer chains of elastic-plastic spheres do not exhibit the same local resonances as elastic dimer chain [44]. It was observed that the amount of energy transmitted did not depend on the mass ratio of the particles and was dominated by plasticity effects instead of local resonances.

We simulate the response of these systems using a discrete element method (DEM), which includes a strain-rate dependent model for the dynamic contact interaction of elastic-plastic spheres given in Chapter 33. We determine how the properties of the initial wave in the elastic-plastic granular chains compare to those in Hertzian chains and in chains described by a simplified linear contact law. We validate the model experimentally using a Hopkinson pressure bar coupled with a laser vibrometer. From the experimentally validated simulation results, we extract a model that relates the particles material properties to the leading wave velocity. In the dimer chains, we show the effect of local resonances on the energy transmission. We use the models to define design constraints for the creation of novel materials with engineered wave propagation properties.

The content of this chapter has been partially adapted from:
Hayden A. Burgoyne and Chiara Daraio. "Elastic-plastic wave propagation in uniform and periodic granular chains." *Journal of Applied Mechanics* 2015, **82**(8). p. 081002.

4.1 Experimental Validation of 1D Simulations

Hopkinson bar experiments were performed in order to verify that DEM simulations captured the leading wave velocity and energy dissipation properties of long 1D

chains of spheres governed by the elastic-plastic contact law show in Chapter 3. The raw forces in the incident and transmission bars as measured with the strain gauges are shown in Figure 4.1 for uniform chains of twenty five and fifty stainless steel 440c spheres. The incident and reflected force pulses were nearly identical between each experiment comprised of stainless steel 440c spheres. Stainless steel 440c had the highest yield stress of any of the materials used and therefore transmitted the most force through the chain. The transmitted force through the shorter, twenty-five particle chains demonstrated the repeatability between experiments. However, for fifty spheres, the transmitted force was attenuated to the point where noise in the strain gauges becomes very significant, as seen in the green curve in Figure 4.1. The forces were even more greatly attenuated in chains of other materials and therefore the use of the laser vibrometer was necessary to measure particle velocity late in the long chains of particles.

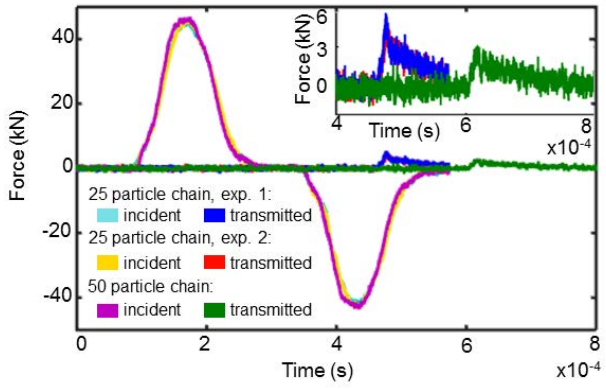

Figure 4.1: Experimentally measured forces within the incident and transmission bars of the Hopkinson bar setup as measured by the strain gauges for 25 and 50 particle chains of uniform stainless steel 440c spheres. For the two experiments with 25 particles chains, the cyan and yellow curves show the forces in the incident bar while the blue and red curves show the forces in the transmission bar. For the experiment with a fifty particle chain, the magenta curve shows the forces in the incident bar while the green curve shows the forces in the transmission bar. The inset shows the transmitted forces for the three experiments zoomed in to show repeatability between experiments as well as the influence of experimental noise.

Uniform chains of aluminum, brass, stainless steel 302 and stainless steel 440c particles were impacted using the Hopkinson bar and measured with a laser vibrometer. Both fifty particle chains and twenty five particle chains were tested. Additionally, alternating dimer chains of aluminum/stainless steel 302, aluminum/brass, brass/stainless steel 302, and brass/stainless steel 440c were tested. The velocity

profile reaching the end of the incident bar, in contact with the first sphere, was calculated from the incident and reflected waves measured by the strain gauge on the incident bar. The experimental velocity profiles are shown as the blue curves in all figures. For fifty particle chains, the velocity profile of the 40th particle was measured by the laser vibrometer. For twenty five particle chains the velocity profile of the 15th particle was measured by the laser vibrometer. All laser vibrometer measurements are shown as the yellow curve in subsequent figures. Using DEM, we simulated the response of these chains applying the experimentally measured incident velocity profiles to the first sphere in the chain. The subsequent simulated velocities of the 10th, 20th, 30th, and 40th spheres are shown as the green, red, cyan, and magenta curves, respectively, for fifty particle chains. For twenty-five particle chains, the subsequent simulated velocities of the 5th, 10th, and 15th spheres are shown as the green, red, and magenta curves, respectively.

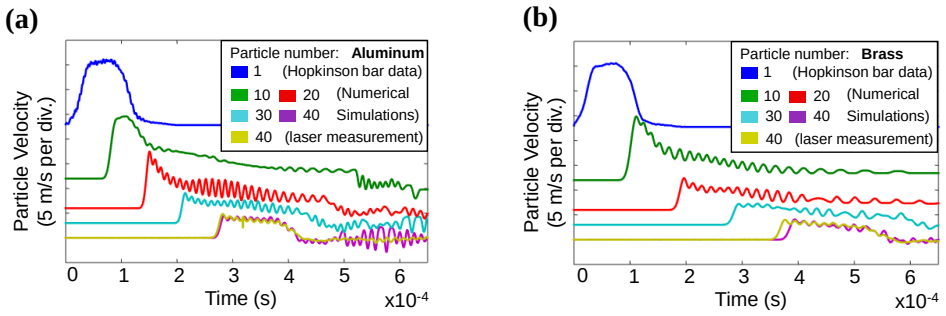

Figure 4.2: Experimental results obtained with the Hopkinson bar setup compared with corresponding numerical simulations for (a) uniform chains of fifty aluminum particles, and (b) uniform chains of fifty brass particles. The blue and red curves represent experimentally measured velocities for the 1st (blue) and the 40th (yellow) spheres. The green, red, cyan, and magenta curves represent numerical simulation for the 10th, 20th, 30th, and 40th particles in the chains.

The results of Hopkinson bar experiments on 50-particle chains of uniform aluminum and brass are shown in Figure 4.2, while the results of experiments of 25-particle chains of the same materials are shown in Figure 4.3. The DEM simulations predict the particle velocity profile of the particles observed using the laser vibrometer extremely well, capturing correctly the magnitude of the particle's velocity, the arrival time of the leading plastic wave, the arrival of the reflected wave off the end of the sample, and the local oscillations of particle. DEM using the elastic-plastic model for the contact between the spheres successfully captures the

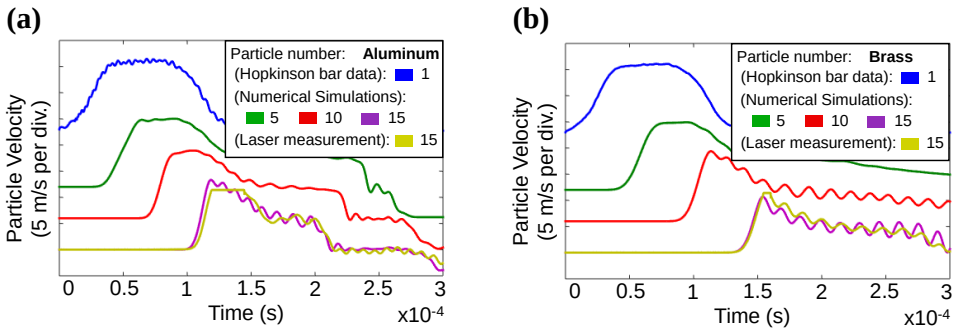

Figure 4.3: Experimental results obtained with the Hopkinson bar setup compared with corresponding numerical simulations for (a) uniform chains of twenty five aluminum particles, and (b) uniform chains of twenty-five brass particles. The blue and red curves represent experimentally measured velocities for the 1st (blue) and the 40th (yellow) spheres. The green, red, and magenta curves represent numerical simulation for the 5th, 10th, and 15th particles in the chains.

behavior of both the 15th and 40th particles, demonstrating that the contact law is applicable for a range of forces, strain rates, and material properties. However, both aluminum and brass are nearly strain-rate independent.

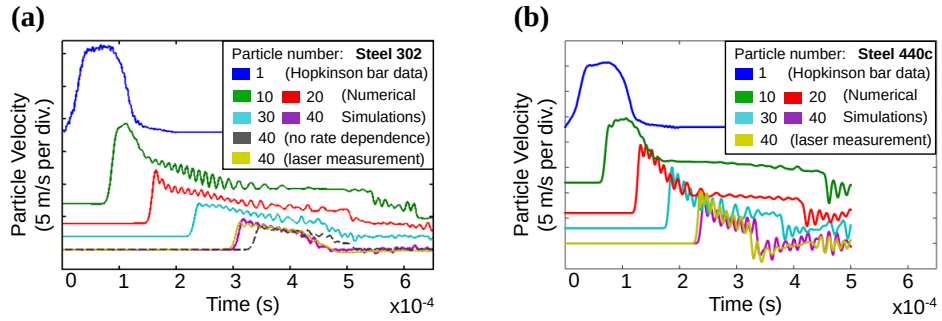

Figure 4.4: Experimental results obtained with the Hopkinson bar setup compared with corresponding numerical simulations for (a) uniform chains of fifty stainless steel 302 particles, and (b) uniform chains of fifty stainless steel 440c particles. The blue and red curves represent experimentally measured velocities for the 1st (blue) and the 40th (yellow) spheres. The green, red, cyan, and magenta curves represent numerical simulation for the 10th, 20th, 30th, and 40th particles in the chains. The dashed dark-gray line in (a) shows the numerical results obtained when strain-rate dependence is ignored and the yield stress is assumed to be the same as the quasi-static yield stress of stainless steel 302.

The results of Hopkinson bar experiments on 50-particle chains of uniform

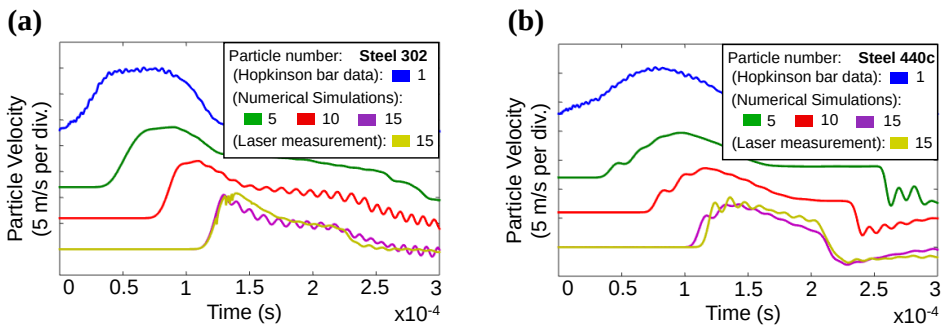

Figure 4.5: Experimental results obtained with the Hopkinson bar setup compared with corresponding numerical simulations for (a) uniform chains of twenty five aluminum particles, and (b) uniform chains of twenty five brass particles. The blue and red curves represent experimentally measured velocities for the 1st (blue) and the 40th (yellow) spheres. The green, red, and magenta curves represent numerical simulation for the 5th, 10th, and 15th particles in the chains.

stainless steel 302 and stainless steel 440c are shown in Figure 4.4, while the results of experiments of 25-particle chains of the same materials are shown in Figure 4.5. Unlike the aluminum and brass particles, the yield stresses of the two stainless steels are highly strain-rate dependent. The importance of including strain-rate dependence in materials like stainless steel 302 is evident in Figure 4.4a. When the quasi-static yield stress is used in the model without utilizing the Johnson-Cook type rate dependence, the velocity profile of the 40th sphere is not predicted correctly by the simulations, as shown by the dashed gray line in Figure 4.4a. For rate-dependent simulations of stainless steel 302, a Johnson-Cook parameter of 0.025 was used, while 0.035 was used for stainless steel 440c.

Next, in order to validate heterogeneous simulation involving multiple materials, we performed experiments on alternating chains of two materials. In this arrangement, every contact is between dissimilar materials, so it represents the most difficult case for the 1D DEM to capture. The results of Hopkinson bar experiments on 50-particle chains of alternating aluminum and stainless steel 302 particles and alternating aluminum and brass particles are shown in Figure 4.6. The results of Hopkinson bar experiments on 50-particle chains of alternating brass and stainless steel 440c particles and alternating brass and stainless steel 302 particles are shown in Figure 4.6. The vertical dashed lines in Figure 4.6a represent the arrival time of the wave for uniform aluminum, uniform stainless steel 302, and the dimer as you move from left to right. The arrival time in the dimer is slower than in the uniform

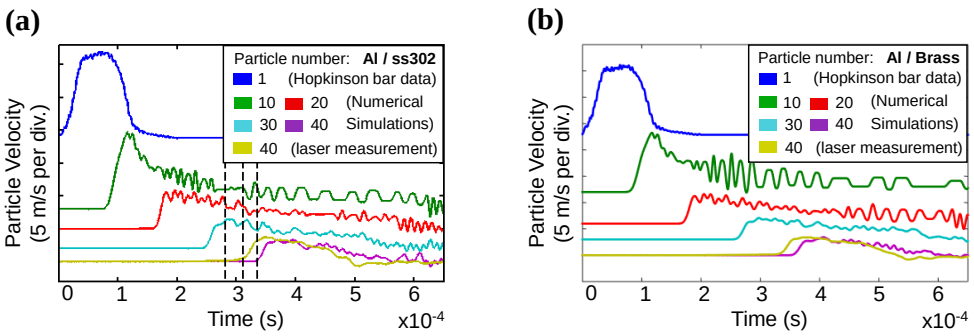

Figure 4.6: Experimental results obtained with the Hopkinson bar setup compared with corresponding numerical simulations for (a) alternating chains of fifty aluminum and stainless steel 302 particles, and (b) alternating chains of fifty aluminum and brass particles. The blue and red curves represent experimentally measured velocities for the 1st (blue) and the 40th (yellow) spheres. The green, red, cyan, and magenta curves represent numerical simulation for the 10th, 20th, 30th, and 40th particles in the chains.

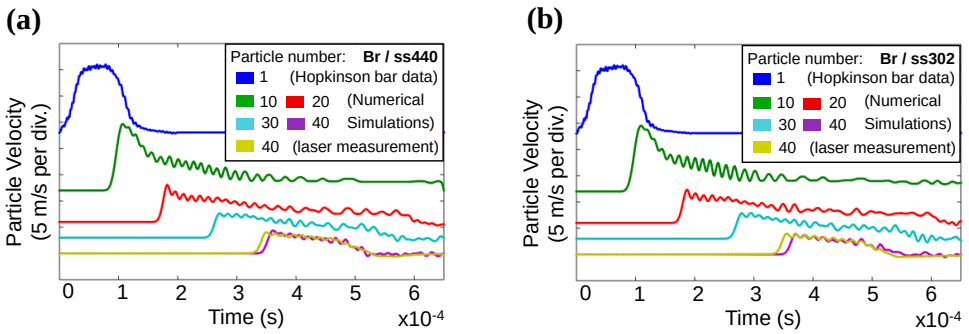

Figure 4.7: Experimental results obtained with the Hopkinson bar setup compared with corresponding numerical simulations for (a) alternating chains of fifty brass and stainless steel 440c particles, and (b) alternating chains of fifty brass and stainless steel 302 particles. The blue and red curves represent experimentally measured velocities for the 1st (blue) and the 40th (yellow) spheres. The green, red, cyan, and magenta curves represent numerical simulation for the 10th, 20th, 30th, and 40th particles in the chains.

chains of either of the constituents. The shape of the laser-measured and DEM simulated particle velocity curves match extremely well for all types of dimers even though the curves appear different in Figure 4.6 and 4.7. In the experiments shown in Figure 4.6, we do not see the very regular oscillations that we saw in experiments of uniform chains of particle or still observed in Figure 4.7. In Figure 4.6, the

aluminum is the lighter material and the softer material in which yield occurs, while in Figure 4.7, the brass is the softer material in which yield occurs but is the heavier of the two materials. This change in whether the heavier or lighter materials is the material in which yield occurs seems to control whether we see local the local particle oscillations or whether we see the flatter, less predictable particle velocity profile.

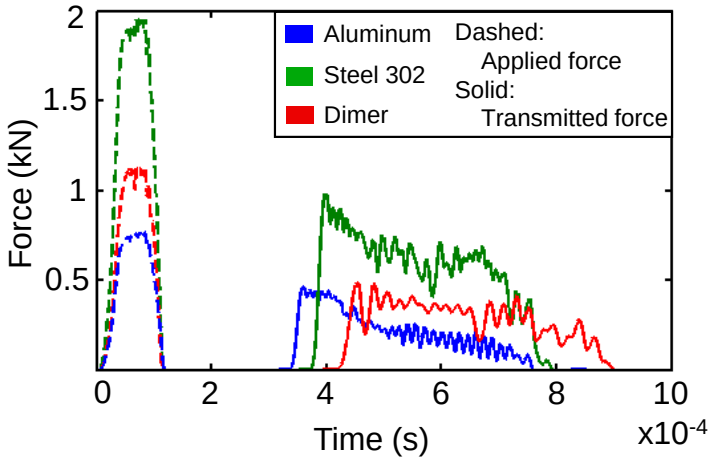

Figure 4.8: Plot of the simulated contact force between the first and second particles after the experimentally measured velocity profile is applied, and the simulated force profile of the final bead in fifty sphere chains of aluminum particles (blue), stainless steel 302 particles (green), and an alternating dimer (red).

Figure 4.8 shows the simulated force at the first contact versus simulations of the force felt by the 50th (final) sphere, after the velocity profile of the incident bar as measured by the strain gauges during the experiment was applied to the first sphere. While the incident velocity profile was nearly identical between experiments, the applied force was material dependent and varied between experiments due to the differences in stiffness of the contacts between particles and masses of the particles. The maximum force after traveling through chains of 50 spheres was reduced by 49.6% in the stainless steel 302, 39.7% in the aluminum, and 57.0% in the alternating dimer chain. The forces on the final bead in the dimer chains, as shown by the red curve in Figure 4.8, are spread over a longer time period and have a smaller transmitted maximum force. In many impact protection applications, the ratio of the input force to the maximum transmitted force is the most crucial measure of protection.

4.2 Properties of Waves in 1D Elastic-Plastic Chains

4.2.1 Contact Model Descriptions

Having verified that DEM captures the dynamics of 1D chains of elastic-plastic granular materials, we performed rigorous numerical investigations of the properties of waves traveling through these materials. In order to elucidate which aspects of the contact law control the various properties of these waves, we compared the elastic-plastic contact law to other model contacts laws which eliminated some of the features of the contact law. We performed additional simulations using a purely elastic (Hertzian) contact law, eliminating the linear plastic regime, and performed simulations on a purely linear contact law, eliminating the non-linear initial regime. A schematic of the elastic-plastic contact law is shown again in Figure 4.9.

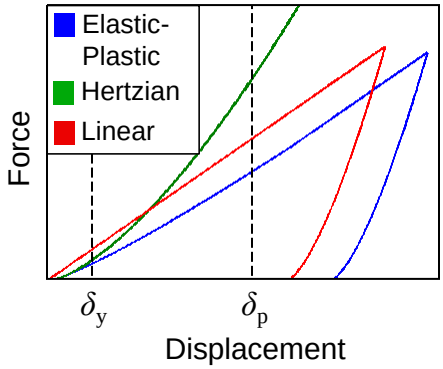

Figure 4.9: Schematics of the three force-displacement relations used in the numerical simulations: elastic-plastic (blue), Hertzian, elastic (green), and linear (red). Dotted vertical lines show transitions between regions in the elastic-plastic model with δ_y representing the displacement at which plasticity initiates and δ_p representing the displacement at which the linear regime begins.

Without plasticity, the contact between metallic spheres is captured by the Hertzian contact law, given again as:

$$F_H(\delta) = (4/3)E^*\delta^{3/2} = K_H\delta^{3/2}, \tag{4.1}$$

with the effective Young's Modulus:

$$E^* = \left(\frac{1-\nu_1^2}{E_1} + \frac{1-\nu_2^2}{E_2}\right)^{-1},$$

where E_1, E_2, ν_1, ν_2 are the Young's Moduli and the Poisson's Ratio of the two materials and the effective radius $r^* = R/2$ for identical spheres with radius R.

[3, 19, 79]. We define K_H as the Hertzian stiffness. The Hertzian contact law is equivalent to the initial region of the elastic-plastic contact before plasticity initiates. The Hertzian contact law is shown in Figure 4.9 as the green curve.

In order to isolate the contribution of the nonlinear region in the elastic-plastic contact law to the dynamics of the chain, we compared the full elastic-plastic contact model with a contact model that includes only the linear contribution of the plastic region:

$$F_L(\delta) = c_1\sigma_Y(2r^*\delta) = K_L\delta, \tag{4.2}$$

where we define K_L as the linear stiffness. The stiffness of this linear model is the same as the elastic-plastic model given in Equation (1) when $\delta > \delta_P$. For the linear contact-law, the same formulation for unloading was used as in the elastic-plastic model. The linear contact-law is shown in Figure 4.9 as the red curve.

4.2.2 Properties of Waves

Prior studies of wave propagation in elastic-plastic 1D chains of spheres focused on the energy dissipation of short impulses and on the effects of impact amplitude and duration on the wave speed [45–47]. However, the experiments reported in these studies are limited to testing short chains, and can only characterize the transmitted waves after the impact. In this work, we study long chains of particles, and focus on the understanding of the dynamics of wave propagation while plasticity is occurring at the contacts, the most relevant regime for energy dissipations during an impact. Our approach also allows a more direct comparison of the experiments with numerical simulations.

To understand the effect of plasticity and nonlinearity on the wave propagation, we performed simulations of the dynamics of 1D chains of 50 particles with elastic-plastic, Hertzian and linear models describing their contacts (Figure 4.10). In these simulations, we applied a 20 m/s step change in initial velocity to the first particle in the chain, and observed the wave front as it propagated through the materials. The dynamic response of both Hertzian and harmonic linear chains to such initial conditions are well known. Hertzian chains support the formation and propagation of a steady front that, after some initial transient effects, propagates through the chains without changing shape due to dispersion [19, 31]. The evolution of the wave front shape is shown in Figure 4.10a for a Hertzian material. In this figure, the different curves represent the velocities of all particles, superimposed and translated based on the arrival time of the wave. The arrival time of the wave front at each

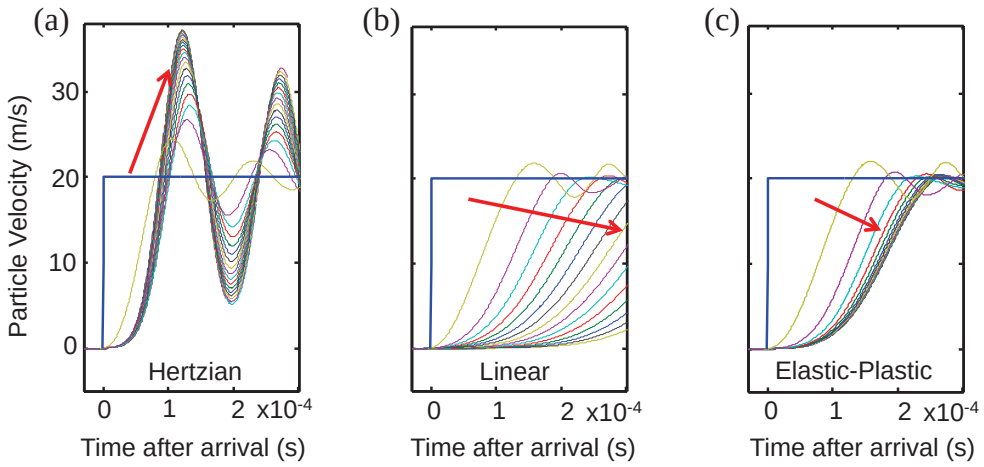

Figure 4.10: Numerical simulations comparing the dynamic response of chains of 50 particles, subjected to a 20 m/s constant velocity, governed by different contact dynamics. The different color curves represent all particle velocities after the arrival of the initial wave front. The velocities curves were translated based on the arrival time of the wave on each particle. (a) Response of a Hertzian chain; (b) response of a harmonic chain of linear springs; (c) response of a chain of elastic-plastic particles. Red arrows indicate the movement of the velocity wave front at progressively later positions in the chain. The arrow points towards the steady wave front that is formed in (a) and (c) in the Hertzian and elastic-plastic cases, respectively, while in the linear case the wave front continues to spread in the direction of the arrow due to dispersion.

particle was defined as the time at which the particle reached 1% of the applied initial velocity (0.2 m/s). Although the speed of nonlinear waves in Hertzian chains is frequency independent, it is amplitude dependent. The leading wave speed, V_H, is given by [21]:

$$V_H = 0.68 \left(\frac{E^*}{r^* \rho^{3/2}} \right)^{1/3} F_M^{1/6}, \tag{4.3}$$

where ρ is the density of the constituent material and F_M is the maximum contact force. The velocity can also be rewritten to show the dependence of the wave speed on the Hertzian stiffness as defined in Equation 4.1 as [21]:

$$V_H = 0.87 \frac{K_H^{1/3}}{\sqrt{r^* \rho}} F_M^{1/6}. \tag{4.4}$$

In harmonic lattices with linear force-displacement relations, the dispersion relation describes the speeds at which the various frequency components of the

initial disturbance move through the chain [84–86]. Because the different frequency components move at different velocities, a steady front is not formed in linear materials and the pulse widens as it travels down the chain. The evolution of the wave front shape for a chain of masses with linear contact interactions is shown in Figure 4.10b. Again in this figure the particle velocities of each particle were superimposed and translated based on the arrival time of the wave as defined previously. The frequency content separates due to dispersion and the peak of the wave appears to arrive at progressively later times after the initial arrival as the wave spreads. While the speeds of linear waves are dependent on the frequency content, there is no direct dependence on the amplitude of the initial excitation because the stiffness of the contact is constant for all amplitudes. The phase velocity of frequency component is $V_L = \omega/k$, where ω and k are the frequency and wave number, respectively, of the normal modes of the linear lattice. ω and k are related by the dispersion relation [84]:

$$\omega(k) = 2\sqrt{\frac{K_L}{M}}\,|\sin kR| = \sqrt{\frac{3K_L}{\pi R^3 \rho_{\text{avg}}}}\,|\sin kR|\,, \tag{4.5}$$

where M is the average mass of the particles, R is the average radius of the spheres, and ρ_{avg} is the average density of the constituent materials. The maximum phase velocity for any frequency component, $V_{L,\max}$, occurs for long wave length excitations in the limit as k goes to 0 and is given by:

$$V_{L,\max} = \sqrt{\frac{3K_L}{\pi R \rho_{\text{avg}}}}. \tag{4.6}$$

In elastic-plastic chains the dynamics are different. When the initial impact is large enough to induce plasticity at the contacts, the particle's loading begins in the nonlinear region described by the Hertzian contact, while the maximum force occurs in the linear regime. The shape of the wave front after a velocity pulse in the elastic-plastic case exhibits unique features compared to waves in the other two types of materials. The evolution of the wave front shape is shown in Figure 4.10c. After an initial transient region (~5 particles long), in which dispersion seems to occur, a steady wave front forms and continues to propagate unperturbed.

Plasticity has a major effect on the wave's propagation in 1D granular systems. Defining a realistic elastic-plastic contact model is essential to capture the correct dynamic behavior of such systems. Both the nonlinear and linear regimes play essential roles in the unique dynamics of these granular systems. The initial contact

nonlinearity, before the onset of plasticity, plays an important role in determining the chain's dispersion behavior, and controlling the frequency and amplitude dependence of the leading wave velocities, while the linear regime determines the apparent stiffness of the chain during plastic deformation.

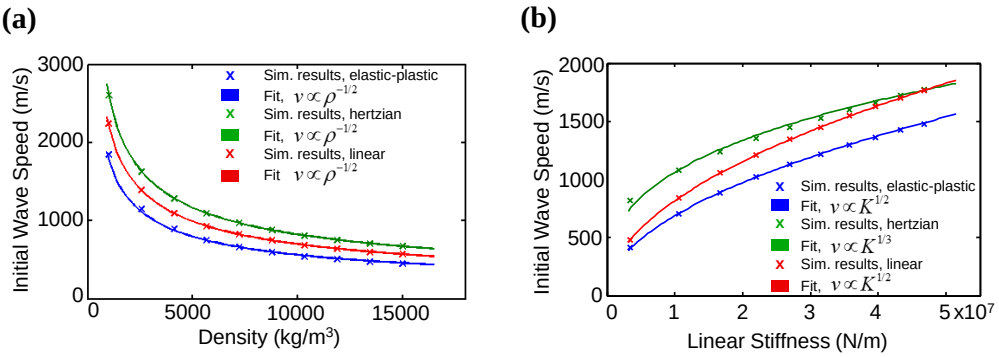

Figure 4.11: Numerical results of parametric studies of the propagating wave speed as a function of (a) the density and (b) stiffness of the particles material. The plots compare the results obtained for chains with elastic-plastic contacts (blue curves), hertzian contacts (green curves), and linear contacts (red curves), subjected to a $2F_p$ impulse. (a) Markers represent the average wave speed observed in each DEM simulation with solid lines showing the wave speed dependence on the square root of the inverse of density. (b) Markers represent the average wave speed observed in each DEM simulation with solid lines showing the wave speed dependence on either the square root or the cube root of the stiffness.

We performed parametric studies using DEM to determine how, in elastic-plastic chains, the leading wave speed depends on the material properties of the constituent particles. We compared the results with similar ones obtained for Hertzian and linear chains. First, the density of the constituent particles was varied while the Young's modulus and yield stress of the material were kept constant. We excited the 50-particle chains with an impulse of 100×10^{-6} seconds with constant force amplitude of twice the force required to reach the linear plastic regime in the elastic-plastic contact law ($2F_P$). In all simulations, the chains consisted of particles with a Young's modulus of 100 GPa and a yield stress of 500 MPa, while the density was varied in ten steps from 1000 kg/m3 to 15,000 kg/m^3. For each chain, local wave velocities of each particle were calculated and then averaged over all particles between the 10th and the 40th particle. The results are shown in Figure 4.11a. Fitting curves (solid lines in Figure 4.11a) show that all three contact models share an inverse square root dependence on the density of the constituent material.

Next, we performed parametric studies using DEM to obtain the leading wave velocity's dependence on the stiffness of the contact. The yield stress of the constituent particles was varied while the Young's modulus and density of the material were kept constant. As before, an impulse of 100×10^{-6} seconds with amplitude of $2F_P$ was applied to 50-particle chains of each material for all three contact laws. A Young's modulus of 100 GPa and a density of 5000 kg/m^3 was used for all simulations, while the yield stress was varied in ten steps from 100 MPa to 2500 MPa. For each material, local wave velocities of each particle were calculated and then averaged over all particles between the 10th to the 40th particles. The results are shown in Figure 4.11b. Fitting curves (solid lines in Figure 4.11b) show that the Hertzian material has a cube root dependence on the stiffness as predicted in Equation 4.4, while both the linear and elastic-plastic materials exhibit the square root dependence predicted in Equation 4.6. Therefore, we see that the leading wave speed of elastic-plastic chains scales in the same fashion as the simplified linear-chains.

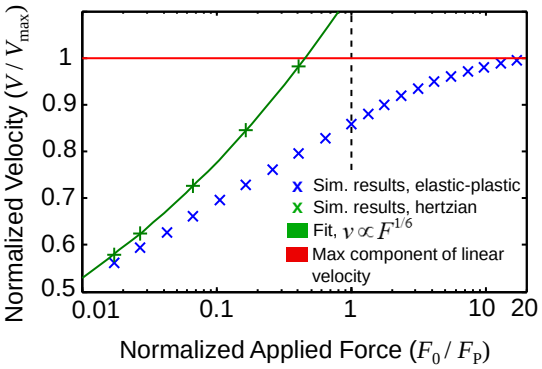

Figure 4.12: Numerical results showing the dependence of the normalized wave velocity on the normalized applied force, plotted on a logarithmic scale. Markers represent the average wave speed observed in each DEM simulation. The green curve shows the dependence of the wave speed in the hertzian material on $F^{1/6}$. The red line is the maximum velocity component of a harmonic chain given by Equation 4.6. The black, vertical, dashed line shows F_p, the force at which the linear regime begins in the elastic-plastic material and the local wave speed begins to asymptotically approach the bound, as the amplitude increases.

In the plastic region the stiffness of the contact is not amplitude dependent; however, in elastic-plastic chains the wave speed is amplitude dependent. This is due to the fact that before reaching the plastic zone, the contact force rises through the Hertzian region, which is amplitude dependent. To investigate the effect of the

excitation amplitude on the wave speed in elastic-plastic chains in comparison with Hertzian and linear chains, we calculated the response of the different contact laws after the application of impulses with greatly varying amplitude. Impulses with duration 100×10^{-6} seconds and amplitudes ranging from 10 N to 10 kN were simulated on chains of 50 particles. The particles' material properties were kept constant with a Young's modulus of 100 GPa, yield stress 500 MPa, and density 5000 kg/m^3 (F_P = 584N). The simulated leading wave speeds are shown versus the logarithm of the applied force, normalized by F_p, as the blue and green markers in Figure 4.12 for elastic-plastic and Hertzian granular chains, respectively. The green curve in Figure 4.12 shows the dependence of the wave speed in the Hertzian material on $F^{1/6}$ as predicted in Equation 4.4. The red line in Figure 4.12 shows predictions for the maximum velocity component of the harmonic linear material given in Equation 4.6. As the force increases, the elastic and elastic-plastic wave speeds diverge. Once the amplitude of the force reaches F_p, the leading wave speed of the elastic-plastic material begins to asymptotically approach the prediction of the fastest component of a harmonic lattice with the same stiffness as the elastic-plastic linear regime. Therefore, Equation 4.6 represents a bound of the leading wave speed in the elastic-plastic 1D material, although the required force to reach this bound is highly material dependent. Figure 4.12 shows that for large amplitude impacts (inducing forces greater than the force required to reach the plastic regime, F_p) the leading wave velocity changes by only 10% over an order of magnitude change in the force. For impacts in which the plastic regime is reached, 1D elastic-plastic chains exhibit unique dynamics where the leading wave velocity has no frequency dependence, relatively little amplitude dependence, and is almost solely a function of the material properties of the constituent particle. Combining the velocity bound in Equation 4.6 with the elastic-plastic contact law presented in Chapter 3 it is possible to derive a model to predict the maximum wave speed ($V_{\max}$) in 1D granular materials when plastic deformation is occurring. $V_{\max}$ can be expressed in terms of the material properties of the constituent particles for high amplitude impulses as:

$$\begin{aligned} V_{\max} &= \sqrt{\frac{3K_L}{\pi R \rho_{\text{avg}}}} \\ K_L &= 2\pi r^* \sigma_y \left[-6.76 \left(\frac{E^*}{\sigma_y} \right)^{-0.14} + 6.30 \right]. \end{aligned} \tag{4.7}$$

In order to gain further insights into the details of the dynamics observed in the simulations and experiments of these materials, particularly the dimer materials,

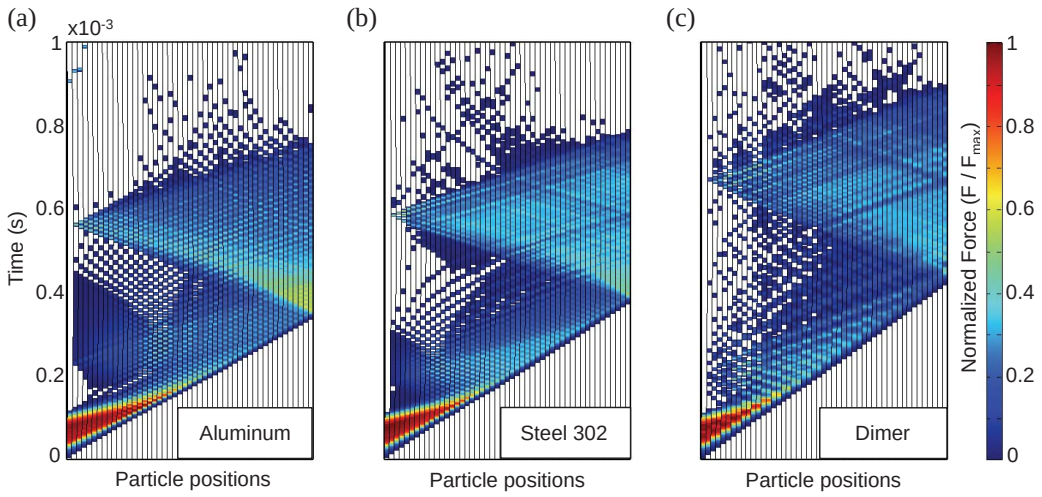

Figure 4.13: X-T diagrams showing the wave propagation in time through chains of fifty particles, assembled with particles of different materials. All chains were excited by a pulse of amplitude $2F_P$ and 100×10^{-6} sec duration. The color scale represents the contact forces between particles, normalized by the applied force. (a) Chain of aluminum particles. (b) Chain of stainless steel 302 particles. (c) Dimer chain consisting of alternating stainless steel 302 and aluminum.

we simulated a 100×10^{-6} second impulse of amplitude $2F_p$ on 50-particle chains of steel 302, aluminum, and an alternating dimer chain. X-T diagrams showing particle position over time are shown in Figure 4.13, with colors scale depicting the magnitude of the contact force between each particle, normalized by the applied force. For each material we observe the initial pulse traveling at a nearly constant speed determined by the stiffness in the linear regime for that material. Once the initial force is removed after 100×10^{-6} seconds, the unloading wave travels through the chain at a faster speed, governed by the elastic unloading of the particles, followed by subsequent reloading waves as the particles continue to collide within the chain.

The dynamics of the non-uniform chain (Figure 4.13c) are visibly different than the behavior of the single material chains. Heterogeneous chains of Hertzian materials have been shown to have wave speed dependence on the mass ratio of the constituent spheres, whereas wave speeds in the harmonic linear chains only depend on the average density of the constituents [30–32, 84–86]. For chains of spheres with identical radii but two alternating materials, the leading wave velocity in the dimer elastic-plastic materials shown in Figure 4.13c does not show any dependence on the mass ratio, only the average of the densities of the two materials (also shown experimentally [44]). After the arrival of initial plastic wave, trailing waves operate

within the elastic regime, and internal reflections associated with local resonances are visible in the XT diagram of the dimer chain (Figure 4.13c), behind the leading plastic wave. These elastic internal reflections depend on the particles mass ratio and slow the transfer of energy to the leading plastic front [30–32]. Therefore, the two types of waves in these materials exhibit inherently different behaviors: the leading wave which causes plasticity does not excite local resonances and its speed depends only on the average mass, while the trailing elastic waves do excite local resonances and cause internal reflections. In dimer chains, this results in more collisions, sustained for longer times, after the initial impact has passed. The forces transmitted at the end of the chain are spread over a longer time period and more uniformly (confirming the experimental velocity measurements in Figure 4.7 and simulation of transmitted force in Figure 4.8). Other periodic composite materials for impact applications have also demonstrated wave propagation properties that exceed those of either constituent component. For example, the shock speed through layered polycarbonate/stainless steel 304 and polycarbonate/aluminum was also shown to be significantly slower than shocks in the constituent materials also due to internal reflections [87].

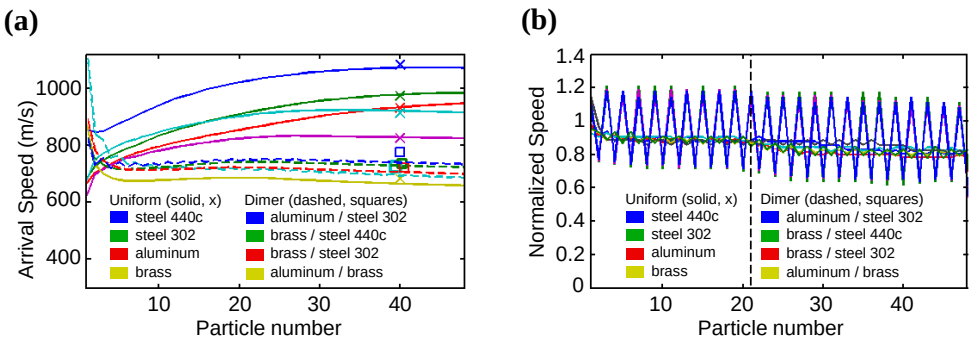

Figure 4.14: (a) Arrival speed of the wave front as it travel through chains of fifty particles of various materials. Numerical results (lines) are compared with experiments (markers) for the particle's velocity measured by the laser vibrometer in the 40th particle. Solid lines represent the arrival speeds in uniform chains. Dashed lines show the same results for dimer chains. (b) Numerical results showing the local wave speed as it travel through the fifty particle chains, normalized by the wave speed bound given in Equation 4.7.

All of the Hopkinson bar experiments with uniform and dimer chains are compared with DEM simulations in Figure 4.14. The markers in Figure 4.14a show the arrival speed measured experimentally on the 40th sphere in all 50 particle chain

experiments. The arrival speed is defined for each sphere as the total distance of the center of the sphere from the end of the incident bar divided by the time at which the particle velocity reaches 1% of the applied velocity (typically 0.12 m/s for these experiments). The arrival speed of the wave to a point in the chain is therefore the average of the local wave speed between each particle before that point. This measure was used instead of the local wave speed used in Figures 4.11 and 4.12 because the laser vibrometer measured the cumulative arrival time to the 40th sphere and not the subsequent arrival time between adjacent spheres. We compared the experimentally measured arrival speeds at the 40th particles to the predicted arrival speeds throughout the chain for each of the experiments. Solid lines in Figure 4.14a represent uniform materials while dashed lines represent the different dimer combinations. The simulations capture the leading wave speed and particle velocity amplitude for a wide range of different types of metallic spheres and for dimer chains of alternating material. For the uniform chains, the average error between the measured and simulated arrival velocities was 1.15%, likely due to variability in the material properties of the spheres. For the dimer chains, simulated arrival times were all consistently underestimated by an average of 3.13%. This suggests that the contact between dissimilar materials is slightly stiffer than predicted, and this is most likely a consequence of the assumption in the model that stiffness in the linear regime is solely a function of the softer material's properties.

Figure 4.14b shows the leading wave velocities after a $2F_P$ impulse was applied to each of the material combinations shown in Figure 4.14a. The leading wave velocities are normalized as: $V_{\text{norm}} = V/V_{\text{max}}$ where V_{max} is given by Equation 4.7. The vertical dashed line represents the approximate location at which the contact forces drop below F_P and stiffness becomes amplitude dependent once again. Before this line, when the contact forces are all in the plastic linear regime, the normalization causes all curves to overlap and we observe nearly no amplitude change. All curves converge to around 90% of the maximum possible wave speed because of the amplitude dependence demonstrated in Figure 4.12. The alternating dimer combinations show significant variations in the arrival times between heavy versus soft constituents, but the average still falls on the normalized curve. As stated earlier for chains of particles of equal radius with alternating material properties, there is no dependence of the leading wave velocity on the mass ratio of the particles that comprise the dimer, only on their average density. Once the contact forces drop below the purely linear regime, the leading wave speed becomes more amplitude dependent, as seen in Figure 4.12, and the curves diverge slightly and begin to slow

as energy continues to be dissipated in the intermediate regime between the Hertzian and plastic zones in the elastic-plastic contact law.

4.3 Designing 1D Wave Properties by Choosing Material Properties

We have shown that the leading plastic wave in elastic-plastic granular chains forms a steady propagating wave front, with a speed that is dependent on amplitude, but is independent of frequency content of the excitation and is bounded by the long-wavelength speed of a simplified linear model with the same stiffness. We have also shown that our model predicts correctly the leading wave properties for both uniform and dimer chains. These foundations provides the necessary insight to predict the behavior of new uniform materials, new combinations of dimer materials, and new rationally designed particles to obtain materials with unique wave propagation properties. Figure 4.15 shows a design surface, which relates the linear stiffness and the average density of constituent particles with the predicted bound of the leading wave speed given by Equation 4.7. We can use this surface to design 1D materials for which the speed of plastic stress waves cannot exceed the predicted value. The real materials used in experiments, as well as others, like tungsten carbide, are shown by markers with blue stems. Brass has the lowest predicted wave speed with 833 m/s, while stainless steel 440c has the highest with 1347 m/s, a factor of 1.6 larger. Alternating dimers using the same materials are shown by markers with red stems. Chain consisting of a combination of aluminum and tungsten carbide particles have the lowest predicted wave speed, with 629 m/s, a factor of 2.14 lower than the uniform stainless steel 440c wave speed. By using alternating dimers, the design space of wave speeds has been expanded.

Additionally, the surface plot in Figure 4.15 allows predicting the behavior of engineered particles. For example, we see that materials with the highest density and lowest stiffness lead to the slowest leading wave velocity. If we were to coat a tungsten carbide particle with aluminum, such that the final particle had the stiffness of aluminum but a density five times higher, Equation 4.7 predicts that we would obtain a wave speed of 489 m/s. If we were to create a hollow particle of tungsten carbide such that the stiffness properties were not changed, but the final particle density was five times less, Equation 4.7 predicts that we would obtain a wave speed of 3011 m/s. These two engineered materials are shown by the markers with black stems in Figure 4.15. Such particles increase the design space such that we obtain a factor of 6.2 between the fastest and slowest materials. However, these hollow/coated particle chains would have to be used within a range of impacts that

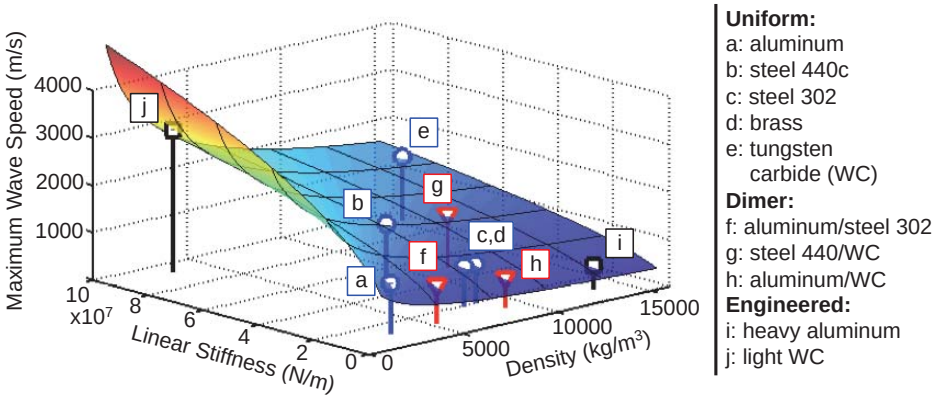

Figure 4.15: Surface plot relating the maximum wave front speed as a function of the linear stiffness of the contact and the average density of the constituent particles, calculated using Equation 4.7. Markers and stems show locations of uniform chains of various types of particles (blue), alternating dimers of those materials (red), and engineered particles such as heavy core aluminum and hollow tungsten carbide (black).

do not violate certain assumptions: first that the plastic region is small enough that it is not altered by the presence of another material in the core of the particle, and second that the wave speed is much slower than the time it takes for the stresses to travel from one end of the particle to the other. These assumptions are unlikely to be valid for very large amplitude impacts, but the design surface allows us to easily visualize how new combinations of materials or engineered particles are likely to dynamically behave.

4.4 Summary of Chapter

We investigated the dynamics of high-amplitude stress waves propagating through 1D chains of spherical particles. In order to understand the effect of each regime of the piece-wise nonlinear, elastic-plastic contact law, we compared chains of elastic-plastic spheres, with chains of purely elastic particles interacting via the Hertzian contact law, as well as with harmonic chains having the same linear stiffness as the one found in the linear regime of the elastic-plastic model. We reported that the elastic-plastic chains showed no dispersion even when forces reached the fully plastic linear regime. As in a chain of Hertzian particles, the frequency components of the wave all propagated at the same velocity, unlike in a typical linear material. However, by varying the density and contact stiffness of the constituent particles,

we found that while plasticity is occurring at the contacts, the speed of the leading wave in the elastic-plastic chain scales with the material properties in the same manner as wave velocities in a harmonic chain of particles with linear contacts. We showed that the harmonic prediction of velocity of the frequency component with highest speed represented an amplitude-dependent bound on the maximum possible velocity in the elastic-plastic chain.

For high amplitude, long duration impacts, for which plastic dissipation continues as the wave propagates, the leading wave travels without dispersion at nearly constant amplitude predicted by the upper bound. This upper bound depends solely on the material properties of the constituent particles. We use these findings to predict the wave propagation properties of chains of uniform materials, new combinations of materials, and chains of engineered particles. We support our finding with experimental tests performed in a Hopkinson bar setup equipped with a laser vibrometer.

Chapter 5

HIGHER DIMENSIONAL GRANULAR CRYSTALS

In this chapter, we study the dynamics of elastic-plastic granular arrangements of spherical particles in higher dimensions, more suitably called granular crystals. While 1D materials are useful as models and simplified cases, most of the applications for granular crystals, particularly impact protection applications, require 2D and 3D materials. The addition of more dimensions also increases the ability to introduce more heterogeneity. In higher dimensional materials, impact energy can be directed away from the sensitive areas of the material whereas in 1D, energy can only be dissipated or reflected. Here we investigate the behavior of impact waves propagating through 2D and 3D materials. First we provide experimental validation of our DEM simulations for higher dimensional materials. We show that DEM is a suitable approach to studying uniform and heterogeneous granular crystals in 2D and 3D despite the assumptions required neglecting interparticle friction and angular rotation. Then we show how we can extend the elastic-plastic wave speed findings in Chapter 4 to 2D and 3D granular crystals. And finally, we demonstrate the ability to use interfaces between particles of dissimilar materials to create systems of elastic-plastic granular crystals suitable for impact protection applications.

Some content of this chapter has been partially adapted from:
Hayden A. Burgoyne et al. "Guided impact mitigation in 2D and 3D granular crystals" *Procedia Engineering* 2015, **103**. p. 52-59.

5.1 Experimental Validation of Simulations of 2D and 3D Granular Crystals

In Chapter 4, we experimentally validated the DEM approach to model one-dimensional granular crystals. However, with all particles aligned along one axis, tangential forces could not play a role in the dynamics. In the DEM approach to simulating large systems of particles in 2D and 3D, a simplifying assumption is that the interactions between particles can be fully described by the normal force-displacement relationship. Friction can be ignored if either the tangential motion of the particles is negligible or if the magnitude of frictional forces is negligible compared to other forces on the particles. If friction were to play a significant role, it would contribute to additional stiffness by preventing particles from sliding past

one another. Rotational motion of the spheres is also neglected. Angular motion can only be ignored if the energy lost to rotating the spheres is negligible compared to the energy lost due to plastic dissipation, and if each pair of particles always contacts at the same point during the impact. A series of experiments were performed in order to experimentally validate the DEM approach for 2D and 3D simulations, as previous described in Chapter 2. First, a sliding impactor rig was designed and built to test 2D arrays of particles. Next, drop weight tower experiments were performed to impact a two-layer arrangement of particle as a first step toward 3D experimentation. The ultimate goal of both experiments was to investigate if our numerical approach can predict the behavior of elastic-plastic granular crystals given these assumptions and ensure that none of the neglected effects play a significant role in the dynamics. The 2D and 3D experiments performed on uniform granular crystals of a single type of particle provided the validation required for the numerical analysis shown subsequently in Section 5.2, where we show how our understanding of elastic-plastic wave propagation in 1D from Chapter 4 can be extended to 2D and 3D granular crystals. Then, the 2D and 3D experiments performed on heterogeneous granular crystals with particles of different types provided the validation required for the numerical analyses and discussions of applications for impact protection in Section 5.3.

5.1.1 Impacts on 2D Arrays of Particles Using Sliding Rig

Previous experiments on 2D granular crystals have been used to validate DEM simulations for very low amplitude impacts in which every contact point remained elastic and no energy was dissipated within the crystal [25, 50, 51, 53]. Using the sliding 2D impacting rig described previously in Chapter 2, impacts on 2D granular crystals were performed at significantly higher impact energies for which plastic deformation occurred at the contact between every layer throughout the crystal. In order to validate the 2D DEM simulations, we compared the arrival time of the wave through subsequent layers for the experimental and numerical data. Arrival time for both the experiments and the simulations was defined as the time at which the particle moved 3/4 of a full pixel's width (approximately 191 μm) from its original location. By using nearly one pixel's width as the threshold distance for arrival time of the wave, the effect of noise and changes in the lighting as the particles displace is reduced in experimental images. The same threshold distance is used to calculate arrival time for simulations for the sake of comparison although the arrival of wave can be more accurately resolved in simulations.

Uniform Granular Crystals of a Single Material

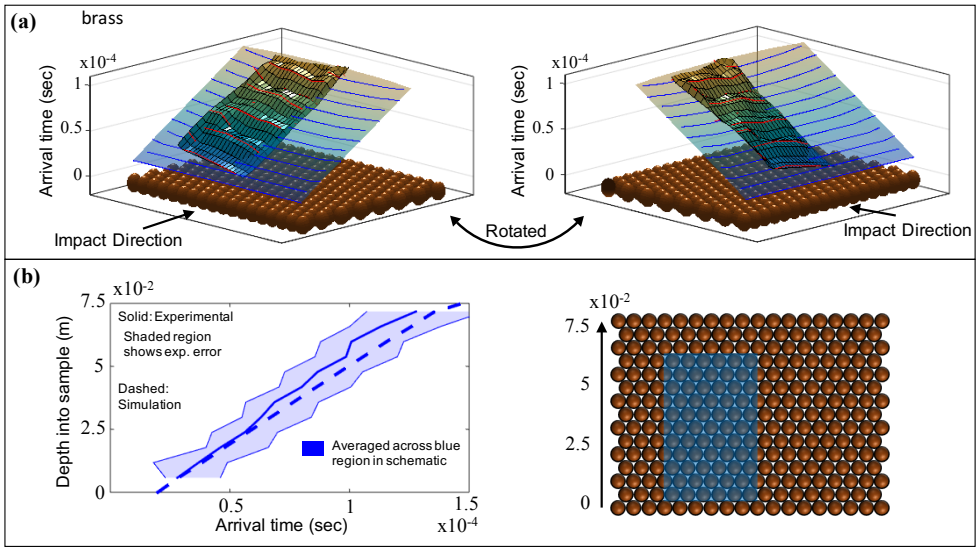

Figure 5.1: (a) Surfaces of arrival time, experimental (solid, red contours) and simulated (transparent, blue contours), of the impact wave through a uniform array of brass spheres, shown from two angles. Arrival time for both the experiments and the simulations was defined as the time at which the particle moved 3/4 of a full pixel's width. (b) Plots of impact wave depth from the front of the sample versus arrival time of the wave averaged horizontally across the blue strip shown in the schematic to the right of the plot. Dashed line shows simulation while the solid line shows the experimental results. Shaded regions on the plots represent arrival times if we assume the largest magnitude errors for the experimental displacement measurements (+/- half a pixel's width).

Figure 5.1a shows surfaces of the arrival time of the impact waves through a 2D array of uniform brass spheres for the experimental data and the simulation using the experimentally measured initial impactor bar velocity. These surfaces are analogous two-dimensional XT-diagrams. We see qualitative agreement between the numerical and experimental results. Experimental error due to the limited resolution of the high-speed camera at such high frame rates is seen in Figure 5.1a as the random bumps on the experimental surface. Error due to slight misalignments of impactor bar are seen in Figure 5.1a as tilt in the horizontal direction. To alleviate some experimental error and make a more quantitative comparison between experiment and simulation data, arrival times were averaged horizontally across particles within the same layer of the array. By plotting the arrival time along vertical strips of the array through the depth of the sample, as shown in the schematic on the right of

Figures 5.1b, we can compare experimentally measured and simulated arrival times for the uniform arrays and for different regions of the heterogeneous 2D arrays. The plots on the left of Figure 5.1b show the arrival time of the wave through vertical strips of the arrays, averaged horizontally across a 6-particle wide strip, versus depth from the front of the array. Shaded regions on the plots bound the arrival times if we assume the largest possible magnitude of experimental errors for the displacement measurements, plus or minus one-half of a pixel width. The slope of the curves in Figure 5.1b represent the local impact wave speed at that depth in the array. For the uniform array of brass particles, we see that the simulated arrival times and wave speed matches the experimentally measured data within the bounds of the experimental error quantification.

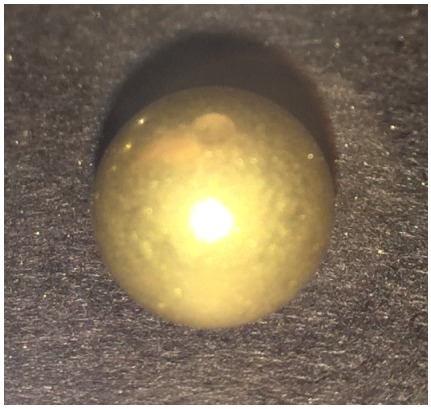

Figure 5.2: Photograph of a brass sphere after impact in a 2D sliding rig experiment. Permanent plastic deformation is visible on the top surface of the sphere. Damage is uniform, symmetric and shows no sliding or transverse movement during compression.

Figure 5.2 shows a photograph of a brass sphere from the 12th row of a sliding impact rig experiment. There is an approximately 1 mm permanently deformed area visible, as well as similar deformed areas at the other contact points. These areas of deformation are all uniform, symmetric suggesting no transverse motion during the impact.

Figure 5.3a shows surfaces of arrival time for a uniform array of stainless steel 304 particles. The higher reflectivity of the steel spheres leads to more uncertainty in the particle tracking due to experimental lighting conditions. However, Figure 5.3a still shows qualitative agreement between the simulated arrival surface and the experimentally measured displacements from the sliding impactor rig. Furthermore, 5.3b again shows plots of arrival time versus depth averaged horizontally across

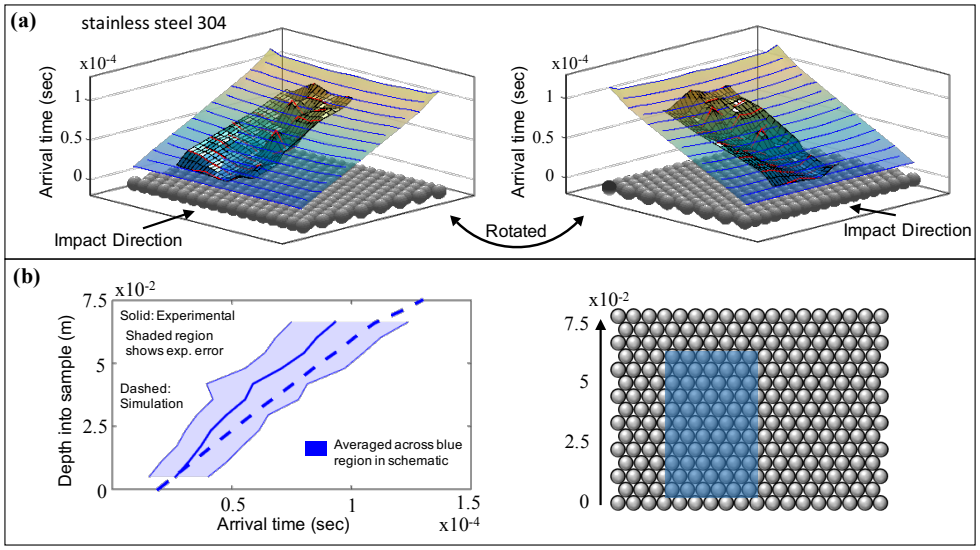

Figure 5.3: (a) Surfaces of arrival time, experimental (solid, red contours) and simulated (transparent, blue contours), of the impact wave through a uniform array of brass spheres, shown from two angles. Arrival time for both the experiments and the simulations was defined as the time at which the particle moved 3/4 of a full pixel's width. (b) Plots of impact wave depth from the front of the sample versus arrival time of the wave averaged horizontally across the blue strip shown in the schematic to the right of the plot. Dashed line shows simulation while the solid line shows the experimental results. Shaded regions on the plots represent arrival times if we assume the largest magnitude errors for the experimental displacement measurements (+/- half a pixel's width).

each layer for the stainless steel 304 array in order to alleviate some experimental error. Again, we see good agreement in the arrival times and wave speeds for the simulations versus the experiments.

Using the 2D sliding impactor rig, we showed that our DEM approach to modeling 2D granular crystals captured the behavior of impact waves causing plastic deformation at the contacts despite assumptions neglecting tangential forces and rotational motion of the particles. By measuring the displacement of each particle in the field of view of the camera, we showed that our predictions for the particle displacements, particle velocities, and speed of the wave front match between experiments and simulations. This result provides the validation required to perform the numerical analyses of the general properties of elastic-plastic waves in 2D granular crystals shown in Section 5.2.

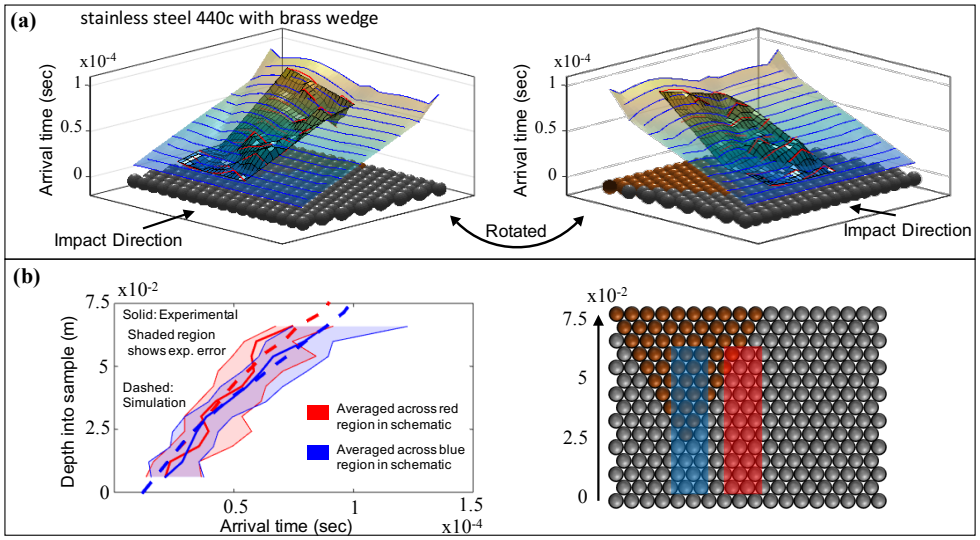

Figure 5.4: (a) Surfaces of arrival time, experimental (solid, red contours) and simulated (transparent, blue contours), of the impact wave through an array of stainless steel 440c particles with a wedge of brass particles at a 60° interface. (b) Plots of impact wave depth from the front of the sample versus arrival time of the wave averaged horizontally across the red and blue strips shown in the schematic to the right of the plot. The two strips correspond to one region which mostly remains in the first material (red region) and another region which mostly transitions to the second material (blue region). Dashed lines show simulation while the solid lines show the experimental results. Shaded regions on the plots represent arrival times if we assume the largest magnitude errors for the experimental displacement measurements (+/- half a pixel's width).

In order to experimentally validate simulations of waves traveling through heterogeneous granular crystals, particularly through oblique interfaces of heterogeneous particles, experiments were performed on samples with a wedge of a second material in the 2D array. A schematic of the experimental setup for the heterogeneous samples is depicted in Figure 5.4b. Figure 5.4a shows the surface of arrival time through a 2D array of stainless steel 440c particles with an intruding wedge of brass particles with a 60° interface. Because the wave travels more slowly through the brass particle in the wedge, the arrival times are slowed and the wave appears bent upwards. The nature and applications of this bending across heterogeneous interfaces will be more heavily investigated in Section 5.3.2; however, here were experimentally validated that the bending behavior is captured by the DEM simulations. The shape of the simulated surfaces again match qualitatively with the experimentally measured sur-

faces with surfaces of experimental arrival time showing the distribution of random errors due to limitations of the resolution of the high-speed camera. To alleviate some of the experimental error, Figure 5.4b again shows the arrival time of an impact wave averaged horizontally across layers of the sample; for heterogeneous samples, two vertical strips were used. The strips were chosen such that one contained nearly uniform stainless steel particles (red) while the other includes the interface with the brass particles part way through the strip (blue). Figure 5.4b shows plots for an impact on the array of stainless steel 440c particles with a wedge of brass particles with a 60 degree interface. Although, stainless steel particles introduce more experimental error due to their surface finish, the arrival times in the two strips in Figure 5.4b diverge as one travels through the brass with a slower wave speed, matching the numerical predictions.

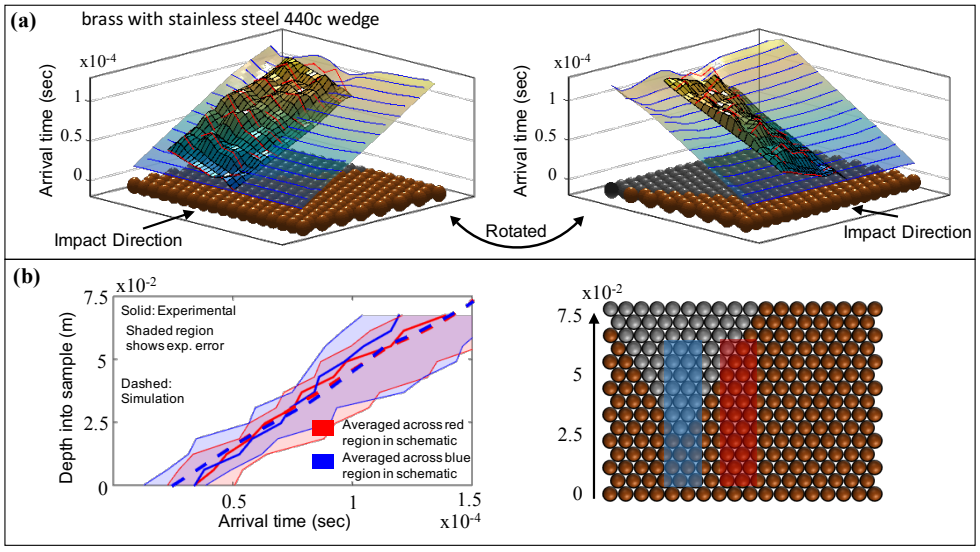

Figure 5.5: (a) Surfaces of arrival time, experimental (solid, red contours) and simulated (transparent, blue contours), of the impact wave through an array of brass particles with a wedge of stainless steel 440c particles at a 60° interface. (b) Plots of impact wave depth from the front of the sample versus arrival time of the wave averaged horizontally across the red and blue strips shown in the schematic to the right of the plot. The two strips correspond to one region which mostly remains in the first material (red region) and another region which mostly transitions to the second material (blue region). Dashed lines show simulation while the solid lines show the experimental results. Shaded regions on the plots represent arrival times if we assume the largest magnitude errors for the experimental displacement measurements (+/- half a pixel's width).

Additionally, Figure 5.5a, shows the surface of arrival time through a 2D array

of uniform brass particles with an intruding wedge of stainless steel 440c particles with a 60° interface. Figure 5.5b shows plots for an impact on an array of brass particles with a wedge of stainless steel 440c particles with a 60 degree interface. Simulations of the brass array with a stainless steel 440c wedge do not predict much change in the arrival time. Because the displacement threshold must be high enough to accommodate experimental limitations, we can't observe a lot of the nature of the initial wave behavior. However, we can see in Figure 5.5b that the experimentally measured arrival time is very accurately predicted by simulations for the chosen threshold.

These experiments further demonstrate that DEM simulations capture the behavior of impact waves propagating through 2D array of elastic-plastic spheres. For both uniform 2D granular crystals and heterogeneous granular crystals with interfaces between dissimilar materials, we were able to accurately capture the behavior of impacts causing plastic deformation. These experiments demonstrating the bending of impact waves as the transition from an area of higher wave speed to an area of lower wave speed provide validation for the analysis of Snell's law in elastic-plastic granular crystals which will be discussed in Section 5.3.

5.1.2 Impacts on 2-Layer, 3D Granular Crystals using Drop Tower

Drop weight tower experiments were performed in order to begin to investigate if our numerical approach could predict the behavior of elastic-plastic granular crystals in 3D as well and verify again that none of neglected effects played a role in the dynamics, particularly on the forces experienced by the impactor. Because of limitations of the experimental equipment, difficulty instrumenting a 3D sample, and the amount of time required to setup the 3D samples, only two layers of particles were stacked. While the transition from 1D to 2D required new assumptions regarding the interactions between particles in the tangential directions, there are no new fundamental assumptions required in transitioning from 2D to 3D. Therefore, the experimental validation of the 2D arrays using the sliding impacting rig also provides validation that the DEM approach can be extended to 3D granular crystals as well. However, with the additional dimension, there is grater variety of crystal structures in 3D, even for densely packed crystals. Therefore, we first used the drop tower experiments discussed in this section to further validate the DEM approach for uniform 3D granular crystals in order to support numerical analyses in Section 5.2. Additionally, we then performed experiments on 2-layer 3D granular crystals in a face-centered-cubic (FCC) configuration to show that our approach can be extended

to investigations of increasingly complex heterogeneous granular crystals.

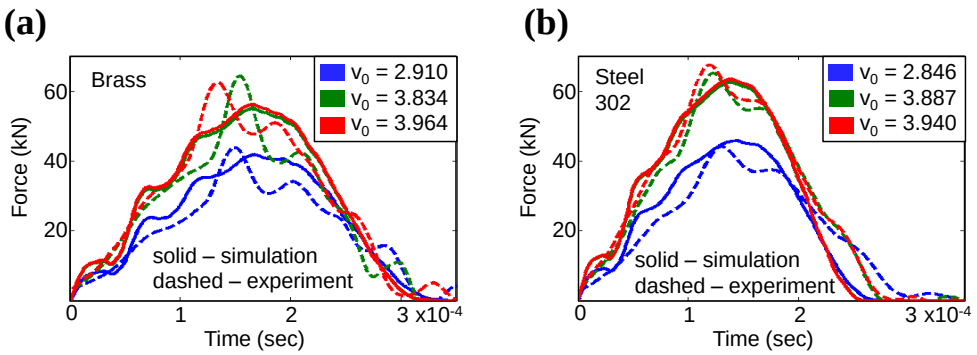

Figure 5.6: Plots of forces versus time on the impactor during impacts performed on two-layer crystals of uniform materials. The plots compare the experimental and numerical forces on the impactor as a function of time (a) Impacts on arrangement of brass particles. (b) Impacts on arrangement of stainless steel 302 particles. Different initial velocities are shown in various colors, and experimental data is shown with dashed lines while numerical predictions are shown as solid lines.

Figure 5.6 shows the comparison of experimental and numerical forces on the impactor for the two-layer HCP packing described in Chapter 2, for both uniform brass and uniform stainless steel 302 systems. Despite only describing the normal interactions, the 3D DEM simulations predict correctly the magnitude of the forces and the impact duration, describing well the overall behavior of the system (e.g., the overall system's stiffness and energy transferred). From these results, we deduce that friction, tangential forces, and angular momentum play a secondary role in the dynamics of these systems. The experimental results typically show more oscillations after the peak force than predicted by the numerical simulations, this is likely a result of the mass of vibrations in the impactor.

In addition to the uniform 2-layer HCP crystals, we performed experiments on 2-layer crystals using combinations of brass and stainless steel 302 particles. Figure 5.7 shows the experimentally measured and simulated forces in the impactor versus time for drop tower experiments on composite crystals of the two materials. The blue curves correspond to experiments in which the entire top layer was comprised of brass spheres while the entire bottom layer was composed of stainless steel 302 spheres. The green curves correspond to an arrangement of the two materials where, within both the layers, concentric hexagons are formed by alternating between the brass and stainless steel 302. This arrangement is shown in Figure 5.7a as the

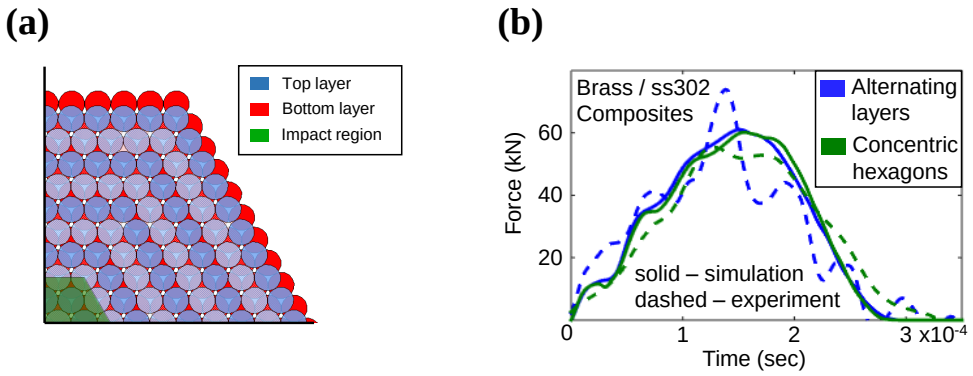

Figure 5.7: (a) Schematic diagram showing a top down view of one quarter of the experimental arrangements of the spheres as well as the arrangement of particles for simulations of the experiment. Light blue and darker blue circles represent different materials used in the composite experiment described as concentric hexagons. Shaded green area (bottom left) is the impacted region. (b) Plots of forces versus time on the impactor during impacts performed on two-layer crystals comprised of both brass and stainless steel 302. Blue curves represent an experiment where the entire top layer was brass particles and bottom layer was stainless steel 304 particles. Green curves represent the arrangement shown in (a) with alternating hexagons of the two materials within the two layers.

lighter and darker blue spheres. We see good agreement between the durations and magnitudes of the experimental and 3D DEM simulated forces on the impacting mass for composite crystals of two materials as well.

Lastly, in order to gain more insight into the effects of different contact geometries, a different crystal packing arrangement was used for drop tower experiments of uniform brass. Instead of a 2-layer HCP crystal, a 2-layer FCC crystal was used to change the number of contact points between the spheres in the top and bottom layers. In the HCP crystal, a sphere in the top layer sat in contact with three in the bottom. As shown in the schematic of the experimental and numerical arrangement of spheres in Figure 5.8, in the FCC arrangement, each sphere in the top layer is in contact with four spheres in the bottom layer. Figure 5.8b shows the experimentally measured and simulated forces on the impacting weight for this arrangement. The blue curve in Figure 5.8b can be directly compared to the green and red curves in Figure 5.6a. We see that the FCC crystal packing leads to higher forces in the impactor and a shorter duration of impact. Despite the modification in the contact geometry and arrangement of materials, 3D DEM is still able to capture the duration

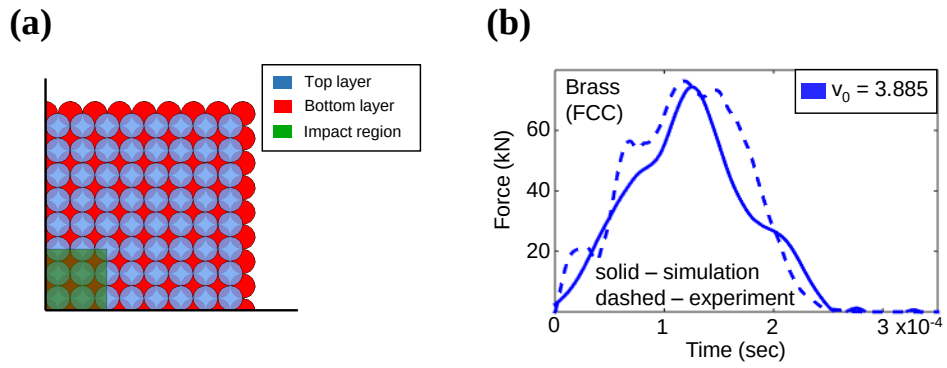

Figure 5.8: (a) Schematic diagram showing a top down view of one quarter of the FCC experimental arrangement of the spheres as well as the arrangement of particles for simulations of the experiment. Shaded green area (bottom left) is the impacted region. (b) Plots of forces versus time on the impactor during impacts performed on two-layer FCC crystals of uniform brass particles. Experimental data is shown with dashed lines while numerical predictions are shown as solid lines.

and magnitude of the forces on the impactor for all cases.

5.2 Properties of Waves in Uniform 2D and 3D Granular Crystals

With the experimentally validated 2D and 3D DEM approach, we can investigate the general properties of waves in higher dimensional elastic-plastic granular crystals like we did for 1D chains in Chapter 4. For 2D and 3D lattices of elastic particles with Hertzian contact interactions, Manjunath showed that predicted velocities of solitary waves in 1D could be scaled to 2D and 3D by taking into account packing density and the angle between contacts [60]. It was shown that:

$$\begin{aligned} V_{\mathrm{H,2D}} &= \frac{3}{2\sqrt{2}} V_{\mathrm{H,1D}} \\ V_{\mathrm{H,3D}} &= \frac{2}{\sqrt{3}} V_{\mathrm{H,1D}}, \end{aligned} \tag{5.1}$$

where $V_{\mathrm{H,1D}}$ was the solitary wave speed through 1D Hertzian granular chains.

The wave speed of elastic-plastic granular crystals was previously shown to be somewhat amplitude dependent because the initial non-linearity determines how quickly the linear regime is reached. Therefore, in our numerical investigation the applied force on each particle in the first layer was always fixed such that $2F_p$, twice the required force to reach the linear region for that material, was initially experienced at each contact between the first and second layers. By fixing the

relative initial contact force, the wave speeds' dependence on the material properties is decoupled from the amplitude dependence. For the subsequent numerical studies, simulations were performed on 50 layers of 1D, 2D, and 3D densely packed granular crystals as discussed in Chapter 2. The 2D and 3D simulations were performed with periodic boundary conditions on the sides.

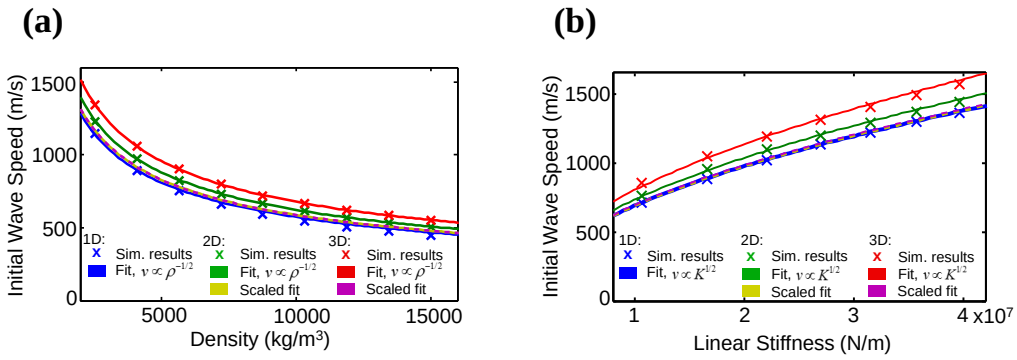

Figure 5.9: (a) DEM results of a parametric study of initial stress wave speed versus the density of the material used in 1D, 2D, and 3D close-packed arrangements of particles. Markers represent the wave speed observed in DEM simulations with solid lines showing the wave speed dependence on the square root of the inverse of density. Dashed lines (yellow and purple) show this fit scaled by the factor determined by the geometry and are nearly indistinguishable and overlap with 1D results (blue). (b) DEM results of a parametric study of initial stress wave speed versus the stiffness of the material used in 1D, 2D, and 3D close-packed arrangements of particles. Markers represent the wave speed observed in DEM simulations with solid lines showing the wave speed dependence on the square root of the stiffness. Dashed lines show this fit scaled by the factor determined by the geometry.

A parametric study was done by varying the density of the constituent material and the yield stress of a model material independently. In order to determine the dependence of the wave speed on the density of the particle material, simulations of impacts on 1D, 2D, and 3D systems were performed with 10 densities between 2000 kg/m^3 and 16000 kg/m^3. For these simulations, the Young's modulus and yield stress were fixed at 100 GPa and 500 MPa, respectively. The simulated speed of the stress wave traveling though the material was averaged over 20 layers for each density and each geometry and shown as markers in Figure 5.9a. By fitting curves to the numerical data we see that the wave speed of 2D and 3D elastic-plastic granular crystals continues to be inversely proportional to the square root of the density of the particle material. Furthermore, if we scale the fitting curves using the same c constants as Equation 5.1 based on the changes in stiffness and packing densities in

the manner demonstrated by Manjunath in the elastic case [60], all the fits collapse to a single curve. Therefore, despite the additional piece-wise non-linearities in the elastic-plastic case, the density dependence exhibited by 1D granular chains can still be scaled to 2D and 3D granular crystals.

Next, in order to determine the dependence of the wave speed on the stiffness of the contact between particles, simulations of impacts on 1D, 2D, and 3D systems were performed with 10 yield stresses between 100 MPa and 2500 MPa. In the linear region of the elastic-plastic model, the stiffness of the contact, K_{1D}, is a function of the yield stress of the particle materials and is repeated from Chapter 4 again as

$$K_{1D} = 2\pi r^* \sigma_y \left[-6.76 \left(\frac{E^*}{\sigma_y} \right)^{-0.14} + 6.30 \right]. \tag{5.2}$$

For these simulations, the Young's modulus and density were fixed at 100 GPa and 5000 kg/m^3 respectively. Therefore, using Equation 5.2, the range of yield stresses used corresponds to a range of stiffness from 3.5×10^6 N/m to 4.8×10^7 N/m. The simulated speed of the stress wave traveling though the material was averaged over 20 layers for each stiffness and each geometry and shown as markers in Figure 5.9b. By again fitting curves to the numerical data we see that the wave speed of 2D and 3D elastic-plastic granular crystals continues to be proportional to the square root of the 1D contact stiffness. Now if we again scale the fittings based on the geometrical correction factors in Equations 5.1, the parameter fittings all collapse to a single curve. Just as with the density, the stiffness dependence exhibited by 1D granular chains can be easily scaled to 2D and 3D granular crystals.

As shown in the 1D case, knowing how the wave speed scales with the density and yield stress of the constituent materials, allows us to predict the stress wave propagation properties of new combinations of materials. We have now shown that this approach can be scaled to close packed 2D, and 3D granular crystals and allow us to predict the properties of increasingly complex systems of real materials. The predicted wave speeds through each layer in 1D, 2D and 3D granular crystals of four real materials are shown in Figure 5.10a. If we then take these wave speeds and normalize them both by materials properties and geometry according to Equation 5.1, we can define the following wave velocities for 2D and 3D elastic-plastic granular crystals:

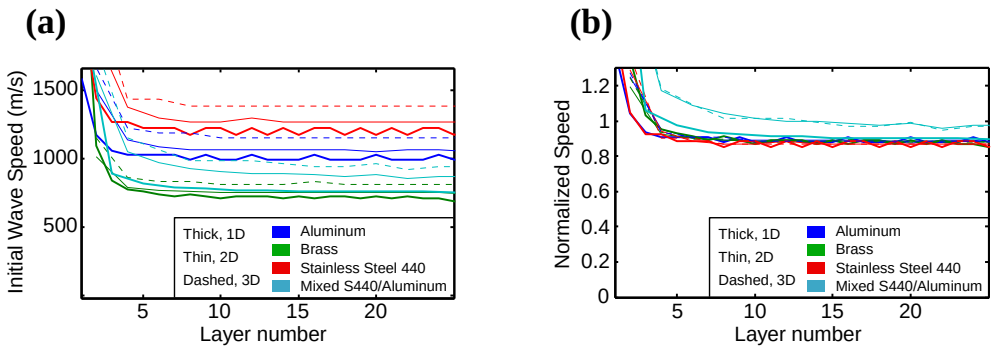

Figure 5.10: (a) Plots of the simulated local speed of the wave as it travel through 1D, 2D, and 3D arrangements of particles of real materials. (b) Plots of the simulated local speed of the wave as it travel through 1D, 2D, and 3D arrangements of particles of real materials normalized by the dependence on the stiffness, density, and the geometry.

$$V_{\max} = A\sqrt{\frac{3K_{1D}}{\pi R \rho_{\text{avg}}}},$$
$$A = \begin{cases} 1 & \text{for 1D} \\ \frac{3}{2\sqrt{2}} & \text{for 2D} \\ \frac{2}{\sqrt{3}} & \text{for 3D,} \end{cases} \tag{5.3}$$

where, as given in Chapter 4, K_{1D} is the stiffness in the elastic-plastic region given in Equation 5.2, R is the radius of particle, and ρ_{avg} is the average density of constituent particles.

The results of this scaling for the real materials used are shown in Figure 5.10b. We see that by normalizing by this predicted wave speed, all systems comprised of just one material collapse to a single curve. Therefore, by knowing the density of the constituent material and using Equation 5.2 to get the linear stiffness of the 1D contact, we can predict the initial wave velocity of 1D, 2D, and 3D close-packed, elastic-plastic granular crystals. It was previously shown in Chapter 4 that the normalization was also valid for 1D granular crystals with alternating materials. 2D and 3D granular crystals with alternating layers of 2 materials appear to have a slightly different normalized wave speed. This is perhaps due to a new deformation mechanism between hard and soft layers that violate the quasi-one dimensional nature of the previous periodic simulations, i.e., soft particles being pushed aside

by harder particles and moving in other dimensions which don't exist in 1D.

5.3 Heterogeneous Granular Crystals and Applications

5.3.1 Guided Impact Applications

We have shown that speed of stress waves due to impacts in elastic-plastic granular crystals is determined by the materials properties of the local constituent particles. Because granular systems give us the freedom to choose the materials properties of each individual particle we can create highly anisotropic materials with designed geometries. Using our understanding of the wave propagation properties in elastic-plastic granular crystals, we can create materials with designed responses to various impacts.

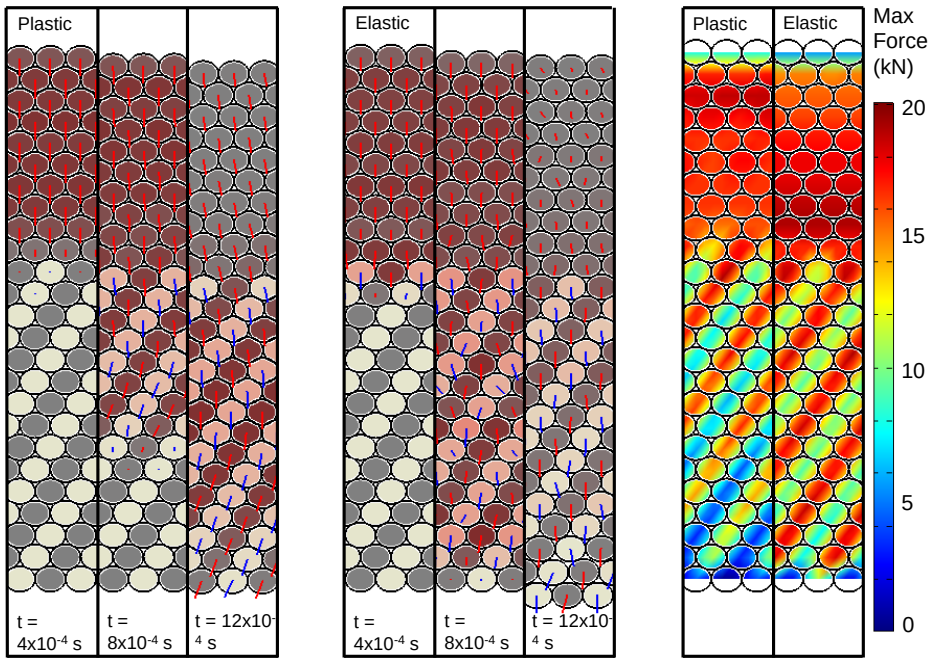

Figure 5.11: (a), (b) Depictions of the location, velocity, and force on each particle at different times following an impact on a system (a) with plasticity and (b) assuming only elastic (Hertzian) interactions between particles. Initial color represents the particle material with dark particles being stainless steel 440 and light particles being aluminum. Red color depicts force on the particle relative to the maximum forces experienced during the impact. Red and blue lines show the direction of the velocity of steel and aluminum particles respectively with the length of the line normalized by the maximum velocity in any of the particles at that time step. (c) Depiction of the maximum force felt by each particle during the impact for both contact laws.

An example is shown in Figure 5.11 where arrangements of stainless steel 440c and aluminum are used to create a change in the direction of particle velocities within a material. An initial impulse of $2F_p$ for the stainless steel 440c was applied to 25 layers of hexagonally close packed spheres which are 15 particles wide in the periodic direction. After 10 layers of stainless steel 440c, we introduced stripes of alternating aluminum and stainless steel 440c at a 60° interface angle. In Figure 5.11a, we see that as the wave entered into the striped region, after a few layers of transition, the particle velocities aligned with the stripes and traveled along the 60° interface. However, when only elastic interactions were assumed, the new geometry created some local oscillations in direction of the particle velocities, but the wave generally continued in the z-direction as seen in Figure 5.11b. Because the elastic-plastic particle systems allow us to control the local particle velocity, we can design materials with anisotropic and inhomogeneous wave propagation properties where impacts can be directed away from sensitive areas of materials and towards less sensitive areas. In Figure 5.11c we can also see that, in the elastic-plastic case, forces were dissipated within the material due to permanent plastic deformations and the maximum forces were lower in each subsequent layer of material. After just a few layers of heterogeneous elastic-plastic granular crystals, the direction of the particle velocities can be modified and controlled.

5.3.2 Snell's Law for Elastic-Plastic Granular Crystals

Previous work in the elastic regime has demonstrated that granular crystals in 2D and 3D allow for enhanced control of how energy propagates through a material after an impact [55, 57–59]. Various approaches have been explored to rationally designing impact protecting devices through numerical optimization [28, 54], randomization [29, 56], and adapting techniques from other fields such as optics and optical metamaterials [70]. In optics, lens are routinely used to focus electromagnetic energy and control the shape of an incoming wave. Based on curved interfaces between materials at which light waves travel at different speeds, the waves can be focused down to a point and concentrated as demonstrated by a magnifying glass lighting a piece of paper on fire using sunlight.

In order to focus a wave, the geometric shape of a lens can be calculated using Snell's Law. It says that the ratio of the angle of an incident plane wave to the angle of the transmitted wave which has been bent (refracted) after passing through an interface between two materials is equal to the ratio of the speeds at which the waves travel in the two materials. Therefore in order to design a lens, all that is needed is

knowledge of the wave speeds on either side of an interface. Electromagnetic waves travel at different speeds in air, glass, or plastic, and furthermore different frequencies of light travel at different speeds. If the wave speed's frequency dependence varies differently within the two materials, the different frequencies of the light will be bent at different angles. This creates "chromatic aberrations" where the various colors of light separate and focus differently creating a prismatic effect. Therefore, a lens is designed for a range of frequencies of electromagnetic waves.

Previous work showed that an analog to Snell's law could be obtained for oblique interfaces of particles of different mass in elastic granular crystals and depends on the ratio of solitary wave speeds in the two materials [61]. As previously discussed, the wave speed in elastic granular crystals is amplitude dependent. Therefore, waves of different amplitude would behave differently across an interface in an analog to the chromatic aberration in optical lens. However, by only varying the masses of the particles across the interface, the amplitude dependence on either side of the interface is equivalent and ratio of the wave speeds remains the same at any amplitude. Therefore, the refracted angle is predictable for that specific subset of elastic granular crystals.

For elastic-plastic granular crystals, we have previously shown that over a large range of forces, the speed at which plane waves travel is neither frequency dependent or amplitude dependent and is controlled by the material properties of the constituent particles. Therefore, we investigate here whether Snell's law is valid for general elastic-plastic granular crystals and, in the subsequent subsection, whether lenses can be designed to demonstrate the focusing of an impact wave.

Snell's law is typically written in the following form derived purely from geometric considerations:

$$\frac{\sin\Theta_{\text{inc}}}{\sin\Theta_{\text{ref}}} = \frac{V_1}{V_2}, \tag{5.4}$$

where, in this case, V_1 and V_2 were the solitary wave speed in each of the materials and Θ_{inc} and Θ_{ref} were the incident and refracted wave angles with respect to the angle of the interface [61]. We can rewrite Snell's law in more general and convenient form in terms of the interface angle with respect to an arbitrary horizontal axis, θ_i, and the angles of the incoming and bent waves, θ_1 and θ_2 respectively:

$$\theta_2 = \theta_i - \arcsin\Big(\frac{V_2}{V_1}\sin(\theta_i - \theta_1)\Big). \tag{5.5}$$

The angles involved in this formulation for Snell's law are shown in Figure 5.12.

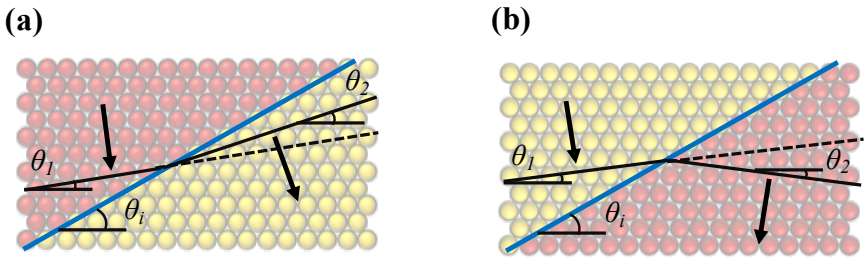

Figure 5.12: Schematic defining the angles involved in defining Snell's Law for elastic-plastic granular crystals. All angles are defined with respect to the 2D hexagonal-packing's horizontal direction. The blue line shows the interface between two types of dissimilar particles with angle θ_i. The incoming wave, making angle θ_1 with the horizontal, is shown to the left of the interface, propagating in the direction of the arrow. The transmitted (refracted) wave is shown to the right of the interface with angle θ_2 to the horizontal. (a) For waves traveling across an interface from faster wave speed to slower wave speed, θ_2 will be positive and the wave will be bent backwards. (b) For waves traveling across an interface from slower wave speed to faster wave speed, θ_2 will be negative and the wave will be bent forwards.

When V_2 is less than V_1, the transmitted wave is bend backwards with respect to the interface and θ_2 is positive for θ_i between 0° and 90°. When V_2 is greater than V_1, the transmitted wave is bend forwards with respect to the interface, up to a critical angle. At the critical interface angle, θ_2 becomes imaginary and total internal reflection of the wave is observed with no transmission into the second material. In the elastic case, the ratio of the wave speeds could be given as a function of the mass ratio of the two materials. However, in the elastic case, this relationship no longer generally held for interfaces between particles of both dissimilar masses and stiffness properties. For larger amplitude impacts in which plasticity occurs, it has been previously shown that the wave speeds in elastic-plastic granular materials can be estimated knowing solely the material properties of the constituent particles (Chapter 4). As amplitude of the initial impact grows the speed of the wave traveling through an elastic-plastic granular crystal approaches Equation 5.3. Therefore, we investigated whether the analog to Snell's law would hold for interfaces of arbitrary elastic-plastic granular crystals.

In order to determine how material parameters affect the refraction angle of the transmitted wave through oblique interfaces in elastic-plastic granular crystals, we performed simulations varying the density of the constituent particles, their yield

stress, and the amplitude of the excitation. First, we considered the case where V_2 is less than V_1 in which the wave is bent backwards with respect to the interface. A schematic of the numerical setup for these simulations is shown in Figure 5.13a. A representative surface of the simulated particle velocity is shown at a fixed time with contour lines of constant velocity showing the bend angle, overlaid above the arrangement of 6.35 mm diameter particles of the two materials (red and yellow spheres) arranged in a 60° wedge. The inset shows a top down view of the area over which the angle of the bent wave was calculated by averaging the slope of linear regressions of particle velocity contour lines. In all simulations, θ_1 is equal to zero because the initial wave is horizontal. θ_i is defined as the angle of the interface between the two types of particles with respect to the horizontal and θ_2 is the angle made by the contours of constant velocity with respect to the horizontal. In these simulations, the spheres in which the wave was initially excited (shown as red spheres in Figure 5.13a) were composed of a model material with Young's Modulus of 100 GPa, density of 5000 kg/m^3, and yield stress of 1000 MPa. The second materials' properties were individually varied in order to achieve the desired ratio of predicted wave speeds using Equation 5.3. Unless otherwise specified, a force pulse was applied to each of the particles in the first row with constant force amplitude of twice the force required to reach the linear plastic regime of the first particles as given by the elastic-plastic contact law ($F_0/F_P = 2$) and duration of 20×10^{-6} seconds.

Figure 5.13b shows the calculated angle of the bent wave through a 60° interface versus the predicted ratio of wave speeds for simulations varying material parameters as well as with combinations of real materials. Similar to the elastic case presented by Tichler el al. [61], Snell's law (the green curve) predicts the refracted wave's behavior most accurately when the mass of the two particles are varied while keeping stiffness properties the same across the interface (the blue curve). However, in previous work in the elastic regime, Snell's law was not used to predict the behavior of non-linear waves traveling across interfaces of materials whose stiffness properties vary. For uniform elastic-plastic granular crystals, the wave speed approached a constant value as amplitude increased predicted only by materials properties of the constituent particles. We see that for waves traveling across interfaces between elastic-plastic materials with dissimilar stiffness properties, the bend angle also tends towards the predicted value from Snell's law as amplitude increases (red curve and shaded region). Additionally, in order to investigate the effect of the initial non-linearity in the elastic-plastic contact law, a linear contact law with stiffness

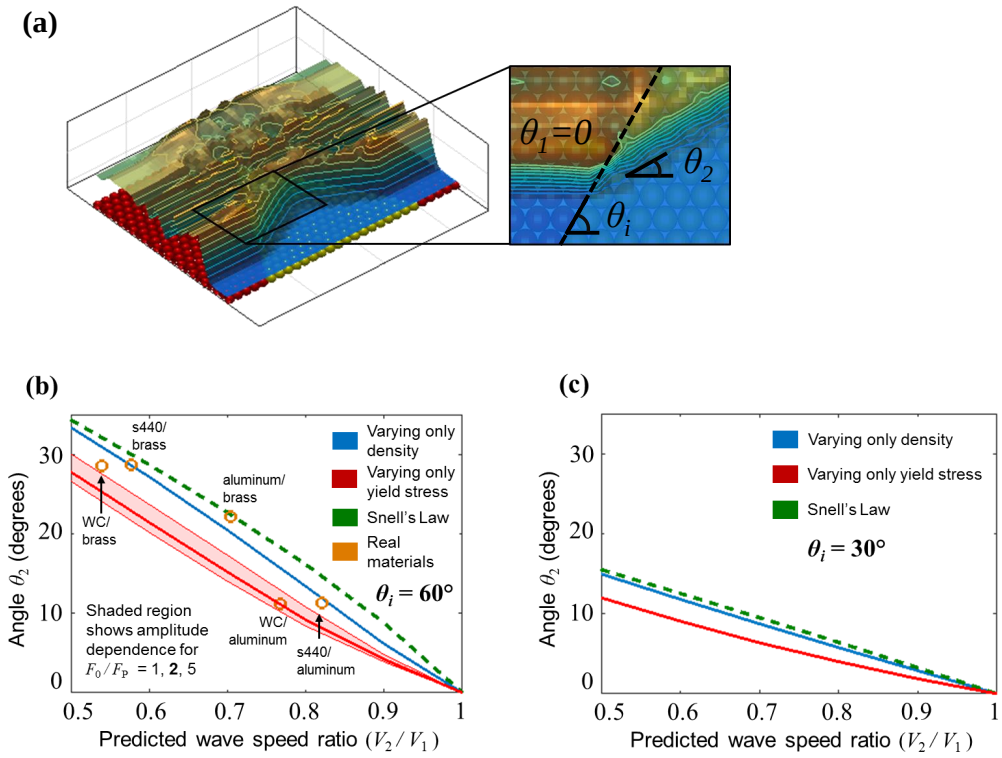

Figure 5.13: (a) Schematic of the numerical setup showing the arrangement of particles in a 60° wedge, a surface of particle velocity at a representative time, and contours of constant particle velocity from which the angles are computed. Inset shows the region over which the bend angle of the wave is computed by averaging the slopes of linear regressions of contour lines over time as the wave passes. (b) Plots showing the resulting angle of the wave after a horizontal wave passes through a 60° interface between dissimilar particles versus the ratio of the predicted wave speeds in uniform arrays of each particle for ratios of wave speeds less than one ($V_2/V_1 < 1$). The dashed green curve shows the prediction using Snell's law. The blue curve shows the resulting angle from simulations in which only the density was modified across the interface while keeping stiffness the same. Red lines show the the resulting angle from simulations in which only the yield stress was modified across the interface while keeping mass the same for 3 different amplitudes of applied force. Yellow markers show the resulting angle from simulations using various combinations of particles with the material properties of real materials. (c) Plots showing the resulting angle of the wave after a horizontal wave passes through a 30° interface between dissimilar particles versus the ratio of the predicted wave speeds in uniform arrays of each particle.

equivalent to the stiffness in the linear regime of the elastic-plastic contact law was used in simulations. In all cases, the bend angle across interfaces between dissimilar *linear* materials exactly coincided with the blue curve in Figure 5.13b, regardless

of amplitude or whether density or stiffness was varied. Therefore, the amplitude dependence and differences between angles observed in simulations and angles predicted by Snell's law when yield stress is varies must be a result of differences in the transition from elasticity to plasticity and the force required to reach the linear plastic regime between the two materials. Figure 5.13b also shows the simulated bend angle for different combinations of real materials and their predicted ratio of wave speeds.

In addition to the behavior of 60° interfaces, interfaces between materials at other angles to the hexagon packing were investigated. Figure 5.13c shows the calculated angle of the bent wave through a 30° interface while varying the same parameters and compares them to the prediction from Snell's law. We see the same trends as discussed for the previous figure.

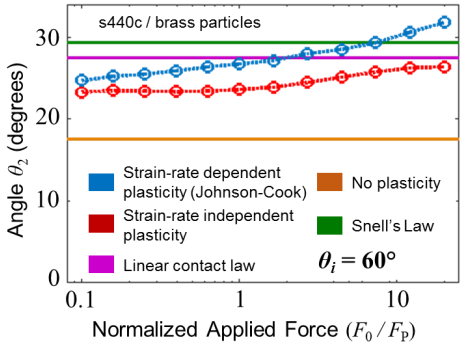

Figure 5.14: Plots showing the resulting angle of the wave after a horizontal wave passes through a 60° interface between stainless steel 440c particles into brass particles versus the amplitude of the applied force, normalized by the force required to reach the linear plastic regime in the steel particles. The green curve shows the prediction using Snell's law. The blue curve and markers show the resulting angle from simulations involving the fully strain-rate dependent model of the elastic-plastic contact law. The red curve and markers show the resulting angle of simulations where the contact law is not strain-rate dependent. The purple curve shows the resulting angle from simulations involving a linear contact law with the same stiffness as the linear regime in the elastic-plastic contact law. The orange curve shows the resulting angle from simulations using a purely elastic (Hertzian) contact law neglecting plasticity.

To investigate how amplitude affects the accuracy of Snell's law in predicting the bend angle of waves across the oblique interface of dissimilar materials, simulations were performed on a 60° interface of stainless steel 440c and brass particles with

different amplitude force pulses applied to the first row of particles, all of 20×10^{-6} second duration. Figure 5.14 shows plots of the bend angle of the transmitted wave versus the applied amplitude (normalized by the force required to reach the linear plastic regime in the first material, F_p). Various modifications to the contact law were made in order to investigate which aspects of the contact law affect the applicability of Snell's law. With no plasticity (orange curve), Snell's law differs greatly from the simulated angle, suggesting that it does not apply in the elastic regime for materials with different stiffnesses as shown previously [61]. The purely elastic granular crystals do not exhibit amplitude dependence, as observed by Tichler el al., because the wave speed scales with amplitude equivalently between the two materials (although the scaling in non-linear). Using a linear model (cyan curve), the wave speeds are amplitude independent and therefore the angle is also constant and nearly the value predicted by Snell's law (green curve). The constant discrepancy of approximately 2° is most likely caused by the discretization of particles (the angled line is approximated by a series of steps) or possibly because the particles cannot carry tension, allowing gaps to form, although further investigation is required. With a strain-rate independent elastic-plastic contact law, the wave speeds in the material approached a constant as the amplitude increases past the amplitude required to reach the linear plastic regime in the contact law. Analogously, the bend angle also approaches a constant (red curve) identical to the constant angle exhibited by the linear contact law simulations. Because these simulations involve stainless steel 440c particles which are highly strain-rate dependent, the most realistic model is the full strain-rate dependent elastic-plastic model (chapter 33). The wave speed in the stainless steel particles continues to increase with amplitude due to the strain rate dependence while the wave speed in the brass particles approaches a steady value. Therefore, the angle continues to grow with increasing amplitude and eventually exceeds the value predicted by Snell's law (blue curve). However, for over an order of magnitude, the angle is within a few degrees of the angle predicted by Snell's law.

Next, we investigated the case where V_2 is greater than V_1 and the transmitted wave is bent forwards with respect to the interface. In order to avoid reaching the critical angle at which total internal reflection occurs, smaller interface angles where used in this case. A schematic of the numerical setup is shown in Figure 5.15a with an inset showing the region over which the bend angle was calculated from contours of constant particle velocity. Figure 5.15b shows the calculated angle of the bent wave through simulations of a 15° interface while varying the density and compares

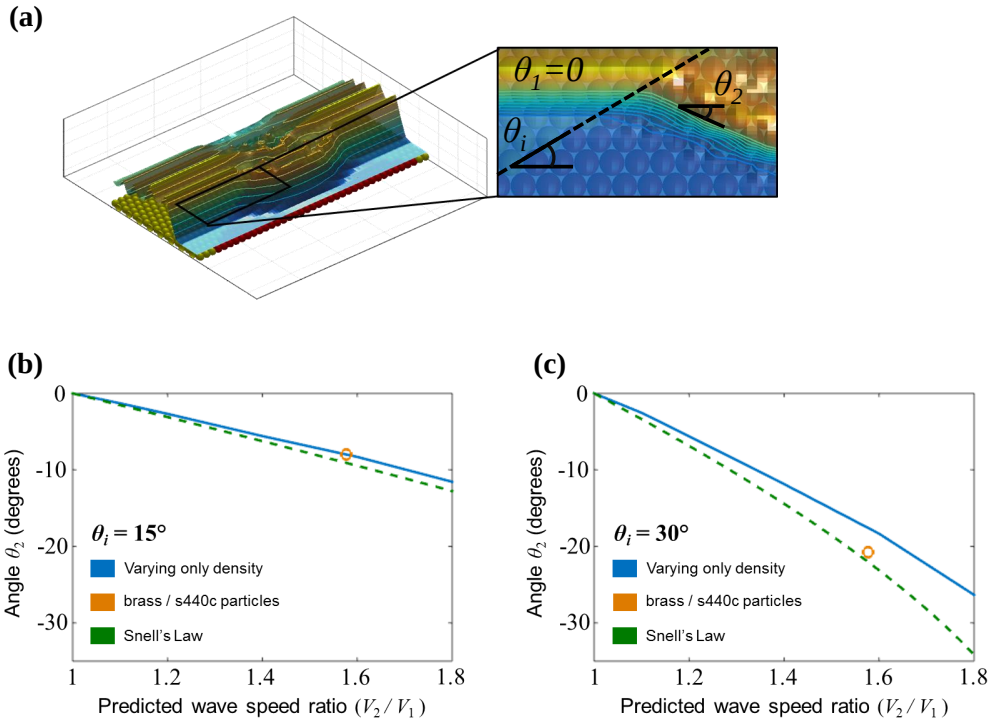

Figure 5.15: (a) Schematic of the numerical setup showing the arrangement of particles in a 30° wedge, a surface of particle velocity at a representative time, and contours of constant particle velocity from which the angles are computed. Inset shows the region over which the bend angle of the wave is computed by averaging the slopes of linear regressions of contour lines over time as the wave passes. (b) Plots showing the resulting angle of the wave after a horizontal wave passes through a 15° interface between dissimilar particles versus the ratio of the predicted wave speeds in uniform arrays of each particle for ratios of wave speed greater than one ($V2_/V_1 > 1$). The dashed green curve shows the prediction using Snell's law. The blue curve shows the resulting angle from simulations in which only the density was modified across the interface while keeping stiffness the same. Yellow marker shows the resulting angle from simulations of a brass array with a wedge of stainless steel 440c particles in a 15° wedge. (c) Plots showing the resulting angle of the wave after a horizontal wave passes through a 30° interface between dissimilar particles versus the ratio of the predicted wave speeds in uniform arrays of each particle.

them to the prediction from Snell's law. Snell's law accurately predicts the bend angle for the model materials of varied density as well as for the simulation of brass particles with a 30° wedge of stainless steel 440c particles (yellow marker). Figure 5.15c shows the calculated angle of the bent wave through simulations of a 30° interface while varying the density and compares them to the prediction from Snell's law. Again we see good predictions from Snell's law for model materials as well

as the brass/stainless steel 440c particles (yellow marker) although the predictions begin to diverge at higher wave speed ratios. For a 30° interface, the θ_2 becomes imaginary (total internal reflection and zero transmission) at a wave speed ratio of 2. Therefore, the predictions become less accurate because the amplitude of the forces is significantly decreased in the second material and the wave speed prediction is no longer accurate as the contact do not reach the fully plastic regime.

5.3.3 Impact Lens Design

Because we can predict the angle of refraction of the impact wave across any angled surface, we can also calculate the shape of the wave across more complex non-linear interfaces. This allows us to create useful wave shapes for impact protection such as spherically converging or diverging waves. Using Snell's law as an estimate for bending angle of a wave after transmission through an oblique interface, we can design heterogeneous elastic-plastic granular crystals that behave as impact lenses and provide control over the flow of energy within the material. Despite the inconsistencies in the predictions given by Snell's law and the actual simulated bending angle attributed to amplitude dependence, discreteness, and the non-linearity of the contact law, the simple impact lenses designed here demonstrates the capability to direct significant portions of the impact forces and energy toward a desired focal region.

Using circular interfaces between two dissimilar materials with large differences in wave speed, we can imitate spherical lenses used in optics to focus impact forces. Figures 5.16 and 5.17 show the focusing of an impact wave through a lens composed of brass spheres embedded in an array of stainless steel 440c spheres. This lens is designed to have the shortest focal length given some restrictions of the system. Specifically, for wave speed ratios greater than one, we observed that if the interface angle becomes too high, we approach the critical angle at which we see total internal reflection and Snell's law becomes inaccurate. To avoid this situation, we minimize the curvature of the back face of the spherical lens and allow significant curvature of the front face up to a maximum interface angle to 60°. This creates a plano-convex lens in which the radius of the back face approaches infinity (becomes flat). A force pulse of five times the force required to reach the linear plastic regime in the steel spheres ($5F_p$, approximately 26 kN per sphere) with a duration of 20×10^{-6} seconds is applied to the first row of particles. The arrangement of the steel and brass particles is shown in Figure 5.16a with a surface of the maximum kinetic energy of each particle during the initial impact wave overlaid above the particles. The

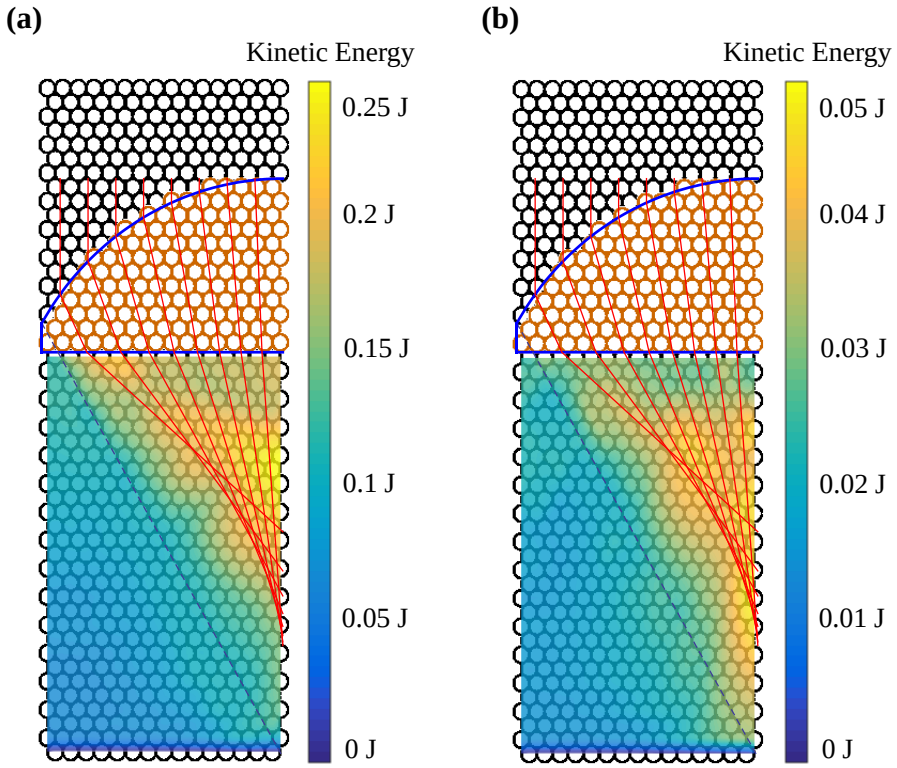

Figure 5.16: Surfaces of the maximum kinetic energy of each particle during initial impact overlaid above a schematic of the impact lens arrangement of stainless steel 440c (black circles) and brass (orange circles) particles. Thick blue lines show the ideal circular lens interfaces and red lines show the path of rays calculated using Snell's law at each face of the lens. (a) Kinetic energy of particles after a force pulse of amplitude $5F_p$ with duration of 20×10^{-6} seconds. (b) Kinetic energy of particles after a force pulse of amplitude $2F_p$ with duration of 20×10^{-6} seconds.

simulations are performed with symmetric boundary conditions on the sides. The circular surfaces of the lenses are approximated by the circular interface between the particles (shown as the thick blue lines in Figure 5.16a). The red lines show the path of ray traces calculated using Snell's law given in Equation 5.5 across the ideal circular lenses. The kinetic energy is successfully concentrated near the focal region predicted by the ray tracing and directed away from the opposite side of the sample. Despite the discrete nature of the interface that restricts our ability to accurately reproduce circular interfaces between materials, the impact lens designed using elastic-plastic granular crystals is effective at focusing impact energy. Figure 5.16b shows a surface of the maximum kinetic energy of each particle during a smaller impact wave with initial force amplitude of just twice the force required to reach the

linear plastic regime in the steel spheres ($2F_p$, approximately 10.5 kN per sphere) with a duration of 20×10^{-6} seconds. We do not observe any major differences in the focusing of the impact energy based on the amplitude of the impact wave as expected. Therefore, we do not need much advance knowledge of the character of the wave in order to design an effective lens.

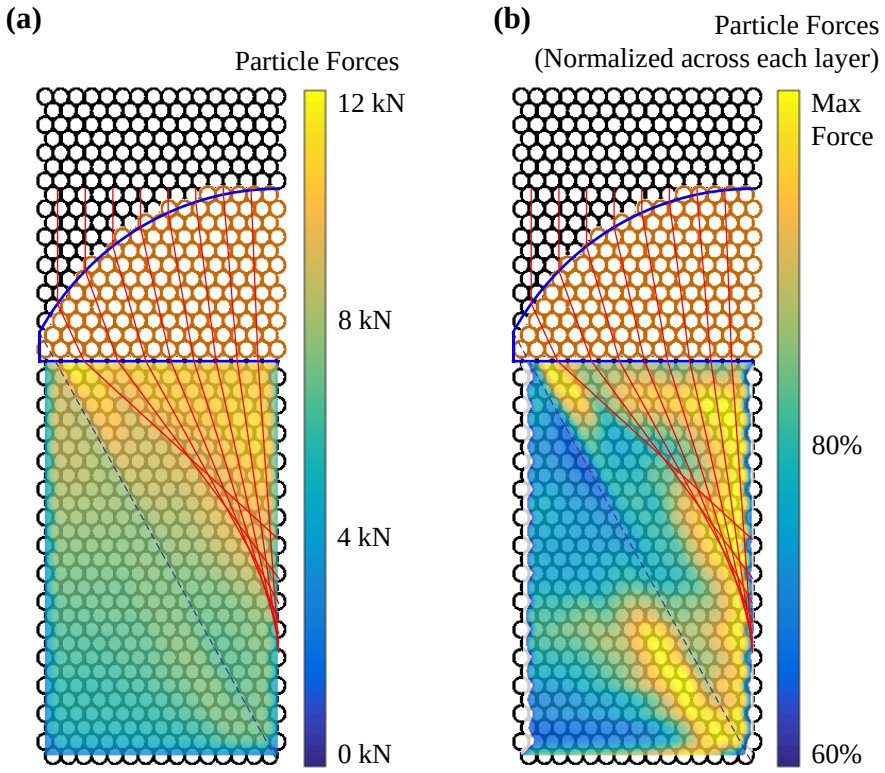

Figure 5.17: (a) Surface of maximum forces experienced during the initial impact by each particle, again overlaid above the schematic of the lens with predicted ray paths. (c) Surface of maximum forces experience by each particle normalized by the highest maximum force within that particle's layer, again overlaid above the schematic of the lens with predicted ray paths.

Additionally, Figure 5.17a shows surfaces of the forces experienced by each particle overlaid over the arrangement of particles and the ray tracing derived from the ideal spherical lens. As with the kinetic energy of the particles, the forces are also higher in the focal region although it is masked by the dissipation of forces as the wave travels through each subsequent layer. In order to show the effect of the focusing, we can normalize the force in each layer by the maximum force in that layer, as shown in the surface in Figure 5.17b. We can see that, within the layers in the focal region, the forces are directed towards the focus and then begin to

diverge after passing through and continuing to dissipate. Furthermore, the forces are directed away from the side of the sample opposite the focal region showing that the lens would provide protection to that area from the forces of the impact.

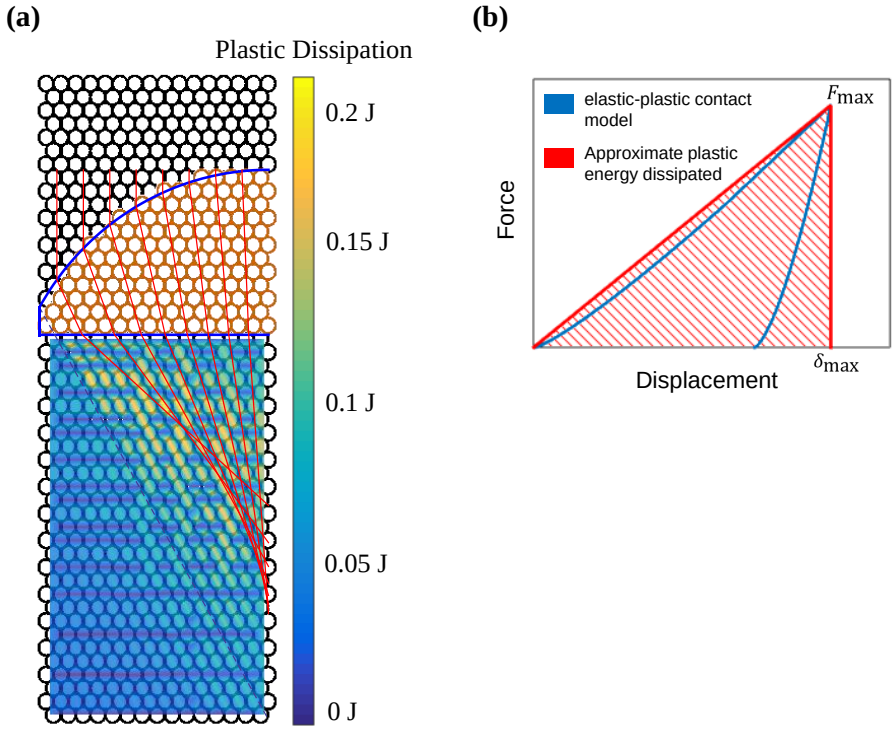

Figure 5.18: (a) Surface of approximate energy dissipated by plastic deformation at each contact point after an impact, overlaid above the schematic of the lens with predicted ray paths. (b) Schematic of the approximate of the energy dissipated by plastic deformation based on the area under the red curve defined by the maximum force and displacement experienced at each contact point. The blue curve shows the elastic-plastic contact law.

To display the lens's effect on the localization of impact damage, Figure 5.18a shows a surface of the approximate energy dissipated through plastic deformation at each contact point. The approximate plastic energy dissipation, PE, is defined as:

$$PE = \frac{1}{2}\delta_{\max} F_{\max}, \tag{5.6}$$

where $\delta_{\max}$ and $F_{\max}$ are the maximum displacement and force experienced at each contact respectively during the simulation. A schematic of energy dissipation as it relates to the force-displacement relationship between the particles in shown in Figure 5.18b. In the surface of plastic dissipation in Figure 5.18a, we see that

significantly more energy is being dissipated in the focal region corresponding to more damage through plastic deformation being done in that region. Conversely, there is very little dissipation occurring in the region opposite the focal region where very little damage is observed after the wave passes.

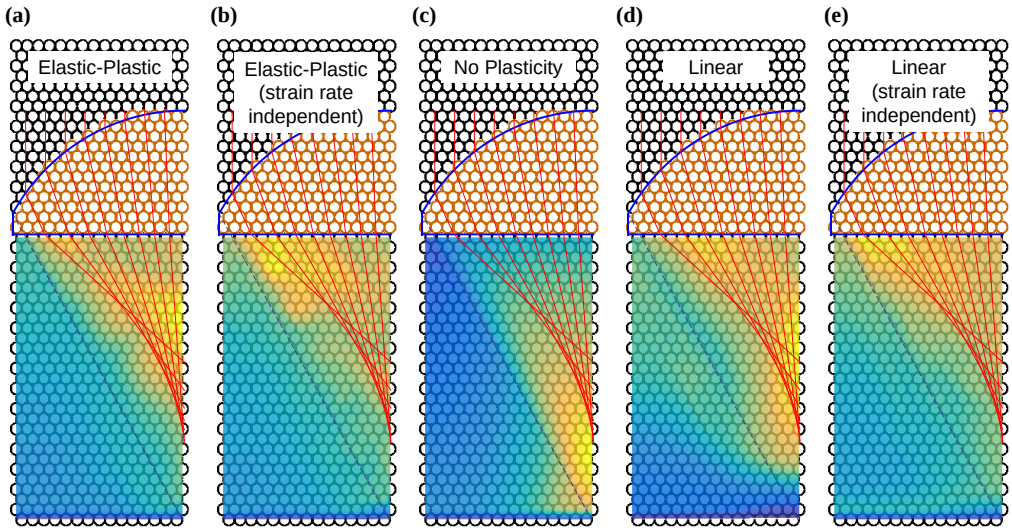

Figure 5.19: Surfaces of the maximum kinetic energy (normalized) of each particle during initial impact overlaid above a schematic of the impact lens arrangement of stainless steel 440c (black circles) and brass (orange circles) particles. Thick blue lines show the ideal circular lens interfaces and red lines show the path of rays calculated using Snell's law at each face of the lens. Each subfigure shows the kinetic energy of particles whose contact interaction is defined by a different model: (a) elastic-plastic model, (b) strain rate independent elastic-plastic model, (c) no plasticity (Hertzian), (d) linear with stiffness equivalent to stiffness in the plastic regime of the elastic-plastic model, and (e) linear with no strain rate dependence.

Next, we compared the results of simulations of the impact lens using the strain rate dependent elastic-plastic model to describe the interactions between particles to other simplified contact models in order to observe the contribution of each aspect of the contact law to the overall behavior and performance of the impact lens. Figure 5.19 shows the focusing on kinetic energies after passing through the impact lens arrangement of stainless steel 440c and brass particles for different contact laws: (a) elastic-plastic model presented in Chapter 3, (b) an elastic-plastic model with strain rate dependence neglected, (c) a purely elastic model with plasticity neglected (Hertzian contact), (d) a linear contact law with the strain rate dependent stiffness equivalent to the stiffness in the fully plastic regime of the elastic-plastic contact law, and (e) a linear contact law neglecting strain rate dependence. We

showed previously that Snell's law was more predictive for some contact laws than for others. Snell's law was most accurate for the elastic-plastic and linear contact laws however the focusing power of the lens also depends on energy dissipation as well. The elastic-plastic law that neglects strain rate dependence has unrealistic dissipation in the stainless steel particles and therefore has more mild focusing. The same effect can be seen in the linear strain rate dependent and independent models. It was previously shown that Snell's law does not accurately predict the behavior of interfaces between dissimilar elastic particles and therefore. This is also evident in Figure 5.19c. Instead of kinetic energy being focused along the ray trace paths predicted by Snell's law in the lens, the kinetic energy is more controlled by the underlying arrangement of particles and shows a significant drop in energy to the left of the dashed line identifying a 60° interface from the corner of the lens. The simulations with elastic-plastic and linear contact laws defining particle interactions appear insensitive to the underlying arrangement of particles and their behavior depends instead on the profile of the interface as desired, but the systems with elastic particles remains dependent on the particles' packing.

The effect of the contact model on the behavior of the impact lens systems is shown again in Figure 5.20. Figure 5.20a shows a schematic of the lens arrangement and a legend describing the different contact models used: blue represents the elastic-plastic contact model, red represents the strain rate independent elastic-plastic contact model, green represents an elastic (Hertzian) contact, orange represents a linear contact model, and magenta represents a strain rate independent linear contact model. Figure 5.20b, Figure 5.20c, and Figure 5.20d show the kinetic energy distribution within each of the the layers shown in Figure 5.20a, normalized by the maximum kinetic energy of any particle within that layer. Because no energy is dissipated in the elastic-only materials, without normalization, the kinetic energies widely vary between material models. Therefore, the normalization allows us to observe the impact of the contact model on the focusing ability of the realistic impact lens. In the focusing region shown in Figure 5.20c, we see that the models that include the realistic strain rate dependence are able to direct more of the energy to the focus region and away from the opposite side of the layer. As shown qualitatively, the strain rate independent materials (red and magenta curves) unrealistically dissipate more energy reducing the focus of energy. We also see in Figure 5.20c and 5.20d, that the elastic model (green curve) does not "focus" until much later because it is being influenced by the hexagonal particle packing and not by the shape of the interface between materials.

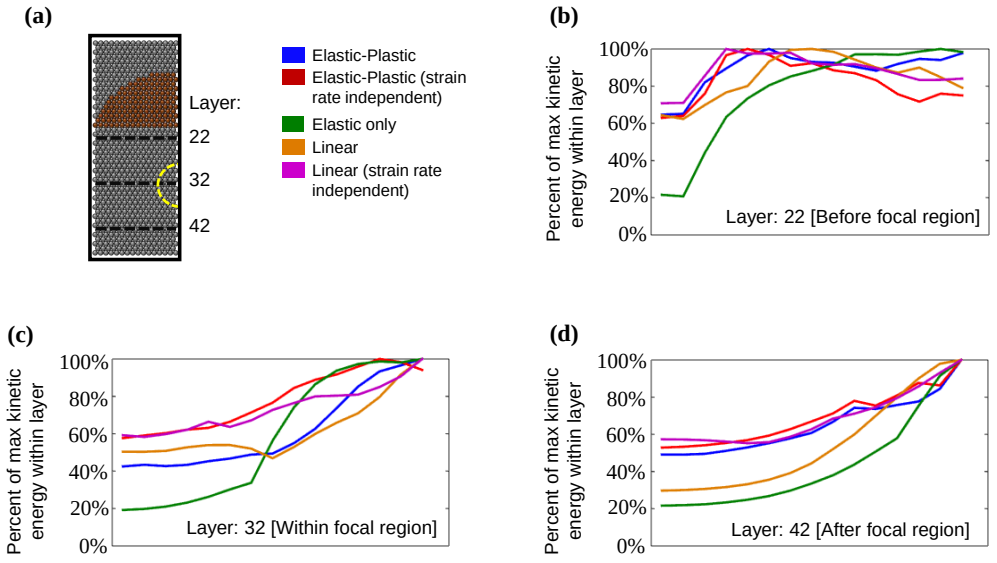

Figure 5.20: (a) Schematics of the particle arrangement used in simulations of performance of the impact lens for different contact models as well as dashed lines to show the vertical locations of the layers used in (b),(c), and (d). In all subfigures, blue corresponds to particles interacting via the elastic-plastic model, red corresponds to the strain rate independent elastic-plastic model, green corresponds to no plasticity (Hertzian), orange corresponds to linear with stiffness equivalent to stiffness in the plastic regime of the elastic-plastic model, and magenta corresponds to linear with no strain rate dependence. (b) Plot of the kinetic energy of each particle across the 22nd layer (before the focal region) of particles, normalized by the maximum kinetic energy within that layer for each of the five contact models. (c) Plot of the normalized kinetic energy of each particle across the 32nd layer (within the focal region). (d) Plot of the normalized kinetic energy of each particle across the 42nd layer (past the focal region).

In order to evaluate the effectiveness of the impact lens composed of elastic-plastic particles, we also performed simulations using uniform arrangements of brass and stainless steel 440c particles as well as an arrangement with a flat brass strip with the same height of the lens. Schematics of the arrangements of the particles in these additional simulations are shown in Figure 5.21a. The kinetic energy across horizontal layers of each simulation are shown in Figure 5.21b, 5.21c, and 5.21d. Figure 5.21b shows the kinetic energy for each simulation across a layer before the focal region, while Figure 5.21c shows the kinetic across a layer within the focal region, and Figure 5.21d shows the kinetic energy across a layer after the focal region. We observe a very clear peak of the kinetic energy within the focal region and see that the minimum kinetic energy on the side opposite the focus is less than

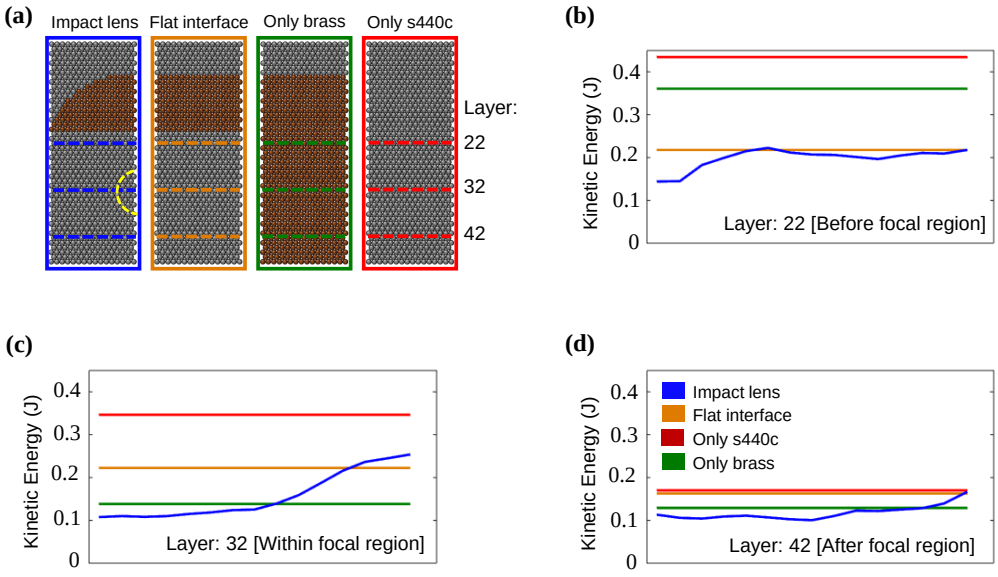

Figure 5.21: (a) Schematics of the particle arrangements used in simulations as well as dashed lines to show the vertical locations of the layers used in (b),(c), and (d). In all subfigures, blue corresponds to the simulation results for the impact lens arrangement, orange to a section of brass with flat interfaces with the same height as the lens, green to an arrangement with only brass particles, and red to an arrangement with only stainless steel 440c particles. (b) Plot of the kinetic energy of each particle across the 22nd layer (before the focal region) of particles for each of the four simulated arrangements. (c) Plot of the kinetic energy of each particle across the 32nd layer (within the focal region). (d) Plot of the kinetic energy of each particle across the 42nd layer (past the focal region).

the kinetic energy at the same region for any of the other particle arrangements. Not only is the kinetic energy lower than the arrangement with flat interfaces where the lens is replaced with a brass strip, it is also lower than the arrangement with all brass where energy continues to be dissipated more quickly as the wave continues to propagate in the brass. Therefore, the impact lens is effectively focusing the impact energy towards the focal region and away from the areas away from the focus. After focusing, the impact energy begins to diverge again the energy becomes more uniform across the width of the sample. However, the energy still remains lower in most regions than for the uniform brass arrangement because the concentration of forces in one region led to more plasticity and more energy dissipation than in the uniform arrangement. While dissipation was concentrated into specific regions after the wave passed through the lens, more total energy was dissipated than when it was dissipated evenly in the uniform arrangements.

We also compared the impact lens with random arrangements of particles. In one arrangement, just the layers which comprise the lens are replaced by randomly distributed brass and stainless steel 440c particles. In the second arrangement, every subsequent layer after the layer at which the lens begins are replaced with a random distribution of particles. For both such arrangements, five independent trials were simulated and compared with simulation results from the impact lens. Figure 5.22 shows schematics of the arrangements and plots of kinetic energy at different layers after an initial force pulse. The blue curves in Figure 5.22b, 5.22c, and 5.22d show the kinetic energy across the layers of the impact lens shown in the schematic in Figure 5.22a. The thick green curves show the average kinetic energy at each location across those same layers averaged over the five independent trials of the arrangement with only the lens-area replaced with randomly distributed particles. The green shaded area bounds the maximum and minimum kinetic energies of any one particle at any location within that layer for any of the five simulations for that arrangement. The thick red curves show the average kinetic energy at each location across those same layers averaged over the five independent trials of the arrangement with the entire area replaced with randomly distributed particles. Again the shaded area bounds the maximum and minimum kinetic energies for that arrangement.

In Figure 5.22b, before the focusing region, we see that there is a very broad distribution of kinetic energies within the random layers (represented by the shaded regions), but that the averages are fairly similar, showing that a similar amount of energy has been dissipated in the layers containing the lens. The kinetic energies within the focal region show in Figure 5.22c, shows that the random arrangement of particles is very effective at continuing to dissipate more energy than the uniform arrangements of particles. Within the focal layer, the minimum kinetic energy almost exactly matches the minimum kinetic energy for the impact lens opposite the focal region. However, the maximum kinetic energy of the random arrangement is nearly double the minimum and the distribution of the kinetic energies within the layer is inherently random. Therefore, the impact lens matches the energy dissipation performance of a random distribution of the same type of particles with the added spatial control over where the minimum and maximum kinetic energies occur. However, it is evident in Figure 5.22d, that the random arrangements of particles continues to be effective at dissipating energy as the wave propagated farther while the impact lens does not dissipate as much energy after the focal region. Therefore, the impact lens is most effective at quickly controlling the spatial distribution of kinetic energy within the particle system, while a random distribution

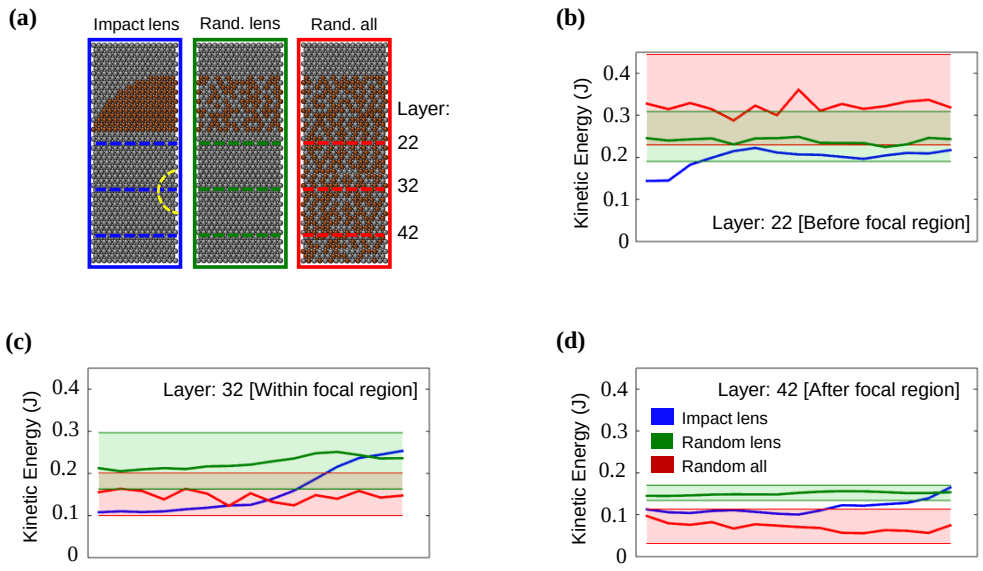

Figure 5.22: (a) Schematics of the particle arrangements used in simulations of performance of the impact lens versus random arrangements of particles as well as dashed lines to show the vertical locations of the layers used in (b),(c), and (d). In all subfigures, blue corresponds to the simulation results for the impact lens arrangement, green corresponds to an arrangement in which the layers containing the lens are replaced with a random assortment of brass and stainless steel 440c spheres, and red corresponds to an arrangement in which all layers are comprised of a random assortment of brass and stainless steel 440c particles. For each random assortment, five different trials were run. Thick lines represent the average kinetic energy at each location over the five trials for each arrangement, while thin lines and shaded regions represent the maximum and minimum kinetic energies of any particle within the layer over all of the five trials for each arrangement. (b) Plot of the kinetic energy of each particle across the 22nd layer (before the focal region) of particles for each of the three types of arrangements. (c) Plot of the kinetic energy of each particle across the 32nd layer (within the focal region). (d) Plot of the kinetic energy of each particle across the 42nd layer (past the focal region).

of particle would be more effective at continual dissipation over long distances.

This simple impact lens could be improved in a number of ways. Because spherical interfaces were used, this lens introduced spherical aberration visible in the ray tracing in Figures 5.16 and 5.17. Rays emitted from a highly curved spherical lens do not converge to a single point. Exact surfaces to focus all rays to a single point can be calculated numerically using Snell's laws. We also observed that Snell's law was more accurate for smaller ratios of wave speeds and for smaller interface angles. Therefore, materials could be chosen to minimize the differences in wave speed and

many stages of impact lenses could be used. The lens demonstrated here only used two types of materials, but many subsequent layers of materials could be combined to more slowly and accurately control the flow of energy. Finally, by expanding the width of the lens (or equivalently shrinking the particle size), the effective distance between the edge of the lens and the center where the energy is focused can be grown. The size of this lens was chosen due to limitations on simulation duration, not optimization of focusing power.

5.4 Summary of Chapter

In this chapter, we began by experimentally validating our approach to simulating impact waves through 2D and 3D granular crystals composed of elastic-plastic spherical particles. Using a sliding rig to impact 2D arrays of hexagonally packed particles and a drop tower to do preliminary experiments on 3D arrays of densely-packed particles, we showed that the assumptions required to efficiently simulate large heterogeneous systems of particles captured the relevant physics. These simulations allowed us to investigate the properties of waves propagating through these materials and extend the observations made about the wave speed in 1D materials to higher dimensional, 2D and 3D granular crystals. Additionally, we showed that by knowing the wave speed, we can use an analog of Snell's law for electromagnetic waves to design materials to control the propagation of impact energy like a lens.

Chapter 6

SUMMARY AND FUTURE DIRECTIONS

6.1 Summary

In this thesis, we studied the effects of plastic deformation on the dynamics of impacts on single contacts between grains, and on 1D, 2D, and 3D granular crystals. For small impacts in which all particles remained elastic at the contact, granular crystals have demonstrated unique properties which could be applicable to impact protection. Therefore, our aim was to extend previous work into new regimes that would be more suitable and realistic for these applications. We developed a model for incorporating plasticity into the contact behavior and revealed the details of dynamic wave propagation in elastic-plastic granular materials. Through extensive experimentally validated simulations, we revealed the unique properties of these materials, distinct even from our understanding of elastic granular crystals. We used this understanding to begin to show how this approach can be used to design new material systems for applications in impact mitigation.

In Chapter 3, we presented a new model for the dynamic compression of elastic-plastic spherical particles. We designed this model to be valid for a wide variety of types of materials to facilitate a large design space. Through parametric FEM studies, we were able to describe the remaining empirical parameters of the model purely as functions of the material properties of the constituent particles. Furthermore, by incorporating a description of the strain-rate dependence into the yield stress ensured that the model was valid for all types of loading. We experimentally validated the model using Hopkinson bar experiments on contacts between two hemispherical particles. By varying the amplitude and loading rate in these experiments, we showed that the model remains valid for any dynamic event through loading and unloading, as well as for a variety of materials.

In Chapter 4, we studied long 1D chains of particles with elastic-plastic contacts. Using the Hopkinson bar again, we experimentally validated our dynamic simulation approach as well as provided further validation of the elastic-plastic contact law. Because much of the impact energy was dissipated within the chain by plastic deformations, a laser vibrometer was used to measure the particle vibrations at the end of the chain which were then compared with results from simulations. Of

particular interest was understanding the speed at which waves traveled with plastic deformation. We showed that over a large range of impacts, the wave speed can be predicted solely by the material properties of the constituent particles, including for heterogeneous chains of alternating particles. The wave speed and dissipation of the dimer chains were even shown to exceed the bounds of uniform chains of the constituent materials.

In Chapter 5, we extended our simulation approach to 2D and 3D arrangements of densely packed elastic-plastic particles. First, we provided experimental validation of the simulations using a sliding rig to impact 2D arrays and a drop weight tower to impact two-layer 3D arrangements of spherical particles. These experiments showed that the assumptions made in the simulations were valid and that the dynamics were not significantly influenced by tangential forces between the particles. With simulations of 1D, 2D, and 3D granular crystals, we showed that the descriptions of the wave speed in 1D can be scaled to 2D and 3D. Lessons from optics show that, with knowledge of the speed at which waves travel in a material, the geometry of the interfaces between materials can be designed to influence the propagation of waves. Therefore, we applied Snell's law to show that lenses can be designed to focus impact wave energy in an analogous fashion to lenses. We compared the 2D lens with elastic-plastic contacts to other particle arrangements to demonstrate the capability to focus impact energy. A 3D version of the impact lens arrangement simulated in 2D is shown in Figure 6.1.

6.2 Future Directions

In this work, we restricted our study of 3D granular crystals to dense packings of spherical particles. We observed in 2D hexagonal packing that direction of wave propagation through the crystal did not affect the velocity of elastic-plastic waves and assumed that this would also be true of densely packed 3D materials. However, non-dense materials could be made by incorporating a compliant support structure to initially hold particles in place but not interfere with contact properties during an impact. Using non-dense anisotropic particle packings, the wave speeds could be tuned in different directions allowing for increased control over anisotropic wave speeds within the material.

In our work, we only used readily available, spherical particles comprised of common materials available from commercial suppliers. As we saw, every change in contact behavior leads to dramatically different dynamics and therefore even slightly

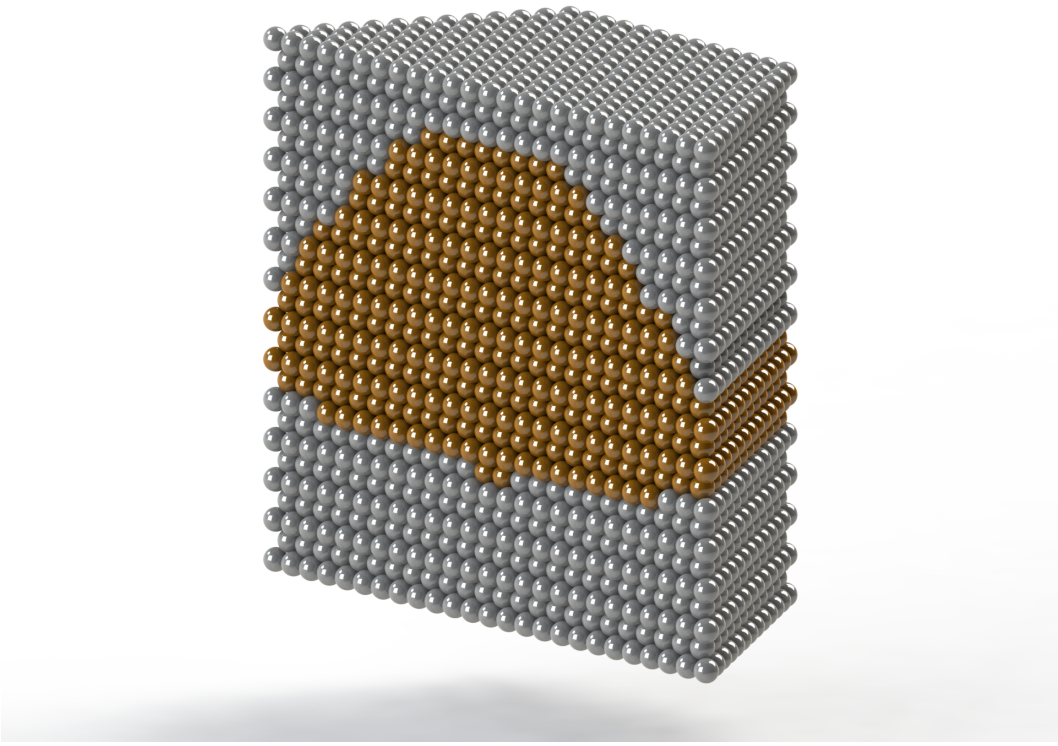

Figure 6.1: Rendering of a 3D impact lens comprised of stainless steel 440c and brass spheres.

modifying the particles shape and material properties could unlock entirely new and unique dynamics not explored in this thesis. For example, hollow particles could be incorporated in order to dissipate more energy locally through crushing of particles. Cylindrical elastic particles have a different power law dependence in the force-displacement law which depends on the alignment of particles [88]. Elastic-plastic cylinders would also have a modified contact-law and could allow for additional tuning of impact wave propagation properties. Also, shape memory alloys could be used to tune the particles' force-displacement response through precisely chosen phase changes in the material during deformation.

We demonstrated that elastic-plastic waves travel through these materials have a very specific speed that is dominated by the material properties of the constituent particles. Future work could experimentally investigate the nature of shocks in elastic-plastic granular materials when the impact velocity exceeds the characteristic wave speed in the material. What would be the shock speed in these materials?

How would plastic dissipation occur? Would any of the spatial control over the distribution of energy still occur with these types of shocks? If the particle velocity directions still respond to interfaces between materials as we showed with the elastic-plastic version of Snell's law, then perhaps similar impact lens designs could be obtained for very high velocity impacts beyond the characteristic wave speed determined in this work. Even if Snell's law does not remain valid, perhaps the direction of the particle velocity in the material can still be influenced by material choices at extremely high velocity. If possible, possibly with a composite of continuum and granular materials, spallation from the back surface can be influenced and controlled. Micrometeor and orbital debris protection systems on spacecraft typically use a Whipple shield to stop small debris by using layered aluminum and Kevlar with gaps between. While the debris might penetrate some of the layers, the goal is to break up the impact into smaller and smaller bits of debris through subsequent layers in order to prevent them from fully penetrating the shield. With more control over the direction of the particle velocities of debris after an impact, the obliquity of the cloud of debris could be increased through each subsequent layer, decreasing the angle at which it impacts the next layer and increasing the chances that it will not penetrate.

BIBLIOGRAPHY

[1] Heinrich M. Jaeger, Sidney R. Nagel, and Robert P. Behringer. "Granular solids, liquids, and gases". In: *Reviews of Modern Physics* 68.4 (Oct. 1996), pp. 1259–1273. DOI: 10.1103/RevModPhys.68.1259. URL: http://journals.aps.org/rmp/abstract/10.1103/RevModPhys.68.1259.

[2] P. G. de Gennes. "Granular matter: a tentative view". In: *Reviews of Modern Physics* 71.2 (Mar. 1999), S374–S382. DOI: 10.1103/RevModPhys.71.S374. URL: http://journals.aps.org/rmp/abstract/10.1103/RevModPhys.71.S374.

[3] H Hertz. "Ueber die Berührung fester elastischer Körper". In: *Journal für die reine und angewandte Mathematik* 92 (1881), pp. 156–171.

[4] C Thornton. "Coefficient of restitution for collinear collisions of elastic perfectly plastic spheres". In: *Journal of Applied Mechanics-Transactions of the Asme* 64.2 (1997), pp. 383–386. DOI: 10.1115/1.2787319. URL: %3CGo%20to%20ISI%3E://WOS:A1997XH19800019.

[5] Robert L Jackson, Itzhak Green, and Dan B Marghitu. "Predicting the coefficient of restitution of impacting elastic-perfectly plastic spheres". In: *Nonlinear Dynamics* 60.3 (2010), pp. 217–229. DOI: 10.1007/s11071-009-9591-z.

[6] Goro Kuwabara and Kimitoshi Kono. "Restitution Coefficient in a Collision between Two Spheres". In: *Japanese Journal of Applied Physics* 26.Part 1, No. 8 (1987), pp. 1230–1233.

[7] Chuan-Yu Wu, Long-Yuan Li, and Colin Thornton. "Energy dissipation during normal impact of elastic and elastic–plastic spheres". In: *International Journal of Impact Engineering* 32.1–4 (2005), pp. 593–604. DOI: http://dx.doi.org/10.1016/j.ijimpeng.2005.08.007. URL: http://www.sciencedirect.com/science/article/pii/S0734743X05001223.

[8] K L Johnson. "Normal contact of inelastic solids". In: (1985), pp. 153–201. DOI: 10.1017/cbo9781139171731.007.

[9] Xiang Zhang and Loc Vu-Quoc. "Modeling the dependence of the coefficient of restitution on the impact velocity in elasto-plastic collisions". In: *International Journal of Impact Engineering* 27.3 (2002), pp. 317–341. DOI: http://dx.doi.org/10.1016/S0734-743X(01)00052-5. URL: http://www.sciencedirect.com/science/article/pii/S0734743X01000525.

[10] Robert L Jackson and Itzhak Green. "A Finite Element Study of Elasto-Plastic Hemispherical Contact Against a Rigid Flat". In: *Journal of Tribology* 127.2 (2005), p. 343. DOI: 10.1115/1.1866166.

[11] L Kogut and I Etsion. “Elastic-Plastic Contact Analysis of a Sphere and a Rigid Flat”. In: *Journal of Applied Mechanics* 69.5 (2002), p. 657. DOI: 10.1115/1.1490373.

[12] Fan Li, Jingzhe Pan, and Csaba Sinka. “Contact laws between solid particles”. In: *Journal of the Mechanics and Physics of Solids* 57.8 (2009), pp. 1194–1208. DOI: 10.1016/j.jmps.2009.04.012.

[13] H Peng, Z S Liu, and G H Zhang. “A study of overall contact behavior of an elastic perfectly plastic hemisphere and a rigid plane”. In: *Proceedings of the Institution of Mechanical Engineers Part J-Journal of Engineering Tribology* 227.J3 (2013), pp. 259–274. DOI: 10.1177/1350650112460799. URL: %3CGo%20to%20ISI%3E://WOS:000316639700007.

[14] Hirofumi Minamoto and Shozo Kawamura. “Effects of material strain rate sensitivity in low speed impact between two identical spheres”. In: *International Journal of Impact Engineering* 36.5 (2009), pp. 680–686. DOI: http://dx.doi.org/10.1016/j.ijimpeng.2008.10.001. URL: http://www.sciencedirect.com/science/article/pii/S0734743X0800239X.

[15] Hirofumi Minamoto and Shozo Kawamura. “Moderately high speed impact of two identical spheres”. In: *International Journal of Impact Engineering* 38.2–3 (2011), pp. 123–129. DOI: http://dx.doi.org/10.1016/j.ijimpeng.2010.09.005. URL: http://www.sciencedirect.com/science/article/pii/S0734743X10001375.

[16] E. Wang, T. On, and J. Lambros. “An Experimental Study of the Dynamic Elasto-Plastic Contact Behavior of Dimer Metallic Granules”. In: *Experimental Mechanics* 53.5 (Dec. 2012), pp. 883–892. DOI: 10.1007/s11340-012-9696-z. URL: http://link.springer.com/10.1007/s11340-012-9696-z.

[17] Erheng Wang, Philippe Geubelle, and John Lambros. “An Experimental Study of the Dynamic Elasto-Plastic Contact Behavior of Metallic Granules”. In: *Journal of Applied Mechanics* 80.2 (Jan. 2013), p. 21009. DOI: 10.1115/1.4007254. URL: http://appliedmechanics.asmedigitalcollection.asme.org/article.aspx?articleid=1661200.

[18] G R Johnson and W H Cook. “A constitutive model and data for metals subjected to large strains, high strain rates and high”. In: *Proceedings of the 7th International Symposium on Ballistics* (1983), pp. 541–547.

[19] Vitali Nesterenko. *Dynamics of Heterogeneous Materials*. Springer New York, 2011, p. 510. URL: https://books.google.com/books/about/Dynamics%7B%5C_%7Dof%7B%5C_%7DHeterogeneous%7B%5C_%7DMaterials.html?id=iqFxcgAACAAJ%7B%5C&%7Dpgis=1.

[20] Stéphane Job et al. “Solitary wave trains in granular chains: experiments, theory and simulations”. In: *Granular Matter* 10.1 (Sept. 2007), pp. 13–20.

DOI: 10.1007/s10035-007-0054-2. URL: http://link.springer.com/10.1007/s10035-007-0054-2.

[21] C Daraio et al. "Strongly nonlinear waves in a chain of Teflon beads." In: *Physical review. E, Statistical, nonlinear, and soft matter physics* 72.1 Pt 2 (July 2005), p. 016603. DOI: 10.1103/PhysRevE.72.016603. URL: http://journals.aps.org/pre/abstract/10.1103/PhysRevE.72.016603.

[22] V F Nesterenko et al. "Anomalous wave reflection at the interface of two strongly nonlinear granular media." In: *Physical review letters* 95.15 (Oct. 2005), p. 158702. DOI: 10.1103/PhysRevLett.95.158702. URL: http://journals.aps.org/prl/abstract/10.1103/PhysRevLett.95.158702.

[23] C Daraio et al. "Tunability of solitary wave properties in one-dimensional strongly nonlinear phononic crystals." In: *Physical review. E, Statistical, nonlinear, and soft matter physics* 73.2 Pt 2 (Feb. 2006), p. 026610. DOI: 10.1103/PhysRevE.73.026610. URL: http://journals.aps.org/pre/abstract/10.1103/PhysRevE.73.026610.

[24] D Ngo, F Fraternali, and C Daraio. "Highly nonlinear solitary wave propagation in Y-shaped granular crystals with variable branch angles." In: *Physical review. E, Statistical, nonlinear, and soft matter physics* 85.3 Pt 2 (Mar. 2012), p. 036602. DOI: 10.1103/PhysRevE.85.036602. URL: http://journals.aps.org/pre/abstract/10.1103/PhysRevE.85.036602.

[25] Andrea Leonard, Laurent Ponson, and Chiara Daraio. "Wave mitigation in ordered networks of granular chains". In: *Journal of the Mechanics and Physics of Solids* 73 (Dec. 2014), pp. 103–117. DOI: 10.1016/j.jmps.2014.08.004. URL: http://www.sciencedirect.com/science/article/pii/S0022509614001719.

[26] Robert L. Doney, Juan H. Agui, and Surajit Sen. "Energy partitioning and impulse dispersion in the decorated, tapered, strongly nonlinear granular alignment: A system with many potential applications". In: *Journal of Applied Physics* 106.6 (Sept. 2009), p. 064905. DOI: 10.1063/1.3190485. URL: http://scitation.aip.org/content/aip/journal/jap/106/6/10.1063/1.3190485.

[27] C Daraio et al. "Energy Trapping and Shock Disintegration in a Composite Granular Medium". In: *Physical review letters* 96.5 (Feb. 2006), p. 058002. DOI: 10.1103/PhysRevLett.96.058002. URL: http://journals.aps.org/prl/abstract/10.1103/PhysRevLett.96.058002.

[28] Fernando Fraternali, Mason A. Porter, and Chiara Daraio. "Optimal Design of Composite Granular Protectors". In: *Mechanics of Advanced Materials and Structures* 17.1 (Dec. 2009), pp. 1–19. DOI: 10.1080/15376490802710779.

URL: http://www.tandfonline.com/doi/abs/10.1080/15376490802710779%7B%5C#%7D.VsUdlvkrKCg.

[29] Jongbae Hong. "Universal power-law decay of the impulse energy in granular protectors." In: *Physical review letters* 94.10 (Mar. 2005), p. 108001. DOI: 10.1103/PhysRevLett.94.108001. URL: http://journals.aps.org/prl/abstract/10.1103/PhysRevLett.94.108001.

[30] K R Jayaprakash, Yuli Starosvetsky, and Alexander F Vakakis. "New family of solitary waves in granular dimer chains with no precompression." In: *Physical review. E, Statistical, nonlinear, and soft matter physics* 83.3 Pt 2 (Mar. 2011), p. 036606. DOI: 10.1103/PhysRevE.83.036606. URL: http://journals.aps.org/pre/abstract/10.1103/PhysRevE.83.036606.

[31] Alain Molinari and Chiara Daraio. "Stationary shocks in periodic highly nonlinear granular chains." In: *Physical review. E, Statistical, nonlinear, and soft matter physics* 80.5 Pt 2 (Nov. 2009), p. 056602. DOI: 10.1103/PhysRevE.80.056602. URL: http://journals.aps.org/pre/abstract/10.1103/PhysRevE.80.056602.

[32] Mason A Porter et al. "Highly nonlinear solitary waves in periodic dimer granular chains." In: *Physical review. E, Statistical, nonlinear, and soft matter physics* 77.1 Pt 2 (Jan. 2008), p. 015601. DOI: 10.1103/PhysRevE.77.015601. URL: http://journals.aps.org/pre/abstract/10.1103/PhysRevE.77.015601.

[33] Eduardo André de F. Bragança, Alexandre Rosas, and Katja Lindenberg. "Binary collision approximation for multi-decorated granular chains". In: *Physica A: Statistical Mechanics and its Applications* 392.24 (Dec. 2013), pp. 6198–6205. DOI: 10.1016/j.physa.2013.07.076. URL: http://www.sciencedirect.com/science/article/pii/S0378437113007073.

[34] S SEN et al. "Solitary waves in the granular chain". In: *Physics Reports* 462.2 (June 2008), pp. 21–66. DOI: 10.1016/j.physrep.2007.10.007. URL: https://www.researchgate.net/publication/243311638%7B%5C_%7DSolitary%7B%5C_%7Dwaves%7B%5C_%7Din%7B%5C_%7Dthe%7B%5C_%7Dgranular%7B%5C_%7Dchain.

[35] N. Boechler et al. "Tunable vibrational band gaps in one-dimensional diatomic granular crystals with three-particle unit cells". In: *Journal of Applied Physics* 109.7 (Apr. 2011), p. 074906. DOI: 10.1063/1.3556455. URL: http://scitation.aip.org/content/aip/journal/jap/109/7/10.1063/1.3556455.

[36] C. Hoogeboom et al. "Hysteresis loops and multi-stability: From periodic orbits to chaotic dynamics (and back) in diatomic granular crystals". In: *EPL (Europhysics Letters)* 101.4 (Feb. 2013), p. 44003. DOI: 10.1209/0295-

5075/101/44003. URL: http://iopscience.iop.org/article/10.1209/0295-5075/101/44003.

[37] E. B. Herbold et al. "Pulse propagation in a linear and nonlinear diatomic periodic chain: effects of acoustic frequency band-gap". In: *Acta Mechanica* 205.1-4 (Apr. 2009), pp. 85–103. DOI: 10.1007/s00707-009-0163-6. URL: http://link.springer.com/10.1007/s00707-009-0163-6.

[38] Alexander Breindel, Diankang Sun, and Surajit Sen. "Impulse absorption using small, hard panels of embedded cylinders with granular alignments". In: *Applied Physics Letters* 99.6 (Aug. 2011), p. 063510. DOI: 10.1063/1.3624466. URL: http://scitation.aip.org/content/aip/journal/apl/99/6/10.1063/1.3624466.

[39] V Tournat, V E Gusev, and B Castagnède. "Self-demodulation of elastic waves in a one-dimensional granular chain." In: *Physical review. E, Statistical, nonlinear, and soft matter physics* 70.5 Pt 2 (Nov. 2004), p. 056603. DOI: 10.1103/PhysRevE.70.056603. URL: http://journals.aps.org/pre/abstract/10.1103/PhysRevE.70.056603.

[40] R Ganesh and S Gonella. "Invariants of nonlinearity in the phononic characteristics of granular chains." In: *Physical review. E, Statistical, nonlinear, and soft matter physics* 90.2 (Aug. 2014), p. 023205. DOI: 10.1103/PhysRevE.90.023205. URL: http://journals.aps.org/pre/abstract/10.1103/PhysRevE.90.023205.

[41] Jérémy Cabaret, Vincent Tournat, and Philippe Béquin. "Amplitude-dependent phononic processes in a diatomic granular chain in the weakly nonlinear regime." In: *Physical review. E, Statistical, nonlinear, and soft matter physics* 86.4 Pt 1 (Oct. 2012), p. 041305. DOI: 10.1103/PhysRevE.86.041305. URL: http://journals.aps.org/pre/abstract/10.1103/PhysRevE.86.041305.

[42] C. Coste and B. Gilles. "On the validity of Hertz contact law for granular material acoustics". In: *The European Physical Journal B* 7.1 (Jan. 1999), pp. 155–168. DOI: 10.1007/s100510050598. URL: http://dx.doi.org/10.1007/s100510050598.

[43] Tommy On, Peter A. LaVigne, and John Lambros. "Development of plastic nonlinear waves in one-dimensional ductile granular chains under impact loading". In: *Mechanics of Materials* 68 (Jan. 2014), pp. 29–37. DOI: 10.1016/j.mechmat.2013.06.013. URL: http://www.sciencedirect.com/science/article/pii/S016766361300149X.

[44] Tommy On, Erheng Wang, and John Lambros. "Plastic waves in one-dimensional heterogeneous granular chains under impact loading: Single intruders and dimer chains". In: *International Journal of Solids and Structures* 62 (June 2015), pp. 81–90. DOI: 10.1016/j.ijsolstr.2015.02.006. URL: http://www.sciencedirect.com/science/article/pii/S0020768315000463.

[45] Raj Kumar Pal, Amnaya P. Awasthi, and Philippe H. Geubelle. "Wave propagation in elasto-plastic granular systems". In: *Granular Matter* 15.6 (Oct. 2013), pp. 747–758. DOI: 10.1007/s10035-013-0449-1. URL: http://link.springer.com/10.1007/s10035-013-0449-1.

[46] Raj Kumar Pal, Amnaya P Awasthi, and Philippe H Geubelle. "Characterization of wave propagation in elastic and elastoplastic granular chains." In: *Physical review. E, Statistical, nonlinear, and soft matter physics* 89.1 (Jan. 2014), p. 012204. DOI: 10.1103/PhysRevE.89.012204. URL: http://journals.aps.org/pre/abstract/10.1103/PhysRevE.89.012204.

[47] M. Shoaib and L. Kari. "Discrete element simulation of elastoplastic shock wave propagation in spherical particles". In: *Advances in Acoustics and Vibration* 2011 (2011). DOI: 10.1155/2011/123695.

[48] Raj Kumar Pal and Philippe H. Geubelle. "Impact response of elasto-plastic granular and continuum media: A comparative study". In: *Mechanics of Materials* 73 (June 2014), pp. 38–50. DOI: 10.1016/j.mechmat.2014.02.006. URL: http://www.sciencedirect.com/science/article/pii/S0167663614000349.

[49] A. Leonard, F. Fraternali, and C. Daraio. "Directional Wave Propagation in a Highly Nonlinear Square Packing of Spheres". In: *Experimental Mechanics* 53.3 (Oct. 2011), pp. 327–337. DOI: 10.1007/s11340-011-9544-6. URL: http://link.springer.com/10.1007/s11340-011-9544-6.

[50] A. Leonard et al. "Traveling waves in 2D hexagonal granular crystal lattices". In: *Granular Matter* 16.4 (Apr. 2014), pp. 531–542. DOI: 10.1007/s10035-014-0487-3. URL: http://link.springer.com/10.1007/s10035-014-0487-3.

[51] Masahiro Nishida and Yusuke Tanaka. "DEM simulations and experiments for projectile impacting two-dimensional particle packings including dissimilar material layers". In: *Granular Matter* 12.4 (Mar. 2010), pp. 357–368. DOI: 10.1007/s10035-010-0173-z. URL: http://link.springer.com/10.1007/s10035-010-0173-z.

[52] A Leonard and C Daraio. "Stress wave anisotropy in centered square highly nonlinear granular systems." In: *Physical review letters* 108.21 (May 2012), p. 214301. DOI: 10.1103/PhysRevLett.108.214301. URL: http://journals.aps.org/prl/abstract/10.1103/PhysRevLett.108.214301.

[53] I Szelengowicz, P G Kevrekidis, and C Daraio. "Wave propagation in square granular crystals with spherical interstitial intruders." In: *Physical review. E, Statistical, nonlinear, and soft matter physics* 86.6 Pt 1 (Dec. 2012), p. 061306. DOI: 10.1103/PhysRevE.86.061306. URL: http://journals.aps.org/pre/abstract/10.1103/PhysRevE.86.061306.

[54] I. Szelengowicz et al. “Energy equipartition in two-dimensional granular systems with spherical intruders”. In: *Physical Review E* 87.3 (Mar. 2013), p. 032204. DOI: 10.1103/PhysRevE.87.032204. URL: http://journals.aps.org/pre/abstract/10.1103/PhysRevE.87.032204.

[55] Amnaya P. Awasthi et al. “Propagation of solitary waves in 2D granular media: A numerical study”. In: *Mechanics of Materials* 54 (Nov. 2012), pp. 100–112. DOI: 10.1016/j.mechmat.2012.07.005. URL: http://www.sciencedirect.com/science/article/pii/S0167663612001317.

[56] Mohith Manjunath, Amnaya P. Awasthi, and Philippe H. Geubelle. “Wave propagation in 2D random granular media”. In: *Physica D: Nonlinear Phenomena* 266 (Jan. 2014), pp. 42–48. DOI: 10.1016/j.physd.2013.10.004. URL: http://www.sciencedirect.com/science/article/pii/S0167278913002807.

[57] Nathan W Mueggenburg, Heinrich M Jaeger, and Sidney R Nagel. “Stress transmission through three-dimensional ordered granular arrays”. In: *Physical Review E* 66.3 (Sept. 2002), p. 031304. DOI: 10.1103/PhysRevE.66.031304. URL: http://journals.aps.org/pre/abstract/10.1103/PhysRevE.66.031304.

[58] J Anfosso and V Gibiat. “Elastic wave propagation in a three-dimensional periodic granular medium”. In: *Europhysics Letters (EPL)* 67.3 (Aug. 2004), pp. 376–382. DOI: 10.1209/epl/i2004-10085-9. URL: http://iopscience.iop.org/article/10.1209/epl/i2004-10085-9.

[59] Franck Bourrier, François Nicot, and Félix Darve. “Physical processes within a 2D granular layer during an impact”. In: *Granular Matter* 10.6 (June 2008), pp. 415–437. DOI: 10.1007/s10035-008-0108-0. URL: http://link.springer.com/10.1007/s10035-008-0108-0.

[60] Mohith Manjunath, Amnaya P. Awasthi, and Philippe H. Geubelle. “Plane wave propagation in 2D and 3D monodisperse periodic granular media”. In: *Granular Matter* 16.1 (Jan. 2014), pp. 141–150. DOI: 10.1007/s10035-013-0475-z. URL: http://link.springer.com/10.1007/s10035-013-0475-z.

[61] A M Tichler et al. “Transmission and reflection of strongly nonlinear solitary waves at granular interfaces.” In: *Physical review letters* 111.4 (July 2013), p. 048001. DOI: 10.1103/PhysRevLett.111.048001. URL: http://journals.aps.org/prl/abstract/10.1103/PhysRevLett.111.048001.

[62] A. Shukla and C. Damania. “Experimental investigation of wave velocity and dynamic contact stresses in an assembly of disks”. In: *Experimental Mechanics* 27.3 (Sept. 1987), pp. 268–281. DOI: 10.1007/BF02318093. URL: http://link.springer.com/10.1007/BF02318093.

[63] A. Shukla, M. H. Sadd, and H. Mei. "Experimental and computational modeling of wave propagation in granular materials". In: *Experimental Mechanics* 30.4 (Dec. 1990), pp. 377–381. DOI: 10.1007/BF02321508. URL: http://link.springer.com/10.1007/BF02321508.

[64] B. Glam et al. "Dynamics of stress wave propagation in a chain of photoelastic discs impacted by a planar shock wave; Part I, experimental investigation". In: *Shock Waves* 17.1-2 (July 2007), pp. 1–14. DOI: 10.1007/s00193-007-0094-x. URL: http://link.springer.com/10.1007/s00193-007-0094-x.

[65] A. Seguin et al. "Sphere penetration by impact in a granular medium: A collisional process". In: *EPL (Europhysics Letters)* 88.4 (Nov. 2009), p. 44002. DOI: 10.1209/0295-5075/88/44002. URL: http://iopscience.iop.org/article/10.1209/0295-5075/88/44002.

[66] A Seguin et al. "Experimental velocity fields and forces for a cylinder penetrating into a granular medium." In: *Physical review. E, Statistical, nonlinear, and soft matter physics* 87.1 (Jan. 2013), p. 012201. DOI: 10.1103/PhysRevE.87.012201. URL: http://journals.aps.org/pre/abstract/10.1103/PhysRevE.87.012201.

[67] A Valance and J Crassous. "Granular medium impacted by a projectile: experiment and model." In: *The European physical journal. E, Soft matter* 30.1 (Sept. 2009), pp. 43–54. DOI: 10.1140/epje/i2009-10504-9. URL: http://www.ncbi.nlm.nih.gov/pubmed/19760440.

[68] Yan Zhu et al. "Propagation of Explosive Pulses in Assemblies of Disks and Spheres". In: *Journal of Engineering Mechanics* 123.10 (Oct. 1997), pp. 1050–1059. DOI: 10.1061/(ASCE)0733-9399(1997)123:10(1050). URL: http://ascelibrary.org/doi/abs/10.1061/(ASCE)0733-9399(1997)123:10(1050).

[69] J. B. Pendry. "Negative Refraction Makes a Perfect Lens". In: *Physical Review Letters* 85.18 (Oct. 2000), pp. 3966–3969. DOI: 10.1103/PhysRevLett.85.3966. URL: http://journals.aps.org/prl/abstract/10.1103/PhysRevLett.85.3966.

[70] Graeme W. Milton. "The Theory of Composites". In: *The Theory of Composites* (2002). URL: http://adsabs.harvard.edu/abs/2002thco.book.....M.

[71] R S Lakes et al. "Extreme damping in composite materials with negative-stiffness inclusions." In: *Nature* 410.6828 (Mar. 2001), pp. 565–7. DOI: 10.1038/35069035. URL: http://dx.doi.org/10.1038/35069035.

[72] Graeme W Milton. "New metamaterials with macroscopic behavior outside that of continuum elastodynamics". In: *New Journal of Physics* 9.10 (Oct. 2007), pp. 359–359. DOI: 10.1088/1367-2630/9/10/359. URL: http://iopscience.iop.org/article/10.1088/1367-2630/9/10/359.

[73] Mohamed Farhat, Sebastien Guenneau, and Stefan Enoch. "Ultrabroadband elastic cloaking in thin plates." In: *Physical review letters* 103.2 (July 2009), p. 024301. DOI: 10.1103/PhysRevLett.103.024301. URL: http://journals.aps.org/prl/abstract/10.1103/PhysRevLett.103.024301.

[74] Nicolas Stenger, Manfred Wilhelm, and Martin Wegener. "Experiments on elastic cloaking in thin plates." In: *Physical review letters* 108.1 (Jan. 2012), p. 014301. DOI: 10.1103/PhysRevLett.108.014301. URL: http://journals.aps.org/prl/abstract/10.1103/PhysRevLett.108.014301.

[75] Mohamed Farhat, Sebastien Guenneau, and Stefan Enoch. "Broadband cloaking of bending waves via homogenization of multiply perforated radially symmetric and isotropic thin elastic plates". In: *Physical Review B* 85.2 (Jan. 2012), p. 020301. DOI: 10.1103/PhysRevB.85.020301. URL: http://journals.aps.org/prb/abstract/10.1103/PhysRevB.85.020301.

[76] P A Cundall and O D L Strack. *A discrete numerical model for granular assemblies*. 1979. DOI: 10.1680/geot.1979.29.1.47.

[77] G T Gray. "Classic Split-Hopkinson Pressure Bar Testing". In: *ASM Handbook Volume 8, Mechanical Testing and Evaluation* (2000), pp. 462–476.

[78] W J Stronge. "Continuum Modeling of Local Deformation Near the Contact Area". In: (2000), pp. 116–145. DOI: 10.1017/cbo9780511626432.007.

[79] K L Johnson. *Contact Mechanics*. Cambridge University Press, 1987. URL: http://books.google.com/books?id=Do6WQlUwbpkC.

[80] M R Brake. "An analytical elastic-perfectly plastic contact model". In: *International Journal of Solids and Structures* 49.22 (2012), pp. 3129–3141. DOI: 10.1016/j.ijsolstr.2012.06.013.

[81] Chuan-yu Wu, Long-yuan Li, and Colin Thornton. "Rebound behaviour of spheres for plastic impacts". In: *International Journal of Impact Engineering* 28.9 (2003), pp. 929–946. DOI: 10.1016/s0734-743x(03)00014-9.

[82] Sinisa Dj Mesarovic and K L Johnson. "Adhesive contact of elastic–plastic spheres". In: *Journal of the Mechanics and Physics of Solids* 48.10 (2000), pp. 2009–2033. DOI: http://dx.doi.org/10.1016/S0022-5096(00)00004-1. URL: http://www.sciencedirect.com/science/article/pii/S0022509600000041.

[83] J H Zhao, S Nagao, and Z L Zhang. "Loading and unloading of a spherical contact: From elastic to elastic–perfectly plastic materials". In: *International Journal of Mechanical Sciences* 56.1 (2012), pp. 70–76. DOI: 10.1016/j.ijmecsci.2012.01.006.

[84] N.W. Ashcroft and N.D. Mermin. *Solid State Physics*. Sauders College Publishing, 1976.

[85] Erwan Hascoët, Hans J. Herrmann, and Vittorio Loreto. "Shock propagation in a granular chain". In: *Physical Review E* 59.3 (Mar. 1999), pp. 3202–3206. DOI: 10.1103/PhysRevE.59.3202. URL: http://journals.aps.org/pre/abstract/10.1103/PhysRevE.59.3202.

[86] James Tasi. "Evolution of shock waves in a one-dimensional lattice". In: *Journal of Applied Physics* 51.11 (July 1980), p. 5804. DOI: 10.1063/1.327538. URL: http://scitation.aip.org/content/aip/journal/jap/51/11/10.1063/1.327538.

[87] Shiming Zhuang, Guruswami Ravichandran, and Dennis E. Grady. "An experimental investigation of shock wave propagation in periodically layered composites". In: *Journal of the Mechanics and Physics of Solids* 51.2 (Feb. 2003), pp. 245–265. DOI: 10.1016/S0022-5096(02)00100-X. URL: http://www.sciencedirect.com/science/article/pii/S002250960200100X.

[88] Feng Li et al. "Tunable phononic crystals based on cylindrical Hertzian contact". In: *Applied Physics Letters* 101.17 (Oct. 2012), p. 171903. DOI: 10.1063/1.4762832. URL: http://scitation.aip.org/content/aip/journal/apl/101/17/10.1063/1.4762832.

Appendix A

NUMERICAL CODE

A.1 Outline of Numerical Code

The general outline of the code demonstrating all options and capabilities is as follows:

1. Initialization:
    a) Initial positions of each particle are specified.
    b) Material for each particle are chosen from a library of materials (or custom material properties specified).
    c) Boundary conditions are specified.
        i. Particles can be restricted to have a permanently fixed position.
        ii. Particles along a line of symmetry can be specified.
        iii. Pairs of particles can be specified to be periodic compliments and transfers forces to one another.
        iv. Polygons representing walls or flat impactors (flats) can be specified with prescribed masses (or infinite mass if they're immovable walls).
        v. Particles can be assumed to be in contact with an infinite, 1D linear medium.
    d) Initial conditions are specified.
        i. Particle can be given initial velocities.
        ii. Flats can be given initial velocities.
        iii. Force pulses or experimentally measured forces over time can be prescribed for particles or flats.
        iv. Velocity pulses or experimentally measured velocities over time can be prescribed for particles or flats.
    e) Global variables are initialized in which the history of plastic deformation at each contact point will be stored after each time step.
    f) Time steps, total time of the simulation, and number of time steps between intermediate data saves are specified.

g) Details about the contact law can specified.

i. Certain pieces of the physics can be neglected in order to observe their effect of dynamics.

ii. Experimentally measured contact responses or any tabular force-displacement law can be substituted (at the expense of simulation speed).

2. Time integration of Newton's 2nd Law. For each time step:

a) Inter-particle forces for each particle are calculated

i. The distance between the centers of every possible pair of particles is calculated. If this distance is less than the sum of the radii of the particles, the force between them is calculated using a contact law.

ii. The calculated force is applied in opposite directions to both of the particles along the axis between the center of the two particles.

iii. The calculated forces are also applied to particles' periodic complements if they are on a periodic boundary.

b) Applied forces are summed with inter-particle forces

c) Forces between flats and particles are calculated

i. The distance between each flat and the center of every particle is calculated. If the distance is less than the radius of the particle, then the force is calculated

ii. The force between a particle and a rigid flat is, by symmerty, the force required to compress two identical particles by twice the distance between the particle and rigid flat.

d) Prescribed velocities or displacements are applied to particles, overruling any applied forces on those particles

e) Particles on lines of symmetry are restricted to only move along the axis of symmetry and forces in that direction are doubled to account for forces from the opposite side of the line of symmetry.

f) History of maximum overlap between every possible pairs of particles and flats are updated and stored in global variables to allow for correct behavior of plasticity in future time steps.

g) Forces and masses are used to calculate accelerations of each particle using Newton's 2nd Law.

h) A 4th order Runge-Kutta method is used to integrate the accelerations and determine the initial conditions for the next time step.

i) After a chosen number of time steps, intermediate results are saved to database to allow for restarts and

3. Post-processing:

a) Particle positions and velocities over time are saved

b) Forces on each particle and contact forces at each pair of particles are saved

c) Positions, velocities and forces of any flats are saved

A.2 Matlab Scripts

A.2.1 Strain-Rate Dependent Contact Model for Elastic-Plastic Spheres

Below is the function used to calculate the interparticle forces using the strain-rate dependent elastic-plastic model for the compression of two spherical metallic particles. The inputs of the function are the relative displacement between the two particles, the relative velocity between the two particles, the material properties of the two particles, and the previous maximum displacements and forces experienced between the two particle due to plasticity. The output is the magnitude of the interparticle force.

```
function [f] = f_3Dcontact(i,j,d,v,var,dmax,Fmax)
% i,j - indicies of the particles in contact
% d - overlap between the two particles i,j
% v - velocities of particles i,j
% var - struct with material properties (E_star, r_star, sig_y) for i,j
% dmax - maximum displacements previously experienced between i,j
% Fmax - maximum force previously experienced between i,j

%Johnson-Cook strain rate dependence
if isequal(var.rate_dependent,'yes')
    sr=max(0,v)/(var.r(i)+var.r(j));
    sr_factor = max(1,(1+var.K_star(i,j)*log(sr/.001)));
else
    sr_factor = 1;
end
sy = var.sy_star(i,j)*sr_factor;

ratio = var.E_star(i,j)/sy;
%Empirical functions derived from FEM parameteric studies
deltap = (.00428*ratio.^(-1) + 1.47e-5)*(var.r_star(i,j)/(.0635*.0254));
c1 = -6.76*ratio^(-0.137) + 6.304;
c2 = (-3.99e-6*ratio^(-1) + 1.01e-9)*(var.r_star(i,j)/(.0635*.0254))^2;
```

```
23
24 %Von Mises criterion for initiation of plasticity
25 deltay=(1/4)*(var.r_star(i,j)/var.E_star(i,j)^2)*(pi*1.6*sy)^2;
26 p0 = c1*sy;
27
28 if d <= deltap && d > deltay && isequal(var.plasticity,'yes')
29     %intermediate region: f = d [A + B log(d)]
30     Fy = (4/3)*var.E_star(i,j)*sqrt(var.r_star(i,j))*deltay^(3/2);
31     a(1) = c2*p0*pi;
32     a(2) = p0*2*pi*var.r_star(i,j);
33     Fp = a(1) + a(2)*deltap;
34
35     f = d*(deltap*Fy*log(deltap)-deltay*Fp*log(deltay)+(deltay*Fp-deltap*
           Fy)*(log(d)))/((deltay*deltap)*(log(deltap)-log(deltay)));
36 elseif d > deltap && isequal(var.plasticity,'yes')
37     %plastic region: f = A + B*d
38     a(1) = c2*p0*pi;
39     a(2) = p0*2*pi*var.r_star(i,j);
40     f = a(1) + a(2)*d;
41 else
42     %elastic loading: f = A*d^(3/2)
43     f = (4/3)*var.E_star(i,j)*sqrt(var.r_star(i,j))*d^(3/2);
44 end
45
46
47 % UNLOADING and RELOADING
48 %(unloading occurs when velocity is less than 0, spheres are moving away
49 %from each other.  However, we follow the unloading curve back up upon
50 %reloading until f > Fmax or d > dmax)
51 if v < 0 || f < Fmax || d < dmax
52     if isequal(var.plasticity,'yes')
53         %elastic unloading with plasticity
54         Fy = (4/3)*var.E_star(i,j)*sqrt(var.r_star(i,j))*deltay^(3/2);
55         Rp = 4*var.E_star(i,j)*((2*Fmax+Fy)/(2*pi*1.6*var.sy_star(i,j)))
               ^(3/2)/(3*Fmax);
56         deltar = dmax-(3*Fmax/(4*var.E_star(i,j)*sqrt(Rp)))^(2/3);
57         d_un = (d-deltar)*((d-deltar)>=0);
58
59         f_un =(4/3)*var.E_star(i,j)*sqrt(Rp*(d_un).^3);
60     else
61         %elastic unloading without plasticity
62         f_un = (4/3)*var.E_star(i,j)*sqrt(var.r_star(i,j))*d^(3/2);
63     end
64     f = min(Fmax,f_un);
65 end
66
67 end
```

A.2.2 Function to Calculate $d\mathbf{X}/dt$ for Use in Numerical Integrator

Below is a Matlab function used to calculate the velocities and accelerations of each particle for each degree of freedom. These velocities and accelerations compose the vector which defines the many coupled, first-order ODEs which must be solved to numerically calculate the particles' displacements and velocities over time.

```
function dydt = odefunc(t,y,var)
% t: current time
% y: vector of all positions and velocities from previous time step
% var: struct containing material properties, boundary, applied forces and
%      other information required to calculate forces
%dydt: vector of all velocities and accelerations from this time step as
%      calculated from all forces on each particle

global g
dydt = zeros(size(y));

%Get positions and velocities of last time step
X = vec2array(y(1:3*var.n));
V = vec2array(y(3*var.n+1:2*3*var.n));

%number of particles (not including any flat impactors)
N = length(var.particles);

%define dmax and Fmax matrices from global memory
dmax = g.dmax;
Fmax = g.Fmax;

A = zeros(size(X));
d = zeros(var.n);
f = zeros(var.n);
%calculate forces from particle interactions
for i = 1:N
    for j = i+1:N
        %overlap between particles i and j
        d(i,j) = var.r(i) + var.r(j) - norm(X(j,:)-X(i,:));

        %if overlap is positive, calculate the force between the pair
        if d(i,j) > 0
            %unit vector from i to j
            e = (X(j,:)-X(i,:))/norm(X(j,:)-X(i,:));
            %relative velocity along vector e, don't need to save
            v = dot(V(i,:),e) - dot(V(j,:),e);
            %force magnitude between particles i and j
            f(i,j) = f_3Dcontact(i,j,d(i,j),v,var,dmax(i,j),Fmax(i,j));

            %acceleration vectors after applying forces on particles i, j
            A(i,:) = A(i,:) - f(i,j)*e/var.m(i);
```

```
            A(j,:) = A(j,:) + f(i,j)*e/var.m(j);
        end
    end
end

%save dmax, Fmax in global variable
if g.flag == 1
    g.t = [g.t; t];
    g.dmax = max(g.dmax,d);
    g.Fmax = max(g.Fmax,f);
end

dydt(1:3*var.n) = vec2array(V);              %Store velocities in dydt
dydt(3*var.n+1:2*3*var.n) = vec2array(A);    %Store accelerations in dydt
%Return dydt vector
end
```

A.2.3 4th Order Runge-Kutta Solver

Below the the Matlab function which uses a 4th-order Runge-Kutta solver to integrate $d\boldsymbol{X}/dt$ over discretized time and calculate the displacement and velocity of each particle in each degree of freedom. A key modification to the typical RK4 solvers used, it an additional evaluation of the function *odefun*, which calculates $d\boldsymbol{X}/dt$ again for each time step. The extra evaluation is used to store the plasticity histories of each contact between particles. The maximum interparticle overlap and interparticle forces for each set of contacts is stored in a global variable after each time step and used in subsequent time steps to calculate forces at later times.

```
function Y = ode4(odefun,tspan,y0,varargin)
%ODE4  Solve differential equations with a non-adaptive method of order
    4.
%
% odefun: the matlab function to calculate the vector X_dot representing
%         the 2nd order ODEdescribed inChapter 2
% tspan: the vector of equally spaced time steps
% y0: the initial conditions (positions and velocities) for each particle
%     for each degree of freedom
% varargin: struct containing material properties, boundary conditions,
%           applied forces and other information required to calculate
%           X_dot in odefun
%

global g   %initiate global struct "g"

h = diff(tspan); % get time step
f0 = feval(odefun,tspan(1),y0,varargin{:}); %evaluate initial conditions
y0 = y0(:);   % Make a column vector.

N = length(tspan);
```

```
Y = zeros(length(y0),N);
F = zeros(length(y0),4);

Y(:,1) = y0;
%For each time step:
for i = 2:N
  %Flag is used to instruct odefun not to store plasticity history for
  %intermediate evaluations
  g.flag = 0;

  %4th Order Runge-Kutta Method
  ti = tspan(i-1);
  hi = h(i-1);
  yi = Y(:,i-1);
  F(:,1) = feval(odefun,ti,yi,varargin{:});
  F(:,2) = feval(odefun,ti+0.5*hi,yi+0.5*hi*F(:,1),varargin{:});
  F(:,3) = feval(odefun,ti+0.5*hi,yi+0.5*hi*F(:,2),varargin{:});
  F(:,4) = feval(odefun,tspan(i),yi+hi*F(:,3),varargin{:});
  Y(:,i) = yi + (hi/6)*(F(:,1) + 2*F(:,2) + 2*F(:,3) + F(:,4));

  %Flag is turned on and forces are calculated using the final
  %displacements and velocities in order to store histories of
  %plasticity after each time step to be used in the next time step
  g.flag = 1;
  feval(odefun,tspan(i),Y(:,i),varargin{:});
end
Y = Y.';
```